MULTIFLUID MAGNETOHYDRODYNAMIC INVESTIGATION OF THE GLOBAL DYNAMICS OF SATURN'S MAGNETOSPHERE

A Dissertation
Presented to
The Academic Faculty

by

Ashok Rajendar

In Partial Fulfillment
of the Requirements for the Degree
Doctor of Philosophy in the
School of Earth and Atmospheric Sciences

Georgia Institute of Technology
December 2015

MULTIFLUID MAGNETOHYDRODYNAMIC INVESTIGATION OF THE GLOBAL DYNAMICS OF SATURN'S MAGNETOSPHERE

Approved by:

Dr. Carol Paty, Advisor
School of Earth and Atmospheric Sciences
Georgia Institute of Technology

Dr. James Wray
School of Earth and Atmospheric Sciences
Georgia Institute of Technology

Dr. Josef Dufek
School of Earth and Atmospheric Sciences
Georgia Institute of Technology

Dr. Mitchell Walker
School of Aerospace Engineering
Georgia Institute of Technology

Dr. Sven Simon
School of Earth and Atmospheric Sciences
Georgia Institute of Technology

Date Approved: November 3, 2015

To my mother Thankam and my father Raj who always supported me, however difficult the path ahead seemed. And to my wife, Shweta, who always believed in me, even when I did not. I am only here today because of their unwavering love and encouragement.

ACKNOWLEDGEMENTS

Please bear with me, I've been here a long time so there's a lot of people who need to be mentioned. This dissertation is the culmination of five years of work on planetary and space physics in the School of Earth and Atmospheric Sciences, but is also in many ways a capstone to the eight-and-a-half years I've spent at Georgia Tech. There have been a lot of ups and a lot of downs over those years, and without the following people I would not have the pleasure of writing this today. First and foremost, I would like to thank my advisor, Dr. Carol Paty. Beyond the productive and enjoyable working relationship we have established, I'm incredibly grateful for her taking a chance on a student with a wholly different background to what she was used. Carol, thank you for your guidance, insights, and constant encouragement. Being your student has been a pleasure, and I can only hope that my future mentors will be as wonderful to work with as you were.

I am also grateful for the time and effort that my committee members put into the dissertation and defense process. Dr. Josef Dufek has always been a ready source of excellent advice, and without his wonderful volcanology class I would never have been able to visit the amazing Mt. St. Helens. Dr. James Wray has likewise been of great help, and I particularly appreciate his flexibility in scheduling the defense, without which I may not have been able to graduate in time! Thanks are also due to Dr. Mitchell Walker of Aerospace Engineering, who was an active and eager participant despite joining the committee barely two months ago. Last, but definitely not least, I would like to thank Dr. Sven Simon, with whom I have had the pleasure of long and enlightening conversations about my research. Sven's contributions to this work belie his relatively recent arrival.

Beyond Georgia Tech, there have been numerous people who have supported and influenced the work in this dissertation. First, I am grateful to the NASA CDAPS program which funded this work. H. Todd Smith of the Applied Physics Laboratory has been an amazing collaborator, and I sincerely appreciate all the effort he has put in to helping us incorporate his model into our simulation. I would also like to thank Chris Arridge of Lancaster University and Caitriona Jackman of the University of Southampton for their time, input, and unstinting support of this work. Michelle Thomsen of the Planetary Science Institute has also been of great help, particularly in obtaining the data to which we wound up comparing our simulation results. There are so many others too, I couldn't possibly list them all here, so I will just say that I'm grateful to have been part of such a supportive scientific community.

Now...thanks first to all my research group! Jeremy Riousset, John Hale, Xin Cao, and Alexia Payan, you guys have been amazing. Thanks for all the long chats, for catching my mistakes, for late-night company, and for the companionship through this amazing journey. Thank you also to my officemates Taryn Black, Ozge Karakas, Gabe Eggers, and Jaime Convers, and to the larger geophysics and planetary family here at GT: Joe Estep, Mary Benage, Jen Telling, Ryan Cahalan, Julian McAdams (thanks for lending me your laptop for the defense!), Josh Mendez, Brendan Sullivan, Xiaofeng Meng, Zefeng Li, Dongdong Yao, Yanqung Su, Luju Ojha, Mary-Beth Wilhelm, George McDonald and Heather Chilton. Thanks finally to the many friends who've enriched my life these past eight years: Jack Crawford (awesome roommate, awesome friend), Saleem Malkana (wouldn't have met my wife without him!), the old guard at the FMRL (where graduating in less than a decade is noteworthy), and all the folks from the GT

Phd2Consulting club, without whom I wouldn't be embarking on this new exciting career, Alvin Zhou, Caitlin Baker, Gareth Guvanesan, and Apoorva Salimath.

And finally we come to my family, without whom nothing is possible. I cannot express my gratitude and love for you in these few sentences, suffice it to say I would not have succeeded here or anywhere else without your inexhaustible goodwill, encouragement, and support. To my in-laws Indira and Ram, I am delighted to be part of your family. To my mother and father, Thankam and Raj, to my wife Shweta, I won't embarrass you too much here - I've dedicated this thesis to you. It is a small token of how much I love and appreciate you.

TABLE OF CONTENTS

LIST OF TABLES

LIST OF FIGURES

LIST OF SYMBOLS

$\boldsymbol{B}$	magnetic field vector
B_{eq}	equatorial magnetic field strength
$\boldsymbol{B_{IMF}}$	IMF vector
$\boldsymbol{E}$	electric field vector
e^+	positive elementary charge
$f(v)$	velocity space distribution function
$\boldsymbol{F_L}$	Lorentz force
G	universal gravitational constant
H+	protons/proton plasma
hvy+	heavy ions/heavy ion plasma
$\boldsymbol{J}$	current
k_{ph}	photoionization rate constant
L	L-shell
L_i	volumetric loss rate of species i
m_i	mass of species i
M_S	mass of Saturn
n	number density
n_e	electron number density
n_i	ion number density
n_n	neutral number density
$\dot{n}_r$	radial number flux
P	pressure
P_e	electron pressure

P_i	ion pressure
q_i	charge of species *i*
r	radial coordinate
R_E	Earth radius
R_{En}	Enceladus radius (~260 km)
r_{En}	Enceladus orbit (~4 R_S)
R_H	hinging distance
R_J	Jupiter radius
R_S	Saturn radius (~60,000 km)
S_i	volumetric source rate of species *i*
S_{W+}	W+ volumetric source rate
T_e	electron temperature
T_S	Saturn rotation period (~10.6 hrs)
T_{trans}	transport time scale
$\boldsymbol{U_n}$	neutral velocity
$\boldsymbol{V}$	velocity
v	speed
$\boldsymbol{V_b}$	bulk plasma velocity
v_{corot}	corotation speed
$\boldsymbol{V_e}$	electron velocity
$\boldsymbol{V_i}$	ion velocity
v_r	radial speed
$\boldsymbol{V_{sw}}$	solar wind velocity
v_{sw}	solar wind speed
v_φ	azimuthal speed

W+	water group ions/plasma
$\boldsymbol{x}$	position vector
z_{ps}	plasma sheet displacement from equator
β	plasma beta
γ	ratio of specific heats
η	resistivity
κ_e	electron impact ionization rate constant
μ_0	permeability of free space
υ_e	electron impact ionization frequency
υ_{in}	ion-neutral charge exchange frequency
ρ_i	Mass density of species *i*
$\sum Q_{en}$	Heat transfer between electrons and neutrals
$\sum Q_{in}$	Heat transfer between species *i* and neutrals
σ_e	electron impact ionization cross section
σ_{in}	ion-neutral charge exchange cross section
φ	azimuthal coordinate

LIST OF ABBREVIATIONS

amu	atomic mass unit
AOA	angle of attack
AU	astronomical unit
BATSRUS	Block-Adaptive-Tree-Solarwind-Roe-Upwind-Scheme
CAPS	Cassini Plasma Spectrometer
ELS	Electron spectrometer (CAPS)
ENA	energetic neutral atom
FFT	Fast Fourier Transform
FGM	Fluxgate magnetometer (MAG)
IBS	Ion beam spectrometer (CAPS)
IMF	interplanetary magnetic field
IMS	Ion mass spectrometer (CAPS)
KSMAG	Kronocentric Solar Magnetic coordinate system
RCM	Rice Convection Model
S/VHM	Scalar/vector helium magnetometer (MAG)
SKR	Saturn Kilometric Radiation
SLT	Saturn local time
SOI	Saturn Orbital Insertion
TCR	traveling compression region
UT	universal [simulation] time

SUMMARY

The dynamics of Saturn's magnetosphere are driven internally by the planet's strong magnetic field, rapid rotation rate, and inner-magnetosphere plasma source, and externally by the solar wind. We use a multifluid magnetohydrodynamic simulation of Saturn's magnetosphere to investigate the production and transport of new plasma, the dynamics of Saturn's magnetotail, and response to seasonal variation. Saturn's closely aligned magnetic dipole and rotational axes are inclined 26.7° relative to the plane of its orbit. As a result, the magnetospheric morphology is strongly influenced by the solar wind; the plasma sheet is deformed into a "basin" at solstice, with decreasing curvature as the planet approaches equinox. Internally, new water group plasma is produced by ionization of Saturn's distributed neutral cloud, while charge-exchange collisions between magnetospheric ions and neutrals result in a loss of momentum from the plasma. New plasma is accelerated towards corotation by the magnetic field, while centrifugal stresses cause it to move radially outward. In order to prevent runaway inflation of the magnetosphere, this plasma must eventually escape, either through the flanks or down the magnetotail.

The Saturn multifluid model features three ion species (protons, water group ions, and a heavy tracer), allowing us to track the dynamics of each ion species, as well as the evolution of the electron pressure. We have modified the simulation to include neutral cloud interactions, specifically photoionization, electron impact ionization, and symmetric charge exchange, enabling simulation of mass-loading as a function of local plasma variables. Our 3D multifluid global simulation provides global context for in-situ

observations, which, while valuable, only provide data from a single spatial location at a given time. We use this model to study the production and outflow of plasma in the inner magnetosphere, as well as the characteristics of inward-moving outer-magnetosphere injection fingers. We also investigate the impact of seasonal changes on the global magnetospheric configuration and dynamics, as well as the plasma production and transport processes in the inner and middle magnetosphere. Finally, we investigate the evolution of plasmoids and their possible role in removing inner magnetosphere plasma. We validate our results using data from the Cassini Plasma Spectrometer and Magnetometer instruments (CAPS and MAG).

CHAPTER 1

INTRODUCTION

1.1 Anatomy of a magnetosphere

Depending on whom one asks, astrophysicists and space plasma physicists will variously state that the percentage of the observable universe that consists of magnetized plasmas is between 99% and 99.9%. While rarely a visible part of everyday life outside of very hot flames, lightning, and electric arcs, the physics of plasmas is of tremendous importance to modern civilization, particularly the flows of plasma in Earth's magnetosphere. Our magnetosphere is formed due to the interaction of the solar wind, the magnetized plasma flowing radially outwards from the Sun, and the Earth's magnetic field. We therefore begin by briefly describing the structure and important boundary layers of magnetospheres, using Earth's as an archetypal example.

Figure 1.1 shows how the action of the Lorentz force ($\boldsymbol{F}_L = q(\boldsymbol{E} + \boldsymbol{V} \times \boldsymbol{B})$, where q and $\boldsymbol{v}$ are the charge and velocity of a charged particle, and $\boldsymbol{E}$ and $\boldsymbol{B}$ are the electric and magnetic field vectors) acts to deflect ions and electrons encountering a magnetic field in opposite directions. When the solar wind encounters a planetary magnetic field, the differential charged-particle flow that results forms the Chapman-Ferraro current system. This current system maintains the subsolar boundary separating the solar wind and its Interplanetary Magnetic Field (IMF) from the cavity dominated by the planetary magnetic field and its associated plasma flows. We call this cavity the magnetosphere.

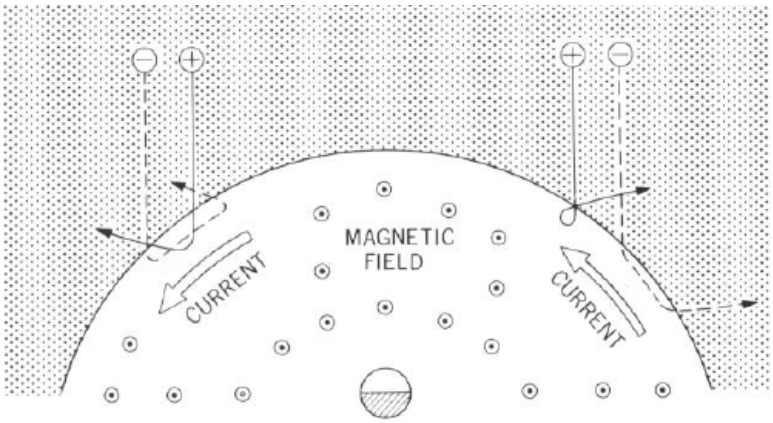

Figure 1.1 Deflection of charged particles encountering a magnetic field by the Lorentz force (source: *Nishida* [1982])

Figure 1.2 shows a schematic of a magnetosphere (in this case, Earth's) with important boundaries and features labeled. The magnetopause is the boundary separating the interior of the magnetosphere from the solar wind and IMF. Since the solar wind flows at supersonic and super-Aflvénic speeds (400 km/s < v_{sw} < 1000 km/s; the Aflvén wave is a magnetohydrodynamic wave that propagates through the plasma) a shock is formed in front of the magnetopause. Between this bow shock and the magnetopause lies the magnetosheath, a region of hot, sub-Aflvénic solar wind plasma and piled-up IMF field lines. It is bounded on the bow-side by the Chapman-Ferraro current system described above. The flow of the solar wind past the magnetopause compresses the anti-Sunward planetary magnetic field into a long structure known as a magnetotail. Currents arise due to $\nabla \times \boldsymbol{B}$ forces, which flow across the center of the magnetotail between dawn and dusk, in the region where the oppositely directed field lines (Sunward and anti-Sunward) are closest, which reinforce the structure of the magnetotail.

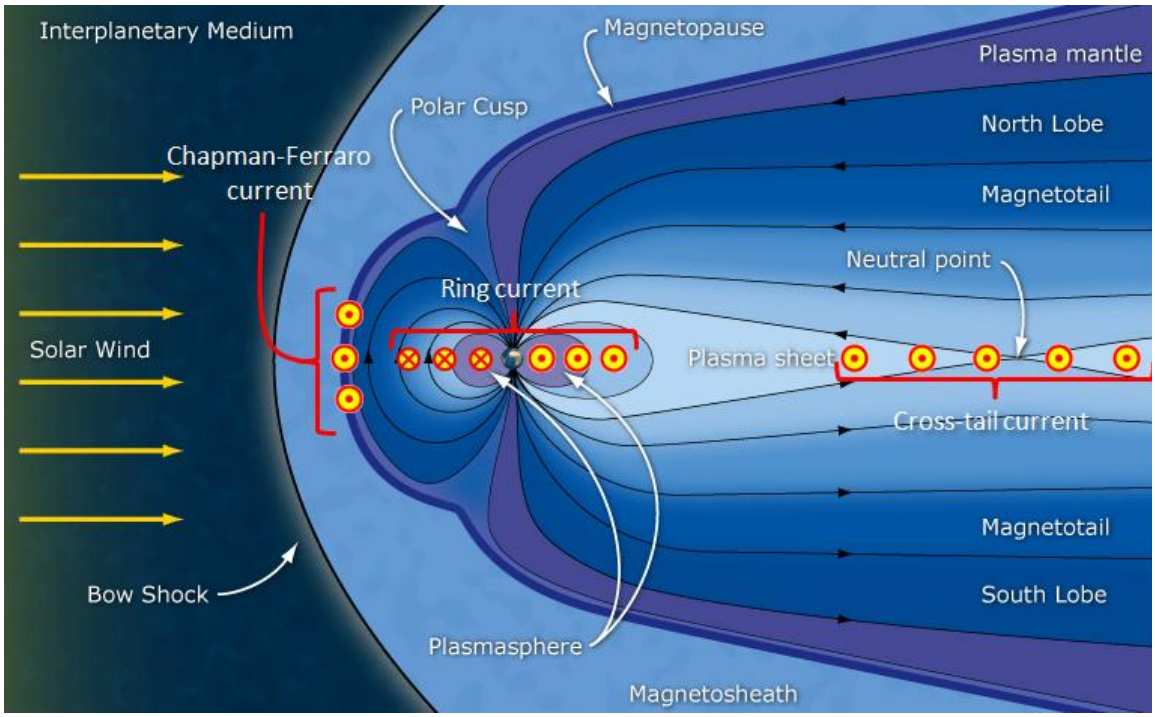

Figure 1.2 Schematic of Earth's magnetosphere along the day-night meridian (Source: modified from https://www.nasa.gov/mission_pages/ibex/news/spaceweather.html)

The magnetic field lines originating from the planet may be either open or closed. Open field lines are found near the poles, where they extend out of the magnetopause and close elsewhere, or in the lobes, where they extend far downtail but remain within the magnetotail until the structure dissipates entirely. The process whereby a close field line opens, or open field lines close is known as magnetic reconnection. We generally assume that space plasmas obey the "frozen-in" condition, whereby a fluid particle of plasma is constrained to move with the magnetic flux tube or field line it is associated with. However, during reconnection the frozen-in condition breaks down and plasma diffuses across oppositely directed field lines, and the field lines reconfigure (e.g.: at the neutral point shown in Figure 1.2). When this occurs, energy is released and the newly

reconfigured field lines accelerate away from one another. Solar wind plasma can enter the otherwise closed magnetosphere through reconnection.

The magnetic field is quasi-dipolar close to the earth, where the distortion caused by the interaction with the solar wind is minimized. In this region, known as the plasmasphere, the plasma tends to corotate with the planet (i.e.: it moves azimuthally around the planet's rotation axis at the same angular velocity). The individual charged particles gyrate along the magnetic field lines, executing bounce and drift motions. If their velocities along the field line are high enough, they may enter the Earth's atmosphere, colliding with the molecules and producing the colorful displays known as the Auroras Borealis and Australis. In addition to the bulk azimuthal velocity in the corotation direction, the magnetic field gradient and the curvature of the field lines close to the Earth cause the electrons positively charged ions to drift in opposite directions, creating the ring current, which flows around the planet. The direction of flow is such that it reduces the surface magnetic field strength.

There are numerous other phenomena that are of great interest in the Terrestrial magnetosphere, such as the important currents that link distant regions of the outer magnetosphere, the dynamics of substorms and the Dungey cycle, and the radiation belts. However, for the purposes of providing a simple description of the structure and important behavior found in magnetospheres in general, the above will suffice. We will describe some of the relevant phenomena that affect Saturn's magnetosphere in greater detail in Chapter 2. For those looking for a more rigorous introduction, we direct the reader to some of the numerous and excellent textbooks on the subject, such as *Dougherty* [2009], *Lyons* [1984], and *Baumjohann and Treumann* [1996].

1.2 Comparative magnetospheres

Table 1. Comparison of Earth, Jupiter, and Saturn and their magnetospheres

	Earth	Jupiter	Saturn
Orbital distance	1 AU	5-5.5 AU	9-10.1 AU
Radius	1 R_E = 6,400 km	1 R_J = 71,000 km	1 R_S = 60,000 km
Rotation rate	24 hrs	9.925 hrs	$1T_S \approx 10.6$ hrs[†]
Equatorial B-field	31,000 nT	428,000 nT	21,000 nT
Solar wind density	$5/cm^3$	$0.5/cm^3$	$0.1/cm^3$
Dipole tilt	10°	10°	> 0.1°
Axial tilt	23.4°	3.1°	26.7°
IMF	5 nT	1 nT	0.5 nT
Standoff distance	10 R_E	45-100 R_J	20-40 R_S
Internal plasma source	No	Yes (Io)	Yes (Enceladus)

[†]see Section 2.4 for discussion on uncertainty in measurements of rotation rate

Having described the basic structure of a magnetosphere, it is now instructive to examine the three best-studied magnetospheres in the Solar System and consider how they differ from one another. Thus, Table 1 lists some of the relevant parameters governing the magnetospheres of Earth, Jupiter, and Saturn. In many ways, Saturn and Jupiter are very similar planets: both are gas giants with similar bulk compositions, a large system of moons, and internal sources of plasma (Io in the case of Jupiter; the neutral cloud sourced from Enceladus in the case of Saturn). They are both also fast rotators with relatively strong magnetic fields, though Jupiter's equatorial field is an order of magnitude stronger than Saturn's. As such, both giant planet magnetospheres experience significant internal driving. The weaker solar wind conditions at 10 AU compared to 5 AU mean that even though Saturn's internal field is much weaker, its

subsolar magnetopause standoff distance is still almost 50% as large as Jupiter's, and both planets have an extended magnetodisc configuration when solar wind dynamic pressures are relatively low.

However, Saturn is much more than simply an intermediate case between Earth and Jupiter, and exhibits many unique behaviors, as shown in the schematic in Figure 1.3. The close alignment of the planet's spin and dipole axes means that it has been thus far impossible to accurately determine the planet's rotation rate, and while Saturn emits periodic signals (the Saturn Kilometric Radiation, or SKR) that may be close to the rotation rate, there is sufficient variability in these to disqualify them as exact proxies. The close alignment of the rotational and dipole axes, combined with its large axial tilt

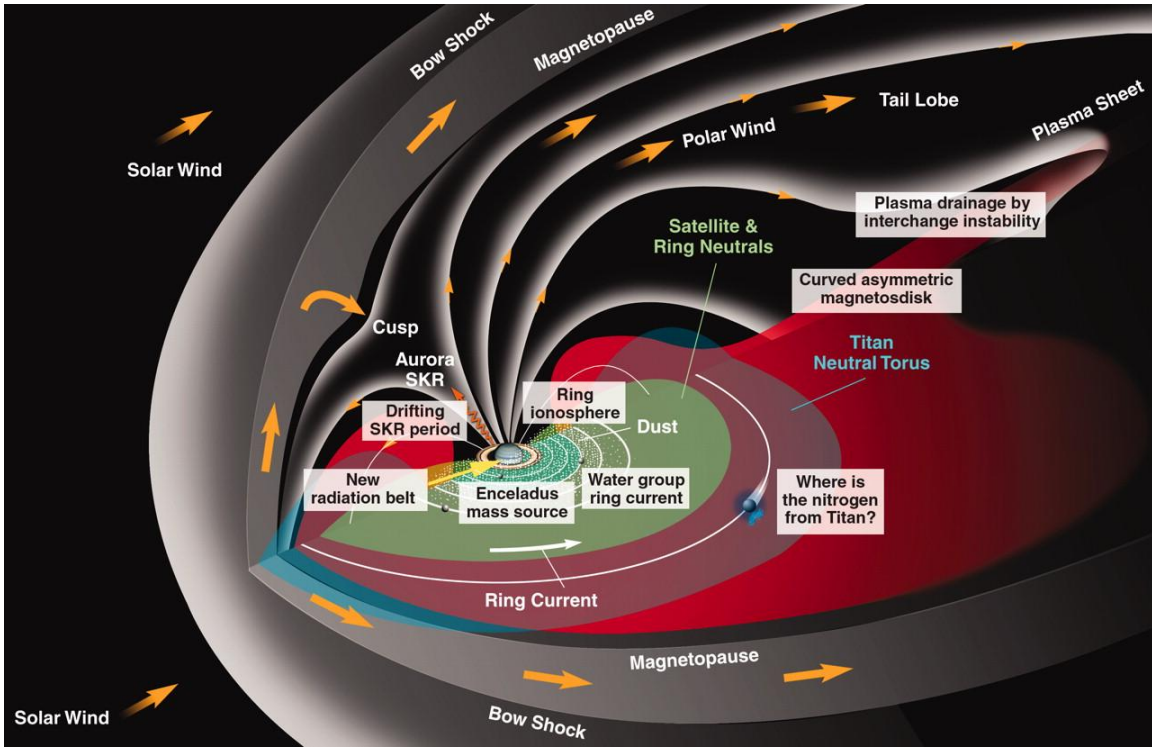

Figure 1.3 Schematic of Saturn's magnetosphere displaying important boundary layers and phenomena (Source: *Gombosi and Ingersoll* [2010])

results in warping of Saturn's plasma sheet and magnetodisc as the planet transitions from equinox to solstice, producing a "bowl" morphology that is unique in the Solar System. Saturn's plasma-neutral interactions are also of great interest. Unlike at Jupiter, where Io is bathed in a plasma torus with relatively low abundances of neutrals, neutral water group molecules are far more abundant than plasma in Saturn's inner magnetosphere. This in turn has implications for how the radial transport processes function at Saturn, as plasma-neutral collisions are far more frequent in this environment. Plasma-neutral interactions are also important further from the planet at Titan, where collisions between plasma constituents and the moon's thick, dense atmosphere were expected to contribute large plumes of ionized nitrogen to the magnetosphere, a phenomenon that has as yet proved elusive to distinguish from the *in situ* data. Finally, Saturn's rings also play a role in magnetospheric interactions. While they are a minor source of neutrals, they also act to absorb plasma in their vicinity, "quenching" flows of charged particles in their vicinity.

1.3 Scope of dissertation

1.3.1 Topics of interest

In this dissertation we investigate the dynamics of Saturn's magnetosphere using results from an updated version of the Saturn multifluid model incorporating the effects of plasma-neutral interactions. This allows us to simulate the production of new plasma in Saturn's inner magnetosphere and the effect of the neutral cloud on bulk plasma flows in this region in a self-consistent manner. While there are numerous open questions across a wide range of topics concerning Saturn's magnetosphere, we concentrate on three major topics here:

1) The production and transport of plasma in Saturn's magnetosphere.

2) The effect of seasonality on the global morphology and dynamics of Saturn's magnetosphere, and the seasonal impact on the production and transport processes.
3) The dynamics of Saturn's magnetotail, focusing on the downtail loss of water group plasma (W+) sourced from the inner magnetosphere.

1.3.2 Importance of multifluid simulations

The Cassini probe has collected an enormous volume of *in situ* data on Saturn's magnetosphere over the last decade, and as a result there have been numerous studies investigating magnetospheric phenomena ranging from corotation lag to the characteristics of Saturn's plasmoids. However, instrument data from a single spacecraft like Cassini is limited to observations from a single trajectory. The investigators who work on *in situ* data use a variety of tools, theories, and hypotheses to investigate various phenomena and integrate observations into cohesive pictures of how various processes function at Saturn, but it is still enormously difficult to develop a global understanding of its magnetosphere. 3D global models like the Saturn multifluid model provide global context to observations, and allow us to simulate large-scale phenomena that are hard to resolve with data from single trajectories. Unfortunately, simulations rely on various approximations, which means that under certain conditions or in some domains they are no longer able to provide reasonable fidelity to the observations. Our updated multifluid model allows accurate simulation of the inner magnetosphere for the first time. This is where mass- and momentum-loading processes occur, and thus it is essential to understanding the internal driving of Saturn's magnetosphere. Saturn's magnetosphere is unique, being rotationally driven like Jupiter but also much less energetic, with neutrals dominating over ions and electrons in the inner magnetosphere. By investigating the

above topics, we therefore not only contribute to the corpus of knowledge on Saturn's magnetospheric dynamics, but also to the understanding of how plasma-neutral interactions affect bulk flows of plasmas.

1.3.3 Outline of document

We have modified the Saturn multifluid model [*Kidder et al.*, 2009; *Kidder et al.*, 2012] to include mass- and momentum-loading interactions between the neutral cloud and the plasma, specifically electron-impact ionization and photoionization of the neutral cloud, as well as elastic charge-exchange collisions between water group ions and neutrals. The extended neutral cloud is incorporated into the simulation as a static representation, based on work by H.T. Smith (unpublished model, 2015). We have used the updated model to investigate the rate of plasma production and radial transport in the inner magnetosphere.

Chapter 2 provides the relevant background that is necessary to understanding the dynamics of Saturn's magnetosphere, as well as the Cassini spacecraft instruments which provide the data that we have used to validate our model. We discuss the physics of rotationally-driven magnetospheres, how Saturn's magnetospheric structure changes over the course of its orbit, and conclude with a brief overview of the various periodic phenomena that occur inside the magnetosphere.

Chapter 3 describes the Saturn multifluid model and the specific modifications that have been made to incorporate plasma-neutral interactions. We discuss in detail how the multifluid equations have been modified to include source terms, as well as how those terms are modeled in order to incorporate electron-impact ionization, photoionization, and elastic charge-exchange collisions interactions with the Enceladus neutral cloud.

In Chapter 4, we validate the results of our model, by comparing them to Cassini Plasma Spectrometer (CAPS) and Magnetometer (MAG) observations from the Cassini prime mission. We present model output for Saturn's southern hemisphere solstice, which corresponds to Saturn's orbital position just prior to Cassini's Saturn Orbital Insertion (SOI) phase, comparing our results for inner magnetosphere plasma properties with *in situ* data, a region that previous investigators were unable to simulate accurately.

Chapter 5 describes in detail the production of new plasma in the inner magnetosphere, as well as the radial transport process in Saturn's inner and middle magnetosphere at southern hemisphere Solstice. We discuss the temporal and spatial variability of the global production of new water group plasma, as well as the structures that transport this plasma out of the inner magnetosphere. All data in Chapters 4 and 5 are from the same 45 hour time interval (4.25 Saturn rotations).

Chapter 6 is a discussion of the effects of seasonal variability, focusing on the differences between the two seasonal extremes of equinox and southern hemisphere solstice. We describe how the global morphology of the plasma sheet is affected by Saturn's orbital location, both in terms of the average shape during a given season as well as the motion of the plasma sheet on timescales of minutes to hours. We also discuss whether seasonality drives inner magnetosphere dynamics, and thus whether it exerts an influence on the mass- and momentum-loading processes that act there.

Chapter 7 is a brief discussion of an exploratory investigation into the dynamics of Saturn's magnetotail, focusing on two key phenomena: the downtail loss of plasma transported outwards from the inner magnetosphere, and the production of plasmoids due to the Dungey cycle when the IMF is directed antiparallel to the planetary magnetic field.

We close this dissertation with Chapter 8, in which we discuss broad conclusions and implications of this work, as well as possible directions of future investigations. We also include supporting material in Appendix A in the form of both figures and animations (captions only; animation files can be found at smartech.gatech.edu). The animations are intended to provide the reader with more clarity on the dynamics of Saturn's inner magnetosphere than static images alone can provide. Finally, Appendix B briefly covers some of the lessons learned in dealing with large legacy physics codes.

CHAPTER 2

SATURN'S MAGNETOSPHERE

2.1 Rotationally driven magnetospheres

2.1.1 Internal driving of Saturn's magnetosphere

There are two known rotationally driven magnetospheres in the Solar System: Saturn's and Jupiter's. For a magnetosphere to be driven internally the rotation of a planet, three prerequisite conditions must be satisfied:

1) a strong planetary magnetic field and fast rotation rate;

2) a conductive ionosphere;

3) an internal source of plasma.

Corotation, or the enforced motion of plasma with the planet's rotation, is a consequence of the fact that the charged particles comprising the magnetospheric plasma and magnetic field lines are "frozen in" one another in most situations. The ions undergo cyclotron, bounce, and drift motion, but barring unusually high gradients they are constrained to execute this motion about the field lines they are associated with. As such, motion of the plasma can deform field lines, while motion of the field lines can transport plasma. *Hill* [1979] states that the imposition of corotation as the result of viscous coupling between the conductive ionosphere and the neutral atmosphere. The collision of ions tied to the field lines with neutrals results in an imposition of an electric field in the magnetosphere that causes the plasma to move at the same angular velocity as the ionosphere. An alternate interpretation is of rotation of the magnetic field and hence the

plasma tied to it, but the essential feature is that a minute portion of the rotational kinetic energy of the planet is passed to the plasma around it.

As Saturn has a relatively strong magnetic field, a highly conductive ionosphere, and a high rotation rate (see Table 1), azimuthal plasma flows dominate much of the magnetosphere. However, corotation is dependent on ionospheric conductivity, which is finite due to the impedance resulting from ion-neutral collisions in the ionosphere. The creation of new plasma from the neutral cloud results in increased mass carried by the tubes of magnetic flux, which in turn requires a greater torque to be exerted at the ionosphere. The finite ionospheric conductivity means that at a certain radial distance away from Saturn, corotation must break down and flux tubes containing plasma beyond this distance will start lagging behind the corotating inner flow [*Hill*, 1979; *Eviatar and Richardson*, 1986]. This is dependent on the rate of mass loading, the ionospheric Pedersen conductivity, the radius of Saturn, and the strength of its planetary magnetic field. At Saturn, this breakdown in corotation occurs between $L \approx 4$ and 5.5 (the L-shell value is defined as the locus of the dipole magnetic field lines which pass through a given radial distance from the planet's center at the equator, e.g.: $L = 2$ defines the field lines which intersect with $r = 2\ R_S$ at $z = 0$). This phenomenon has considerable influence on the overall magnetospheric dynamics.

2.1.2 Saturn's neutral cloud

Saturn's neutral cloud, the dominant source of new plasma produced in the inner magnetosphere, was first discovered in 1993 through analysis Hubble Space Telescope's Faint Object Spectrograph data [*Shemansky et al.*, 1993]. From the highest density region in the vicinity of Enceladus, the cloud extends inwards to less than 2 R_S from Saturn and

outwards to over 10 R_S, as well as to 2 R_S above and below the plane of the equator [*Jurac et al.*, 2002]. The primary source of the neutral cloud is the icy moon Enceladus, orbiting at a distance of r = 4 R_S. This tiny satellite ($R_{En} \approx 260$ km) experiences vigorous cryovolcanic activity near its southern pole along the so-called "tiger stripes", a series of long, parallel depressions in the surface exhibiting elevated temperatures [*Porco et al.*, 2006; *Spencer et al.*, 2006]. Large plumes of solid and gaseous material are observed to emanate from these features. While most of the particulate matter falls back to the surface, approximately 10^2-10^3 kg/s of water vapor escapes to enter Saturn's orbit and form the neutral torus [*Hansen et al.*, 2006; *Waite et al.*, 2006; *Burger et al.*, 2007]. The neutral torus is a narrowly confined region close to Enceladus' orbit with abundant water vapor, while the neutral cloud is the expanded structure containing the photodissociated products of the expelled water vapor, O, and OH, as well as the torus itself [*Fleshman et al.*, 2010]. The existence of the expanded cloud is due to interactions between the neutrals and the magnetospheric plasma: the relatively fast-moving ions collide with the slow moving neutrals, as discussed in Section 3.4.2, resulting in a net transfer of energy from the plasma to the neutral cloud. Some of these neutrals gain sufficient energy to escape the inner magnetosphere entirely in the form of energetic neutral atoms (ENAs), but many of these fast-moving neutrals collide with slower neutrals, thus imparting their energy to the rest of the cloud and causing the entire structure to assume an expanded configuration [*Johnson et al.*, 2006; *Cassidy and Johnson*, 2010; *Smith et al.*, 2010].

The neutral cloud is the primary source of mass- and momentum-loading, with new water group ions being produced by photoionization and electron-impact ionization of the water group neutrals [*Pontius and Hill*, 2006; *Tokar et al.*, 2006; *Pontius and Hill*,

2009]. This newly-produced plasma is cold and slow-moving, and must be accelerated to corotation by Saturn's magnetic field. Saturn has a strong magnetic field, a conductive ionosphere, and a rapid rotation rate, so azimuthal plasma flows dominate much of the magnetosphere. While the exact rotation rate is unknown due to the close alignment of the spin and magnetic dipole axes, using the Saturn Kilometric Radiation (SKR) as a proxy yields a rapid rotation period of approximately 10.6-10.8 hours [*Gurnett et al.*, 2009; *Gurnett et al.*, 2010]. Since the azimuthal velocities of the plasma exceed the Keplerian orbital velocities outside of $r = 1.9\ R_S$, the resultant centrifugal stresses act to accelerate inner-magnetosphere plasma radially outwards. The constant mass loading from continuous production of new plasma and Saturn's finite ionospheric conductivity result in the centrifugal stresses overwhelming the magnetic field's ability to radially confine the plasma, causing flux tubes loaded with inner magnetosphere plasma to move radially outwards [*Hill*, 1979; *Eviatar and Richardson*, 1986].

2.1.3 Plasma transport in the inner magnetosphere

Conservation of magnetic flux requires that the cold inner-magnetosphere plasma moving radially outwards must in turn be balanced by the inward movement of hot and tenuous outer-magnetosphere plasma and their associated flux tubes. This process is known as the centrifugal interchange process or instability (see Figure 2.1), and is the primary process which transports plasma out of the inner magnetosphere. Injection events or "fingers" of hot rarefied plasma have been observed numerous times by the Cassini spacecraft as close in as $5\ R_S$ from Saturn, and are the strongest evidence for the interchange process in the Saturnian magnetosphere [*Burch et al.*, 2005; *Hill et al.*, 2005; *Mauk et al.*, 2005]. The magnetopause boundary acts as a barrier to the outward moving

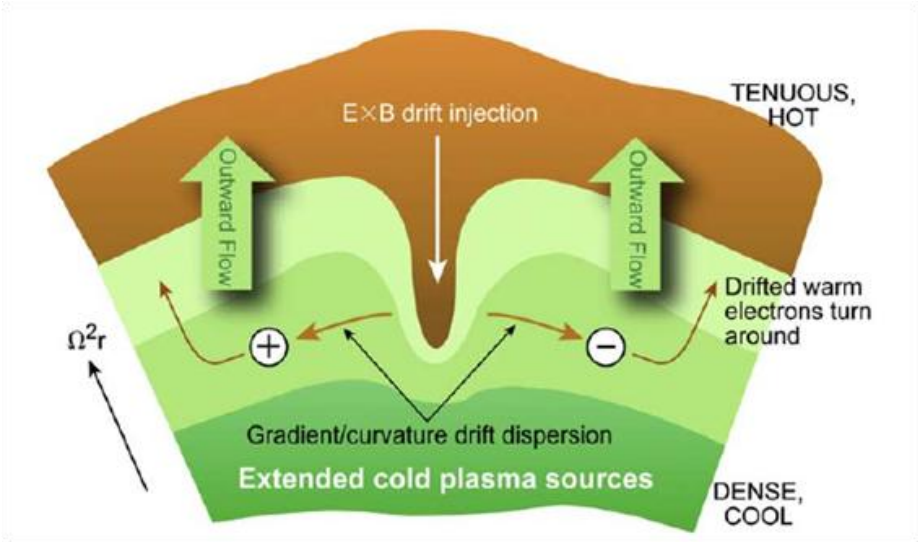

Figure 2.1 Schematic of the centrifugal interchange instability, showing the inward injection of hot plasma to conserve the flux lost through outward movement of flux tubes containing cold inner magnetosphere plasma (Source: *Rymer et al.* [2008])

flux tubes on the dayside, but when this plasma rotates around the nightside, there is no such bounding force. The flux tubes may then continue to distend radially as corotation lag increases, eventually reconnecting and leaving the magnetosphere. Whether most of the inner magnetosphere plasma escapes in large- or small-scale plasmoids downtail, as a steady "drizzle" down the flanks, or through Kelvin-Helmholtz instabilities along the dusk magnetopause flanks is still a topic of debate [*Bagenal and Delamere*, 2011].

2.2 Magnetic reconnection at Saturn

2.2.1 Vasyliunas and Dungey cycles

The identification and study of plasmoids is of great importance to building a comprehensive understanding of the dynamics of Saturn's magnetosphere. Plasmoids are the final stage in the mass flow from the inner magnetosphere: plasma-laden tubes of magnetic flux distend, resulting in reconnection forming plasmoids in the nightside which

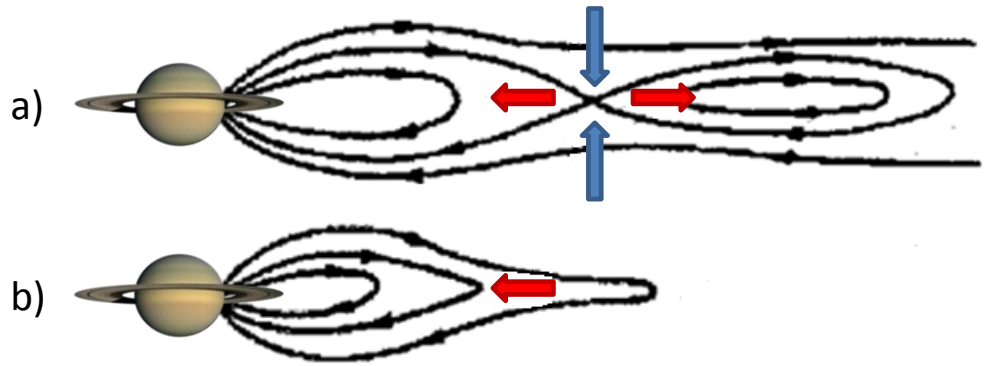

Figure 2.2 Schematic of closed-flux X-line reconnection in the nightside magnetosphere due to distension of plasma-laden flux tube by the centrifugal interchange instability (Source: modified from *Vasyliunas* [1983]). Black lines and arrows represent magnetic field lines; blue and red arrows represent field line and plasma motion in *z* and *r* respectively. a) compression of magnetotail field in *z* causes reconnection as frozen-flux condition breaks down, thus forming loop-type plasmoid; energy released results in acceleration of field away from reconnection X-line. b) plasmoid has advected tailwards out of frame, while closed field lines accelerate planetward.

are then convected downtail. This process is known as the Vasyliunas cycle [*Vasyliunas*, 1983], a schematic of which is shown in Figure 2.2. This is an example of closed flux magnetic reconnection, where both ends of a field line that is undergoing reconnection terminate in the planet. The other major reconnection-driven process is the Dungey cycle [*Dungey*, 1961], which involves the erosion of dayside magnetic flux when the IMF and planetary magnetic fields are antiparallel. The resulting open field lines are advected antisunward by the solar wind, and then compressed in the magnetotail. These open field lines eventually reconnect on the night side, thus this is an example of open flux reconnection. There is evidence that magnetopause reconnection at Saturn's subsolar magnetopause is rarer than at Jupiter or Earth, as a result of the high gradients in plasma β (ratio of plasma pressure to magnetic field pressure) across the magnetopause and magnetosheath [*Masters et al.*, 2012]. It has been hypothesized that reconnection for the

Dungey and Vasyliunas cycles occurs in different regions of the magnetotail, with the former occurring predominantly in the post-midnight sector and the latter in the pre-midnight sector [*Cowley et al.*, 2005].

Hill et al. [2008] presented observations of plasmoid formation and release in the magnetotail, confirming that they contain water group ions, and thus that they contain material originating from the inner magnetosphere. Nevertheless, it is unclear if this plasmoid is due to Dungey or Vasyliunas cycle reconnection. The reconnection process results in heating and acceleration of plasma, which in turn releases radiation and results in energy in the form of plasma waves. The plasmoids themselves are of impressive size, often several planetary radii in length, and the acceleration imparted to them during reconnection is considerable, with plasmoids moving downtail at speeds of hundreds of kilometers per second [*Jackman et al.*, 2008]. It is important to note, however that Cassini's orbit is ill suited to extensive study of plasmoid formation and release. Thus, dynamical simulations can be of great importance in building our understanding of these events and the consequences they have for other magnetospheric phenomena.

Dungey cycle behavior has been observed at Saturn, but the process by which the vast majority of plasma from the inner magnetosphere is lost has yet to be conclusively established. Previous investigators found that mass loss rates from large-scale plasmoids are far too low to account for the rate at which new plasma is produced in the inner magnetosphere by one or two orders of magnitude [*Bagenal and Delamere*, 2011; *Jackman et al.*, 2014]. If either the "dusk-side drizzle" or loss via small-scale plasmoid hypotheses described in *Bagenal and Delamere* [2011] are true, the relative paucity of observations may be because Cassini has rarely visited this region [*Jackman et al.*, 2014].

2.2.2 Plasmoid morphology

Plasmoids possess one of two basic morphologies: loops or flux ropes, as shown in Figure 2.3 [*Zong et al.*, 2004; *Jackman et al.*, 2014]. While a given magnetosphere may produce both types, it has been found that flux ropes tend to be more common at Earth, while all observed plasmoids at Saturn exhibit loop morphology [*Jackman et al.*, 2014]. As an aside, we note that all published Saturn global models tend to produce flux ropes instead of loops [*Jia et al.*, 2012b; *Kidder et al.*, 2012]. Figure 2.3 also shows the expected magnetic field signature recorded by a spacecraft that flies through each type of plasmoid (loop, flux rope, or loop-enclosed flux rope). There is a final plasmoid signature in Figure 2.3, the travelling compression region (TCR). This is what a spacecraft would see when the its trajectory does not actually intersect with a plasmoid, but a plasmoid

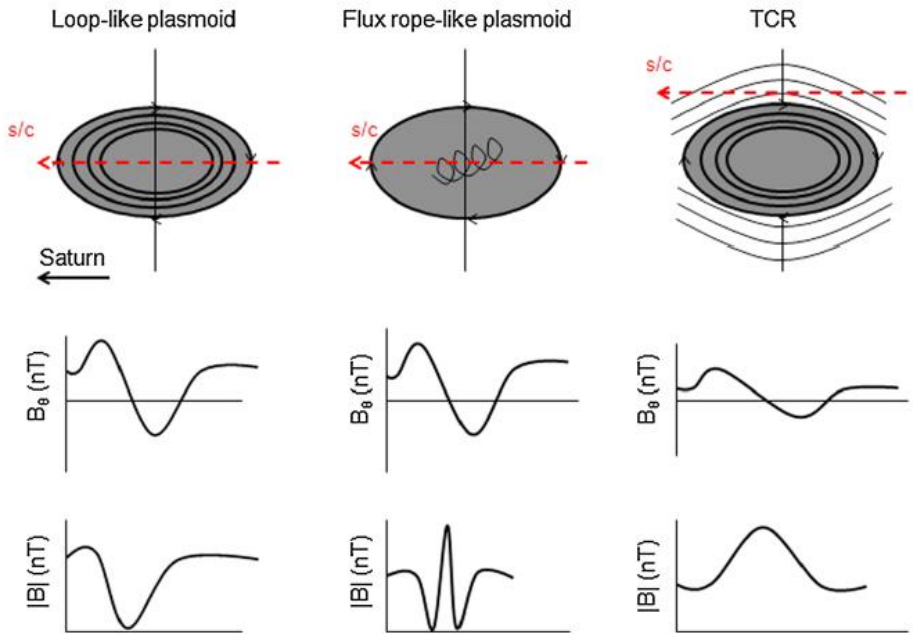

Figure 2.3 Schematic illustrations and magnetic field signatures of plasmoids and TCRs. Dashed red arrows represent spacecraft trajectory relative to plasmoid or TCR (Source: *Jackman et al.* [2014], modified from *Zong et al.* [2004])

passes close by instead, compressing the open field lines in the lobes. These signatures were measured relatively frequently at Saturn during solstice, since plasmoids travel along the curved magnetodisc (see Section 2.3 below), and thus did not often intersect with Cassini which typically orbited below the plasma sheet at this part of its mission.

2.3 Global morphology and seasonal variability

Saturn's magnetosphere is driven both externally, by the solar wind, and internally, by the planet's rotation and the outward flow of newly-produced plasma. The seasonal impact of solar wind forcing on gross morphology is now well-understood: *Arridge et al.* [2008] showed that the "bowl" or "basin" shaped current sheet during southern solstice was due to the solar wind dynamic pressure acting upon the southern magnetopause boundary, as show in Figure 2.3, while *Sergis et al.* [2011] observed a reduction in curvature with decreasing angle of attack as Saturn approached equinox.

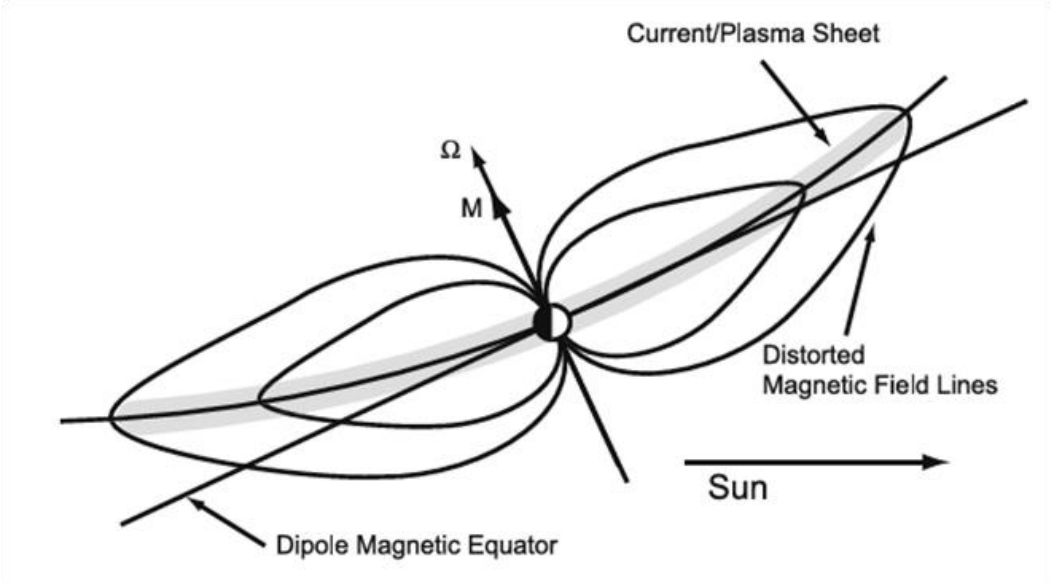

Figure 2.4 Deformation of Saturn's magnetosphere due to solar wind dynamic pressure and the planet's significant obliquity (Source: *Arridge et al.* [2008])

2.4 Periodicities

While the investigation of the various periodic phenomena observed in Saturn's magnetosphere is beyond the scope of this investigation, the importance of periodicities to Saturn's magnetospheric dynamics as well as to the overall history of the inquiry into this topic requires that we briefly discuss the topic here. The close alignment of Saturn's dipole and rotational axes means that, unlike Jupiter, there is no precession of the magnetic field which reveals the planet's true interior rotation rate.

Historically, the Saturn Kilometric Radiation (SKR), a signal with a period of approximately 10.6 hrs first observed by the Voyager probes, has been treated as the approximate rotation rate. However, this is complicated by the fact that there are in fact two different sources, one in the northern hemisphere, and one in the southern hemisphere [*Zarka*, 1998], each of which has a slightly different period which drifts over time [*Gurnett et al.*, 2009; *Lamy*, 2011; *Cowley and Provan*, 2015]. By the beginning of the Cassini epoch (2004-present), the period of the stronger (southern) SKR component was approximately 10.8 hrs, while the northern component was at around 10.6 hrs. As shown in Figure 2.5 from *Cowley and Provan* [2015], by 2010 both periods had drifted to around 10.7 hrs, at approximately the same time as the emergence of the Great White Spot, a planet-spanning storm in the Saturn's northern hemisphere that lasted over 200 days [*Sánchez-Lavega et al.*, 2012; *Sanz-Requena et al.*, 2012]. The drift of the SKR is far too great for it to be directly correlated with an interior rotation rate, which means that the latter is still a mystery.

Numerous phenomena in Saturn's magnetosphere have been observed to oscillate at approximately the SKR period. Consequently, the investigation of these periodicities

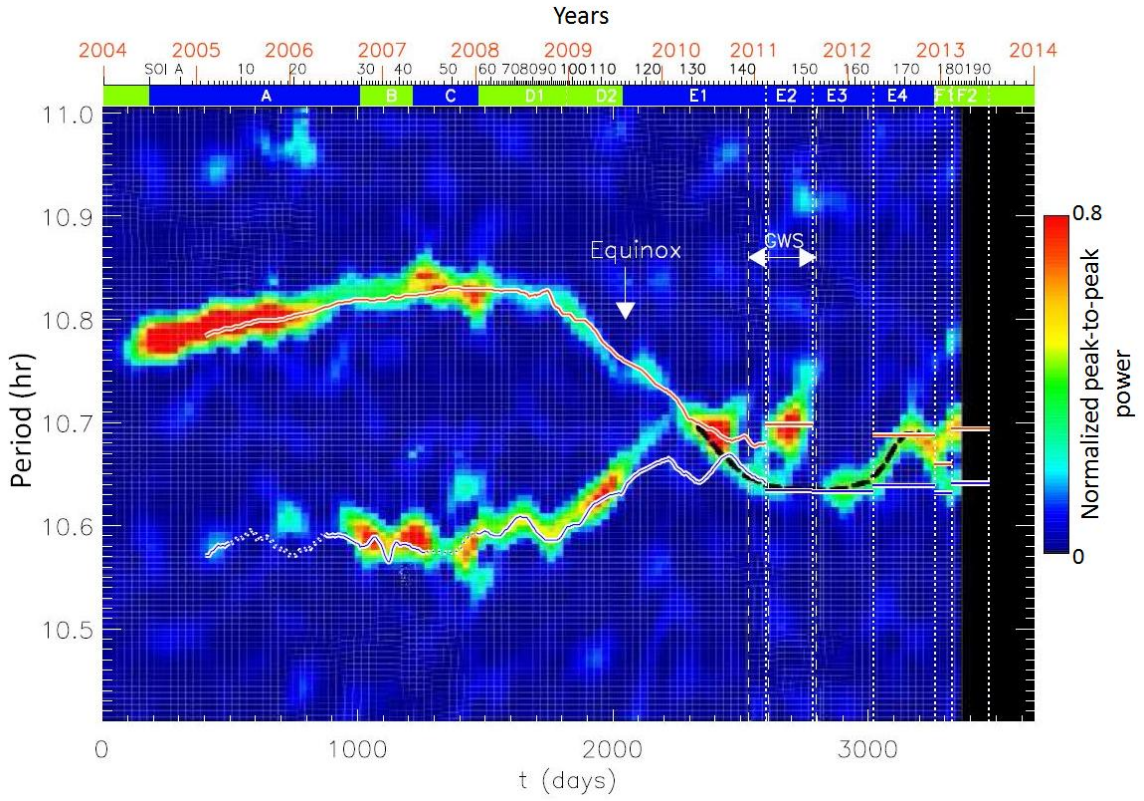

Figure 2.5 Strength and period of northern and southern SKR components over the Cassini era (Source: modified from *Cowley and Provan* [2015])

system has become important to understanding the dynamic behavior of the magnetosphere, in addition to any light such inquiries might shed on the planetary rotation rate. Periodicities in charged particle populations were among the earliest to be investigated during the Cassini epoch [*Carbary et al.*, 2007b; *Carbary et al.*, 2007a], with density variations in both ions and electrons being observed at a period of approximately 10.8 hrs early in the mission. *Carbary et al.* [2009] later showed that both the northern and southern SKR periods could be discerned in the energetic electron population. Saturn's magnetosphere also produces periodicities on a very large scale, with the magnetopause and bow shock "breathing" (oscillating towards and away from the planet) at approximately the SKR period [*Clarke et al.*, 2010b; *Clarke et al.*, 2010a]. Indeed,

many of the previous periodic phenomena can be understood in the context of periodic motion of the plasma sheet with a specific phase relationship with one or both components of the SKR [*Arridge et al.*, 2011a; *Carbary*, 2013].

There have been numerous hypotheses about what causes these periodicities, but thus far every hypothesis has had fatal flaws. Some investigators favor the camshaft model, in which they postulate the existence of a longitudinally rotating magnetic anomaly that perturbs the magnetic field, thus transmitting periodic signals [*Espinosa et al.*, 2003; *Achilleos et al.*, 2010]. Unfortunately, no magnetic anomaly has been located that satisfies these requirements. Another hypothesis has been advanced by *Jia et al.* [2012a], involving rotating ionospheric vortices, but *Smith* [2014] asserts that such vortices are energetically unfeasible. Furthermore, *Winglee et al.* [2013] show that periodicities may originate due to interactions between the centrifugal interchange instability and Titan. This is an important possibility to consider in light of the fact that that *Russell et al.* [2008] have shown that Titan may exert a significant influence on certain aspects of Saturn's global magnetospheric dynamics. In summary, as a result of the complexities and competing hypotheses surrounding this issue, we have chosen not to tackle this topic head-on, and instead merely introduce it here so that the reader understands the nature of this debate.

2.5 Cassini at Saturn

While the Voyager probes provided a wealth of data on the Saturnian system, it was the 2004 arrival of the Cassini probe that began the present era where we have collected and analyzed vast amounts of data about Saturn, its moons, and its magnetosphere. With that has come a new understanding of a unique magnetosphere that

many previous investigators assumed combined the characteristics of Jupiter's and Earth's. Of particular interest to us are the data from the Cassini Magnetometer (MAG) and Plasma Spectrometer (CAPS) instruments, which we use to validate our simulation. In this section, we therefore give a brief overview of the Cassini spacecraft and mission, and the MAG and CAPS instruments.

The Cassini spacecraft was launched in 1997, and entered Saturn orbit (Saturn Orbital Insertion, or SOI) on 1 July 2004. It has spent the last eleven years orbiting Saturn and gathering a wealth of data on the planet, its moons, and its magnetosphere. The period from 2004-2008 is known as the Prime Mission, during which it has helped make numerous exciting discoveries, including the discovery of the Enceladus tiger stripes and plumes, the curvature of Saturn's plasma sheet, and the landing of the Huygens probe on Titan, the first human craft to land on a body in the outer Solar System. Since 2008, the Cassini mission has been extended twice. Cassini has traveled on a variety of trajectories, sampling most of Saturn's magnetosphere , including some passes as close as 5 R_S from Saturn and others into the deep magnetotail, and has therefore contributed immensely to our understanding of these regions. The end of the mission is drawing close however: in 2017, Cassini will be plunged into Saturn's atmosphere to ensure that it does not eventually collide with one of Saturn's moons, thus contaminating its surface.

The MAG instrument is actually comprised of two separate magnetometers, both mounted on an 11 m boom extending from the Cassini spacecraft: a fluxgate magnetometer (FGM) is mounted halfway along the boom, while a scalar/vector helium magnetometer (S/HVM) is mounted at the end. The overall MAG instrument uses both magnetometers together to obtain low noise and high dynamic range measurements of the

magnetic fields in and around Saturn's magnetosphere. The high dynamic range and sensitivity enables the instrument to accurately measure magnetic fields throughout the magnetosphere, from within a few R_S of the planet all the way to the deep magnetotail. For a detailed discussion of the construction and function of MAG, we direct the reader to *Dougherty et al.* [2004].

CAPS is likewise comprised of separate instruments, the Electron Spectrometer (ELS), the Ion Mass Spectrometer (IMS), and the Ion Beam Spectrometer (IBS). The entire CAPS instrument is mounted on an actuated platform that moves in azimuth in order to provide as wide a field of view as possible. ELS measures electrons between 0.6 and 28 keV in logarithmic energy bins, while IMS measures the ions in hot, diffuse plasmas between 1 and 50 keV/q. The mass/charge ratio range that IMS can measure extends from 1 to 400 amu/q. CAPS is intended to complement the MIMI instrument: together they can measure particles at energies from 1 eV to 1 MeV (18 MeV for ions). IBS is intended to observe narrow ion beams, and is therefore not relevant to the topics that we cover in this dissertation. However, the inquisitive reader can learn about CAPS in depth from *Young et al.* [2004].

CHAPTER 3

THE SATURN MULTIFLUID MODEL

3.1 Modeling Saturn's magnetosphere

With its large size and enormous variations of characteristic length scales and velocities, Saturn's magnetosphere is a difficult system to model numerically, second only to Jupiter's among Solar System magnetospheres. While numerous published models have addressed certain aspects of Saturn's magnetosphere, global models have been relatively rare. The two most notable global Saturn models are the BATSRUS single-fluid magnetohydrodynamic (MHD) model, and the multifluid multiscale MHD model from the University of Washington, Seattle. Our model is descended from the latter.

The BATSRUS model was first applied at Saturn by *Hansen et al.* [2005], who very early on showed that the external conditions at equinox are such that the plasma sheet should be warped, hinged at both the bow and tail. *Arridge et al.* [2008] later showed that this was indeed the case, with definitive evidence of the so-called "bowl" morphology of Saturn's plasma sheet and magnetodisc. Later, *Zieger et al.* [2010] conducted a numerical investigation into open flux reconnection and the release of plasmoids, finding that there were strong relationships between the upstream conditions and the rate of production of large-scale flux rope plasmoids in Saturn's magnetotail. Most recently, *Jia et al.* [2012b], *Jia et al.* [2012a], *Jia and Kivelson* [2012], and *Kivelson and Jia* [2014] have published an updated version of the BATSRUS Saturn model, focusing on the implications of ionospheric vortices inside the inner boundary driving the SKR-related periodicities in Saturn's magnetosphere. BATSRUS is a mature

and highly optimized model with a wide range of numerical schemes at its disposal, and has thus been a pillar in the modeling community for over a decade. However, the fact that the large-scale Saturn model is single-fluid only means that there are important regions and behaviors in Saturn's magnetosphere that it is unable to simulate effectively.

By virtue of its separate ion fluid components and ability to track the electron population characteristics, the multifluid model is much better suited to simulating the inner regions of Saturn's magnetosphere with its populations of ion species of with significantly different mass-to-charge ratios. Multifluid MHD was first presented in a global model of Earth's magnetosphere [*Winglee*, 1998], and has since been extended to several other solar system bodies, including Ganymede [*Paty*, 2006], Titan [*Snowden and Winglee*, 2013], and Saturn [*Kidder et al.*, 2009; *Kidder et al.*, 2012]. The model utilizes a nested-grid structure, which enables it to simulate complex multi-scale, multi-body interactions, such as the Saturn-Titan interaction [*Winglee et al.*, 2013]. The ability to track individual plasma components means that it is possible to incorporate self-consistent plasma-neutral interactions such as electron-impact ionization and ion-neutral charge exchange collisions, pioneered by *Snowden and Winglee* [2013] in investigating the Titan's interaction with magnetospheric plasma flows. This approach was so successful that it was later adopted by *Rubin et al.* [2015] at Europa using BATSRUS's multifluid scheme. Early versions of the Saturn multifluid model were among the first to produce outflow and injection fingers, but like many previous MHD models they experienced severe supercorotation in certain regions of the magnetosphere where this has not been observed by spacecraft instruments [*Kidder et al.*, 2009]. In this paper, we discuss the results of a modified and extended version of the Saturn model incorporating

plasma-neutral interactions, thus enabling simulation of the effects of mass- and momentum loading in the global magnetosphere.

One other notable model is the Rice Convection Model, or RCM [*Liu et al.*, 2010]. This is a 2.5D model (infinite in *z* along Saturn's rotational axis) which has been used to study the centrifugal interchange instability at Saturn, focusing on the production of outflow structures and injection fingers. It is thus the only other model to produce these structures at Saturn. The RCM results show good qualitative results in terms of corotation lag and the development of the interchange instability, but the overall number and azimuthal coverage by the injection fingers is quite different from what has been observed at Saturn, a likely consequence of the 2.5D geometry. It is nevertheless an extremely useful tool that has provided excellent insights into the processes governing Saturn's magnetospheric dynamics.

3.2 The multifluid multiscale model

The multifluid technique is a generalization of the well-known single fluid MHD technique, where each positive ion species with the same or similar mass-to-charge ratio can be treated as an individual fluid. A model can include an arbitrary number of ion fluids, while the electrons are treated as a zero-mass fluid that flows instantaneously to neutralize charge. Multifluid MHD thus enables study of the dynamics of individual ion species and produces more accurate behavior in regions with diverse ion species of varying abundances, such as in Saturn's inner magnetosphere. The ability to track the properties of each major plasma component also makes the multifluid technique ideal for the simulation of plasma-neutral interactions, which are of great importance to these process in the vicinity of the Enceladus neutral cloud.

The updated Saturn model incorporates three singly-charged ion species with the following mass/charge ratios: 1amu/e^+ (protons or H+, comprising the bulk of the solar wind and also sourced from Saturn's ionosphere); 17 amu/e^+ (water group ions or W+, e.g.: H_2O^+, OH^+, O^+, sourced primarily from ionization of the neutral cloud, with a smaller ionospheric source); and 32 amu/e^+, a low-abundance heavy ion included as a tracer. In addition to tracking the pressure, density, and velocity of these species, the modified multifluid equations (see Section 3.3) also tracks the evolution of the water group fluid due to photoionization and electron impact ionization of the neutral cloud, as well as momentum exchange due to elastic collisions between water group ions and neutrals. The current nested grid comprises six boxes with resolution decreasing by factors of two from the innermost (0.25 R_S) to the outermost box (8 R_S), as shown in Figure 3.1 (box 6 omitted due to size). The innermost box contains the planet and most of the inner magnetosphere. The fine grid spacing in the innermost box allows the model to resolve small-scale features and therefore accurately simulate plasma-neutral interactions, while the magnetopause boundary and much of the magnetotail is captured at a still-reasonable 1 R_S grid spacing, thus permitting reasonable computational performance by using coarser spacing farther from the planet.

The origin of our coordinate system is at the center of Saturn, with the *z* axis aligned with the planet's rotational and dipole axes. The *y* axis points in the direction of the planet's orbital motion, and the *x* axis is perpendicular to both and points nominally in

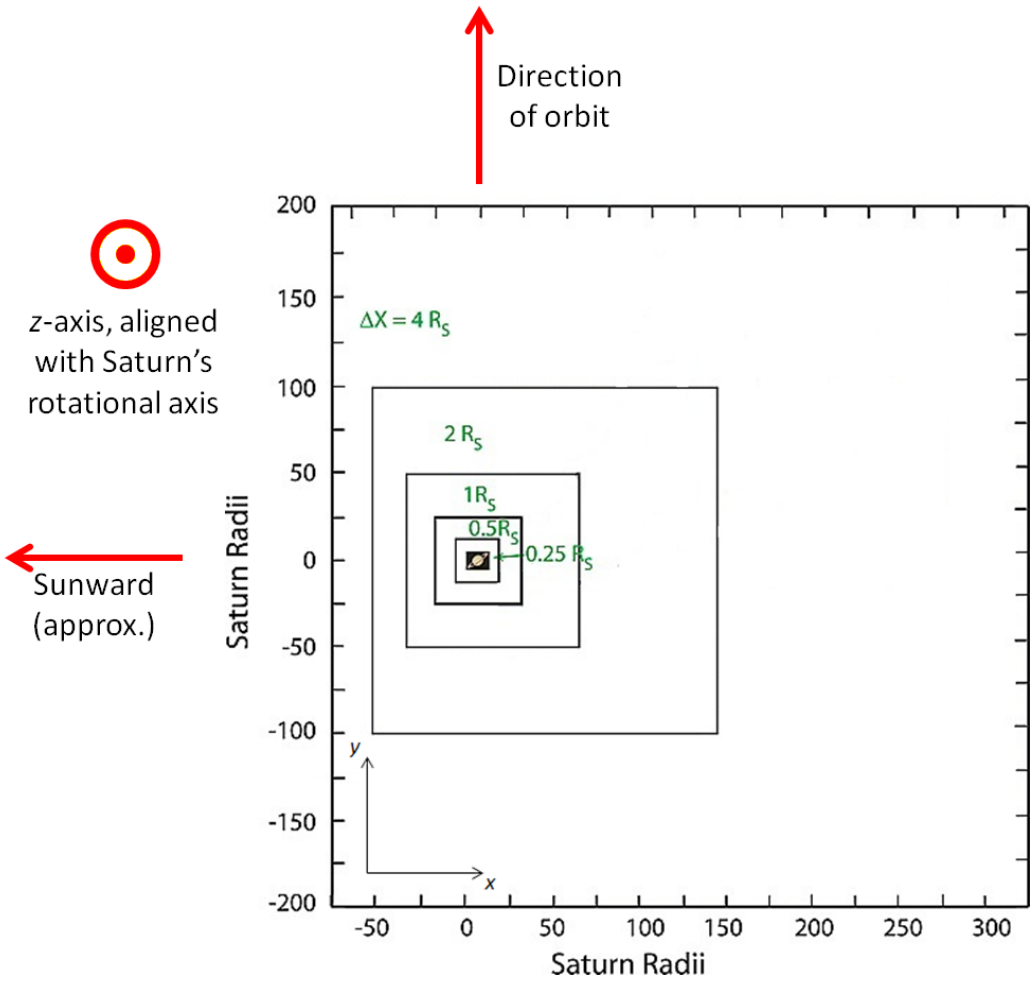

Figure 3.1 Schematic of the nested-grid structure of the Saturn multifluid model (Source: modified from *Winglee et al.* [2009])

the anti-Sunward direction. This is similar to one of the standard inertial frames used at Saturn, the Kronocentric Solar Magnetic (KSMAG) frame described in *Arridge et al.* [2011b], except that the KSMAG *x* and *y* axes point in the opposite directions from our coordinate system. To transform from KSMAG to our system involves a simple 180° rotation around the *z*-axis. The incoming solar wind conditions can be varied to simulate different angles of attack, and therefore seasonal conditions (e.g.: during equinox, the solar wind flows in the positive *x* direction, as the *x* axis at this point in Saturn's orbit

points directly in the antisunward direction). In this paper we will often need to refer to features that are at some stated radial distance away from the planet's spin axis. Thus, we will also often refer to a cylindrical coordinate system with an identical *z* axis, radius $r = \sqrt{x^2 + y^x}$, and $\varphi = \arctan(y/x)$.

3.3 Governing multifluid equations

Equations 1-9 are the multifluid equations [*Winglee*, 1998; *Kidder et al.*, 2009], modified to include the effects of neutral cloud interactions [*Snowden and Winglee*, 2013]. These equations govern the evolution of the plasma variables velocity $\boldsymbol{V}$, mass density ρ, and pressure P for the ions and the electrons (denoted *i* and *e* respectively), as well as the electric field and magnetic fields $\boldsymbol{E}$ and $\boldsymbol{B}$, and current density $\boldsymbol{J}$. Variables m_i, q_i, and n_i are the mass, charge, and number density of ion species *i*, and γ is the ratio of specific heats ($c_p/c_v \approx 1.67$, assumed to approximate a monatomic ideal gas). Equations 1 and 2 are the mass and momentum conservation equations for ion species *i*, while 3 is the equation of state.

$$\frac{\partial \rho_i}{\partial t} + \nabla \cdot (\rho_i \boldsymbol{V_i}) = A \tag{1}$$

$$\rho_i \frac{D\boldsymbol{V_i}}{Dt} = q_i n_i (\boldsymbol{E} + \boldsymbol{V_i} \times \boldsymbol{B}) - \nabla P_i - \left(\frac{GM_S}{{R_S}^2}\right) \rho_i \hat{\boldsymbol{r}} + B + C \tag{2}$$

$$\frac{\partial P_i}{\partial t} = -\gamma \nabla \cdot (P_i \boldsymbol{V_i}) + (\gamma - 1)\boldsymbol{V_i} \cdot \nabla P_i + \sum Q_{in} \tag{3}$$

Terms A, B, and C, described in Equation 4, and $\sum Q_{in}$ from Equation 3 are the modifications made to the governing plasma equations to incorporate the effects of neutral cloud interactions on the ion fluids. Term A is the change in density of species *i* due to the local source (mass-loading) and loss rates, S_i and L_i. Term B is the momentum-loading terms, which describes the change in momentum of species *i* due to elastic

charge-exchange collisions between ions and neutrals, where υ_{in} is the ion-neutral collision frequency and $\boldsymbol{U_n}$ is the neutral velocity. Term C is the change in momentum due to the creation of new plasma moving at the velocity of the neutrals. Finally, $\sum Q_{in}$ is the heat addition term due to plasma-neutral interactions.

$$A = (S_i - L_i)m_i \tag{4a}$$

$$B = \rho_i \upsilon_{in}(\boldsymbol{U_n} - \boldsymbol{V_i}) \tag{4b}$$

$$C = m_i S_i(\boldsymbol{U_n} - \boldsymbol{V_i}) \tag{4c}$$

We assume that all negative charge carriers are electrons. The conservation of mass for electrons is satisfied by the assumption that the plasma is quasi-neutral, $\sum_i n_i \approx n_e$. The low mass of the electrons relative to the ions results in a very high electron gyrofrequencies, and hence very small characteristic timescales, thus we consider only the drift velocity of the electrons. The dynamics of the electrons are therefore entirely determined by Equations 5 and 6 which are respectively the equation of state for the electrons, and a modified Ohm's law describing the evolution of the electric field, where $\eta(\hat{\boldsymbol{r}})$ is the local resistivity (only non-zero in the ionosphere). The final plasma-neutral interaction term is $\sum Q_{en}$ in Equation 5, the electron fluid heat addition term which couples the plasma-neutral interactions to the evolution of the electron fluid.

$$\frac{\partial P_e}{\partial t} = -\gamma \nabla \cdot (P_e \boldsymbol{V_e}) + (\gamma - 1)\boldsymbol{V_e} \cdot \nabla P_e + \sum Q_{en} \tag{5}$$

$$\boldsymbol{E} = -\sum_i \frac{n_i}{n_e} \boldsymbol{V_i} \times \boldsymbol{B} + \frac{\boldsymbol{J} \times \boldsymbol{B}}{e n_e} - \frac{\nabla P}{e n_e} + \eta(\hat{\boldsymbol{r}})\boldsymbol{J} \tag{6}$$

Equation 7 is Faraday's law of induction, which is solved for evolution of the magnetic field while Equation 8, Ampere's law, is used to calculate the current density. Equation 9, uses the definition of current as the differential motion of charges to obtain the bulk electron velocity and thus close the system of equations.

$$\frac{\partial \boldsymbol{B}}{\partial t} = -\nabla \times \boldsymbol{E} \quad (7)$$

$$\boldsymbol{J} = \frac{1}{\mu_0} \nabla \times \boldsymbol{B} \quad (8)$$

$$\boldsymbol{V_e} = \frac{1}{n_e}\left(\sum_i n_i \boldsymbol{V_i} - \frac{\boldsymbol{J}}{e}\right) \quad (9)$$

3.4 Modeling neutral cloud interactions

Terms A, B, and C, $\sum Q_{in}$, and $\sum Q_{en}$ must be modeled as functions of the plasma properties and the density and velocity of the neutrals in order to successfully capture the temporal and spatial variability of the plasma-neutral interactions. Rather than consider the full list of all possible plasma-neutral and photon-neutral reactions that may occur, we begin with a subset of the most important interactions, shown in Table 2. This subset was compiled on the basis of which species were most abundant and which reactions had the fastest rates [*Burger et al.*, 2007; *Fleshman et al.*, 2010]. Saturn's neutral cloud is primarily composed of OH, which is produced from the photodissociation of H_2O sourced from Enceladus' cryovolcanic plumes ($H_2O + h\upsilon \rightarrow OH + H$). Photodissociation may also give rise to atomic O ($H_2O + h\upsilon \rightarrow O + H_2$, $OH + h\upsilon \rightarrow O + H$). H_2O dominates within 0.5 R_S of Enceladus' orbit, but its density rapidly falls with increasing distance (H.T. Smith, personal communication [2015]). Outside of this region, the relative abundances of the main water group neutrals in the cloud is $OH:O:H_2O$ = 10:10: 3 [*Fleshman et al.*, 2010]. Because of the dominance of water group neutrals and W+ ions in Saturn's inner magnetosphere where the neutral cloud interactions primarily take place, we restrict our modifications of the multifluid equations to the W+ fluid alone.

We model the interactions listed in Table 2 because those are the most important in terms of governing the global dynamics of Saturn's magnetosphere. However, there are

Table 2 List of neutral cloud interactions incorporated into modified multifluid model

Reactions	Type
$OH + h\upsilon \rightarrow OH^+ + e^-$	photoionization
$O + e^- \rightarrow O^+ + 2e^-$	electron-impact ionization
$OH + e^- \rightarrow OH^+ + 2e^-$	electron-impact ionization
$H_2O + e^- \rightarrow H_2O^+ + 2e^-$	electron-impact ionization
$H_2O + OH^+ \rightarrow H_2O^+ + OH$	elastic charge-exchange collision
$H_2O + H_2O^+ \rightarrow H_2O^+ + H_2O$	elastic charge-exchange collision

also other plasma-neutral interactions that occur in Saturn's magnetosphere that are important to certain regions of interest. One particular interaction is the charging of nanoscale grains of ice and dust that originate from the Enceladus plumes [*Morooka et al.*, 2011]. The presence of negatively charged dust has important implications for the flow of plasma in the vicinity of Enceladus, as described by *Kriegel et al.* [2011] and [*Simon et al.*, 2011]. However, these effects generally act on length scales far below what we can resolve using the global model and grid described in this document. As a result, we neglect these effects in the model results describe herein, leaving studies on the implications of these effects on global dynamics to future investigators.

3.4.1 Source terms

Together, photoionization and electron impact ionization make up the processes that comprise the source term S_i in terms A and C of Equations 1 and 2. Based on the significantly smaller rate constants for loss processes found by *Fleshman et al.* [2010], we have assumed that the loss rate L_i is generally much lower throughout most of the inner magnetosphere. Also, since we are only considering the reactions in Table 2, only

source rate we are interested in is the volumetric rate of water-group (W+) ion production, or S_{W+}.

Photoionization

We have simplified our model by treating the neutral cloud as being composed entirely of OH for the purposes of simulating photoionization. Thus photoionization is treated as being dependent solely on the rate coefficient for ionization of OH by UV photons (see Table 1) at 9.6 AU for the quiet Sun, $k_{ph} = 3.7 \times 10^{-9}$/s, as obtained from *Huebner et al.* [1992]. The model allows us to easily modify the rate coefficient to reflect different conditions such as solar maximum or Saturn's aphelion. Treating all three major constituents of the neutral cloud as OH is reasonable since the rate coefficients for the photoionization of O, OH, and H_2O are all within approximately 50% of the stated value above [*Fleshman et al.*, 2010], and the global rate of photoionization is an order of magnitude smaller than electron-impact ionization, making it a significantly weaker driver of magnetospheric dynamics.

Electron impact ionization

Electron impact ionization of the neutral cloud is by far the largest contributor to global mass-loading in Saturn's magnetosphere. The electron ionization frequency υ_e is dependent upon the local electron density n_e, and the rate constant κ_e, and is given by $\nu_e = n_e\, \kappa_e(T_e)$. To go from υ_e to the actual source rate per unit volume, we multiply by the local neutral density:

$$S_i = n_n\, \upsilon_e \tag{10}$$

The rate constant is dependent on the impact ionization cross-section σ_e, and the temperature of the local electron population, shown in Equation 11 below:

$$\kappa_e(T_e) = \int \sigma_e(T_e) v\, f(v) dv \quad (11)$$

where *v* is the electron thermal velocity, and *f(v)* is phase-space thermal velocity distribution. Recent work has shown that the distribution that best models the plasma in Saturn's inner magnetosphere may be a Kappa distribution [*Pierrard and Lazar*, 2010; *Carbary et al.*, 2014]. This is a non-thermal distribution, a modification of the Maxwellian distribution which allows for an increased abundance of higher-energy particles in the tail of the distribution. Nevertheless, we assume a Maxwellian instead of a Kappa distribution for *f(v)* for two major reasons: 1) it simplifies the computation of κ_e at each grid point, since the Kappa distribution requires numerical integration, and would slow the simulation to untenable levels, and 2) using a Kappa distribution would require assigning a fixed value for the kappa parameter to each grid point, which would have to be drawn from previous studies and which would prevent our simulation of electron-impact ionization from being self-consistent. We examined cross-section data for the electron impact ionization of each major species, O [*Johnson et al.*, 2005], OH [*Tarnovsky et al.*, 1998], and H_2O [*Itikawa and Mason*, 2005] (see Table 2) and determined that across most of the range of interest (13-150 eV), the cross-sectional values at a given energy were all within 33% of one another, as shown in Figure 3.2. We therefore made another simplifying assumption, and used the cross-section values for OH for the electron-impact ionization calculations for all water group neutrals.

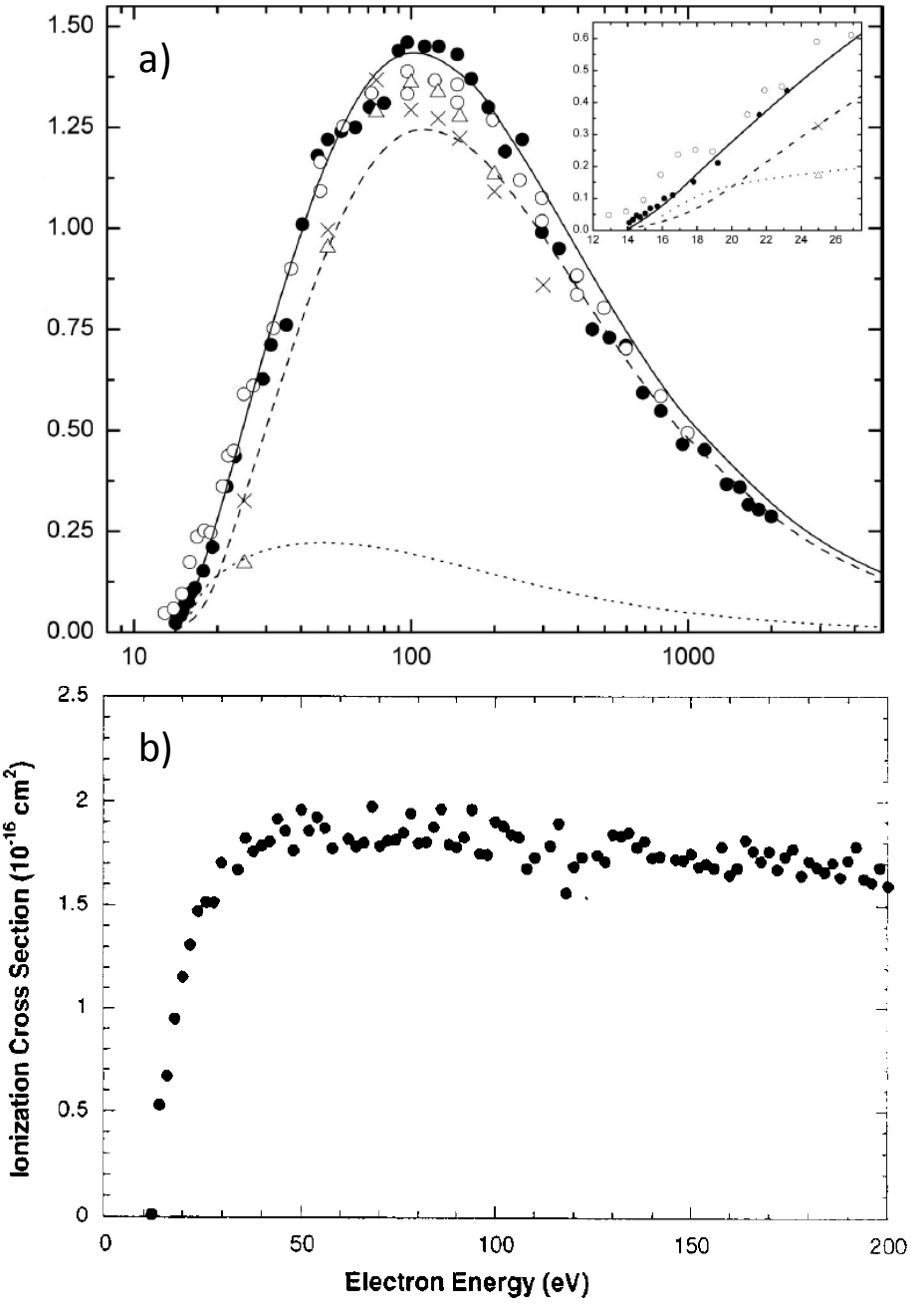

Figure 3.2 Single-electron ionization cross section of a) O (Source: *Johnson et al.* [2005]), and b) OH (Source: *Tarnovsky et al.* [1998])

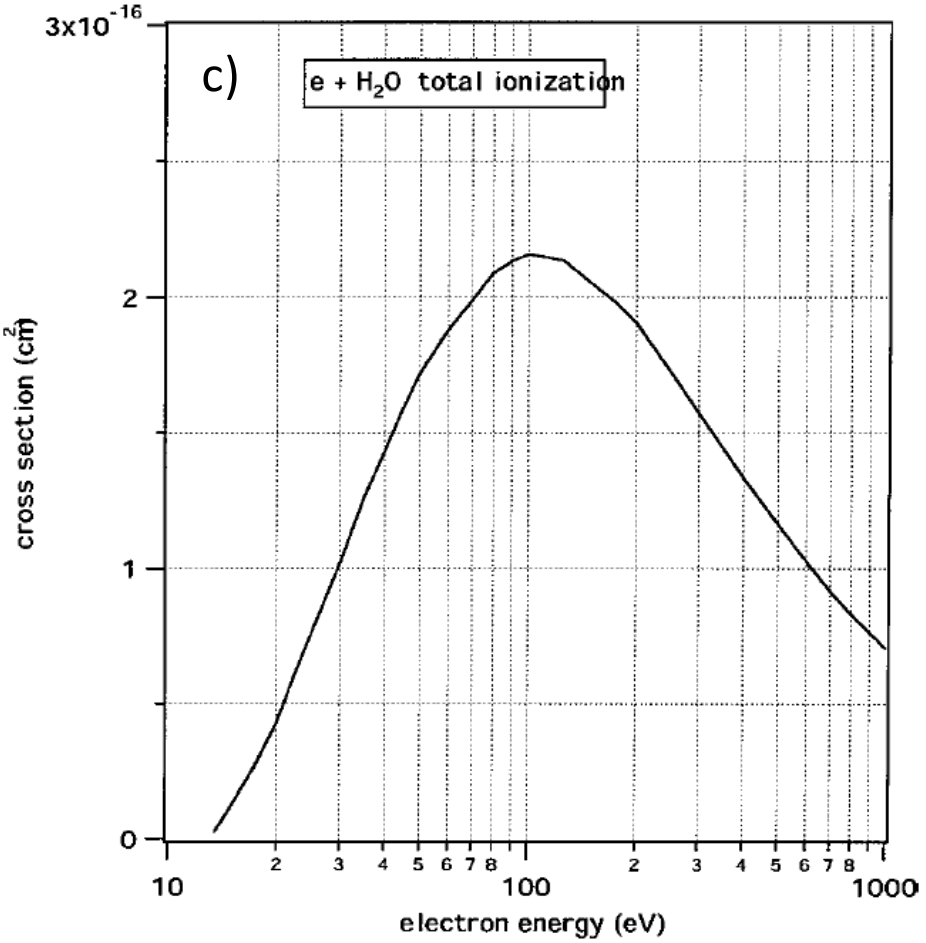

Figure 3.2 (continued) c) Single-electron ionization cross section of H_2O (Source: *Itikawa and Mason* [2005])

3.4.2 Ion-neutral elastic collisions

Elastic collisions between water groups ions and neutrals (i.e.: collisions resulting in symmetric charge exchange) result in a net loss of momentum from the ion fluid. The effects of these interactions are expressed in term B of Equation 2. The local time-dependent rate of these collisions υ_{in} depends upon the collision cross-section σ_{in}, the neutral and ion number densities, n_n and n_i, and the relative speed between the ions and neutrals $\Delta V = |\boldsymbol{V}_i - \boldsymbol{U}_n|$:

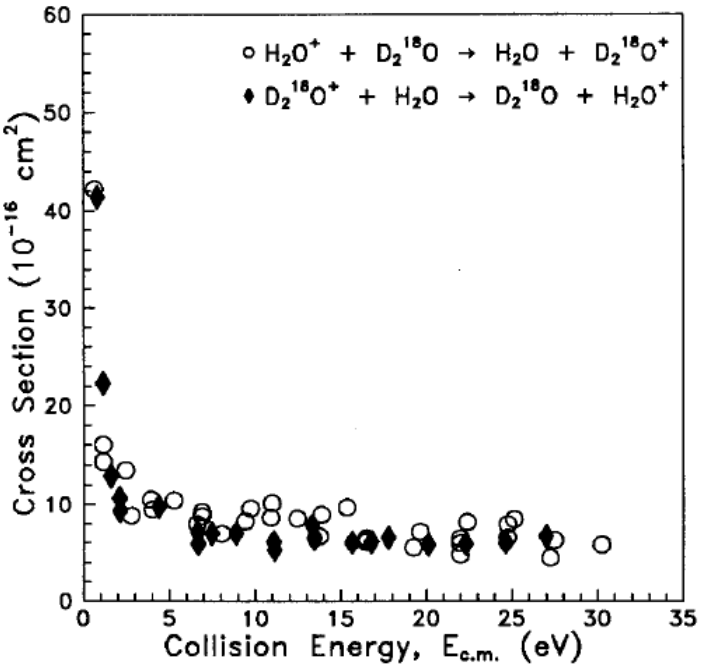

Figure 3.3 Charge exchange cross section (Source: *Lishawa et al.* [1990])

$$\nu_{in} = \sigma_{in}\, n_i\, n_n\, \Delta V \tag{13}$$

We calculate the velocity difference at each grid point and time step, assuming that the neutrals are traveling at Keplerian velocities. *Lishawa et al.* [1990] showed that not only were the collision cross-sections very close for both charge-exchange reactions shown in Table 1, but also that across the range of collision energies, the cross-sections were relatively unchanged as shown in Figure 3.3. We therefore used a mean cross-sectional value of $\sigma_{in} = 8 \times 10^{-16}$ cm^2, greatly simplifying the calculation.

3.4.3 Heat addition terms

The addition of new plasma from the neutral cloud results in a net loss of energy density from the plasma fluid, as the newly created ions are at essentially the same temperature as

the neutrals (practically zero, compared to the bulk ion temperature). Furthermore, elastic ion-neutral collisions result in energy exchanged from the plasma to the neutrals, with a fast (corotational) ion and a neutral at Keplerian speeds becoming a slow ion and a fast neutral. We employ the expression used by *Snowden and Winglee* [2013] to incorporate the change in W+ ion and electron fluid energy due to plasma-neutral interactions, the terms $\sum Q_{in}$ and $\sum Q_{en}$ from Equations 3 and 5 above, and refer the reader to the detailed discussion in that source.

3.4.4 A note on approximations

As we have explained above, we have made a number of approximations in order to reduce the total number of interactions that need to be incorporated into our model to manageable levels. Thus, in addition to the effects of discretization that affect all numerical fluid models, there are also uncertainties that arise from these approximations which primarily manifest within the mass- and momentum-conservation equations, as well as the equations of state (Equations 1-4). Most of this uncertainty arises from our averaging of the electron-impact ionization cross-sections described in Section 3.4.1 above, and our treating the individual water-group neutral and ion species (i.e.: O, OH, H_2O; O^+, OH^+, H_2O^+) as a single neutral or W+ ion species. There are likewise uncertainties arising from the assumption of a single change-exchange collision cross-section as described in Section 3.4.2.

We made the decision to use these approximations because, as noted earlier, the variability in cross-sectional values for the above reactions is on the order or 33% or less. This is generally much less than the observed variability in important quantities such as plasma densities, pressures, and temperatures, and magnetic field strengths and directions

throughout most of the Saturn's magnetosphere. As a result, we believe that the effects of our approximations on the physics are likely far less important than the variability produced by the dynamic behavior in our simulation domain. Moreover, as we go on to show in the remainder of this dissertation, the results of our simulations incorporating these modifications exhibit excellent agreement with the *in situ* data. Thus the uncertainties introduced by these approximations appear to be well constrained and do not inhibit the accurate simulation of Saturn's magnetosphere.

3.5 Empirical representation of the neutral cloud

We began our simulations with an azimuthally-symmetric empirical representation of the neutral cloud based on the results by *Jurac et al.* [2002]. We have since generalized the model to enable the inclusion of any neutral cloud morphology. For the purposes of this investigation, we use a representation from H.T. Smith (personal communication [2015]), which is an updated version of the neutral cloud model from *Smith et al.* [2010]. This representation is the result of populating the inner-magnetosphere with neutrals using a Monte Carlo method, ejecting H_2O molecules from Enceladus and then calculating their trajectories based on the physical and chemical processes acting upon them. Like the older representation, this is azimuthally symmetric, as shown in Figure 3.2. Compared to the model from *Jurac et al.* [2002], this version has much higher densities in the vicinity of Enceladus' orbit, and is both more confined radially, and more expanded in z. In both representations, neutral densities rapidly decay to zero inwards of $r = 4\ R_S$, due to absorption by the rings. Since the neutral cloud varies on much longer timescales than those relevant to the plasma (e.g.: corotation, advection,

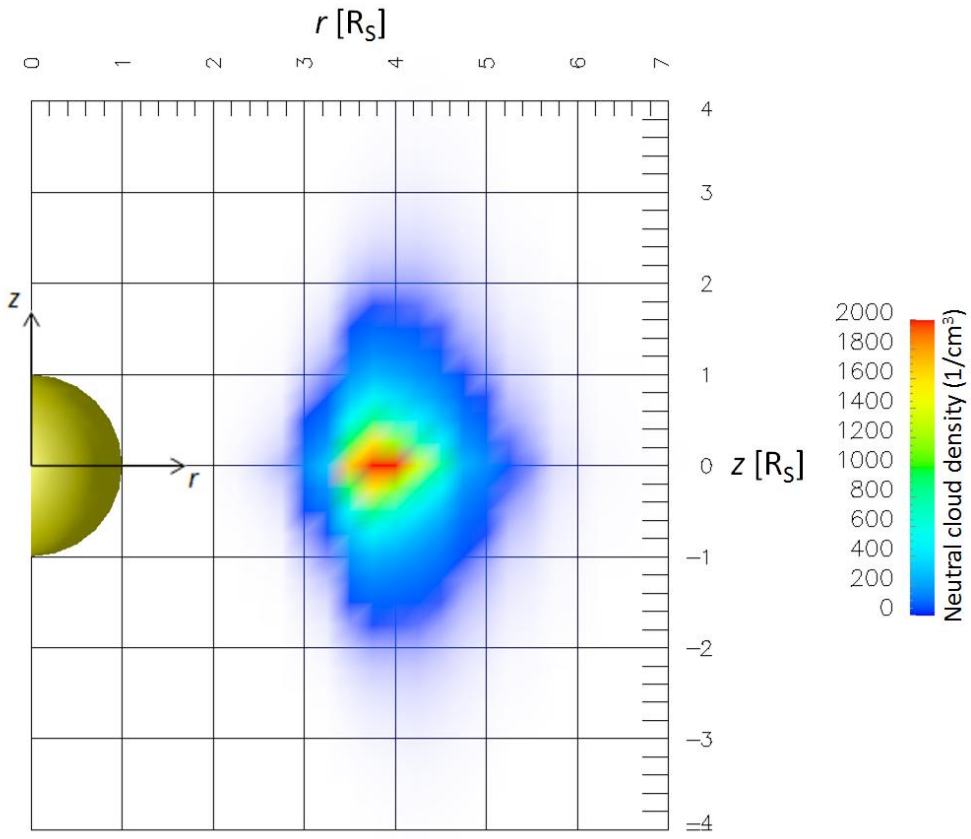

Figure 3.4 Density contours of extended Enceladus neutral cloud representation based on modeling by H.T. Smith. Cloud is azimuthally symmetric, all neutrals at treated as W+ (combination of O, OH, and H_2O)

and reconnection timescales), we treat the cloud as a static source of new ions with unchanging distribution in time.

3.6 Interior boundary and solar wind conditions

The inner boundary of the Saturn model is located at 2.25 R_S from the center of the planet, outside the main rings. The interior dipole field is initialized in the "ionosphere" nodes, just inside the inner boundary, such that $B_{eq}(r = 1\ R_S) = 21{,}000$ nT. The rotation rate is set by restricting the plasma in the ionosphere nodes to move in strict

corotation with Saturn (i.e.: a rotation period of 1 T_S). We do not presently maintain a non-zero ionospheric resistivity. As a result magnetosphere-ionosphere coupling is not current limited (i.e.: field-aligned currents which close through the ionosphere are not affected by the $\eta(\hat{\boldsymbol{r}})\boldsymbol{J}$ term in Equation 6). The lack of a current-limited ionosphere has often led to physically-inaccurate supercorotation in models of large rotationally-driven magnetospheres [*Moriguchi et al.*, 2008; *Kidder et al.*, 2009; *Jia and Kivelson*, 2012]. *Chané et al.* [2013] suggest a potential solution whereby they implement the inner-boundary by modeling the interaction of the plasma with the neutrals in the ionosphere. By doing so, they have produced the first global MHD model accurately depicting corotation lag in the Jovian magnetosphere using this method. We note that our self-consistent incorporation of plasma-neutral interactions with the Enceladus neutral cloud is similar in concept, and we show in Chapter 4 that the net effect of the new physics is to produce much better agreement with corotation lag profiles obtained from *in situ* data. Nevertheless, the inclusion of a physically-representative ionospheric conductance in the model is a topic of ongoing work.

The boundary formulation allows outward ion flux from the interior, but maintains the interior densities and pressures at the same levels. Thus, outward flux at the boundary is driven by pressure gradients and numerical diffusion. Our original intent was to set W+ density in the interior at a negligible level. However, in order to avoid both untenably high Alfven speeds close to the inner boundary which would adversely impact simulation performance, and very large density gradients which would drive excess numerical diffusion, it was necessary to specify a reasonably high water group ion density both inside and on the inner boundary. As a result, we still maintain an interior

W+ source. This is the primary W+ source for previous iterations of the Saturn multifluid model, but in this version it is much reduced, allowing the neutral cloud to dominate the production of new plasma (see Figure 5.6 for magnitude of ionospheric source).

For all results presented in Chapters 4 and 5, the incoming solar wind and IMF conditions were set to values appropriate to Saturn at southern hemisphere solstice, and are constant in time. The solar wind velocity is 450 km/s, and flows roughly anti-Sunward at a 26° angle from the *x*-*y* plane ($\boldsymbol{V}_{sw}$ = [400,0,200] km/s). This was the angle of attack (AOA) of the solar wind relative to Saturn in 2003-2004, shortly before Cassini's Saturn Orbital Insertion (SOI) phase. Thus, our simulation data in these chapters can be reasonably compared to *in situ* observations from the Cassini prime mission. The solar wind is composed primarily of protons, with negligible W+ and hvy+ components (required, since the fluid density cannot be zero), with a density of 0.1 cm^{-3} and a temperature of 140 eV. The only non-zero IMF component in these chapters is B_z = -0.25 nT, parallel to the interior field at the magnetopause, thus producing a closed magnetospheric configuration. The simulations are run for as long as possible (usually several T_S), with the time at the point that quasi-equilibrium has been reached designated as 0 hrs UT.

In Chapter 6, we consider the impact of seasonal variability as expressed by changes in the solar wind AOA. We maintain the solar wind density, temperature, and speed at previous values, as well as the same IMF, but change the incoming solar wind velocity vector $\boldsymbol{v}_{sw}$ to select a particular AOA value (e.g.: $\boldsymbol{V}_{sw}$ = [450,0,0] km/s at equinox). Once again, we wait for the magnetosphere to reach a quasi-equilibrium state before beginning in-depth observations.

In our study of tail dynamics in Chapter 7, we obtained all our data for the equinox case, as the mean plasma sheet is aligned with the rotation equator and the *x*-*y* plane, which makes visualization and the placement of virtual spacecraft (specific points on the grid from which a range of data is collected at every time step) a much simpler task. We applied a step-change in the IMF B_z component from -0.25 nT to 0.25 nT (parallel [closed] to antiparallel [open]). We designated the time at which we applied this flip as 0 hrs UT for this instance of the simulation.

CHAPTER 4

VALIDATION OF SIMULATION RESULTS

4.1 Global morphology of Saturn's magnetosphere

Due to the large number of modifications made to the basic multifluid model, we begin by presenting a series of comparisons to data to demonstrate both the model's fidelity to CAPS and MAG data as well as those regions in which the model results diverge from observations. Previous model results, including both the University of Michigan's BATSRUS model [*Hansen et al.*, 2005] and the University of Washington's multifluid code [*Kidder et al.*, 2009] have successfully reproduced the curved plasma sheet configuration observed at solstice. Figure 4.1a shows *x*-*z* plane H+ pressure contours and Saturn's magnetic field in the day-night meridian, illustrating the typical global configuration of Saturn's magnetosphere at solstice. Note that the simulation maintains the curvature of the plasma sheet after the addition of photoionization, electron-impact ionization, and elastic ion-neutral collisions. The subsolar magnetopause standoff distance, denoted by the blue star, is located at approximately 22 R_S, on the lower end of the range given by *Achilleos et al.* [2008], who found a bimodal distribution of standoff distances with peaks at 22 and 27 R_S. The equatorial plane (Figure 4.1b) shows a typical flow field for the bulk plasma for all modeled plasma species, $\boldsymbol{V}_b$, ($\boldsymbol{V}_b = \sum_i \rho_i \boldsymbol{V}_i, / \sum_i \rho_i$). The inner magnetosphere is dominated by azimuthal flows, both anti-Sunward and cross-tail flows are visible on the dawn flank, the latter enforcing the azimuthal flow in this region, while the dusk flank is largely characterized by anti-Sunward flows. The bend-back of most of the magnetic

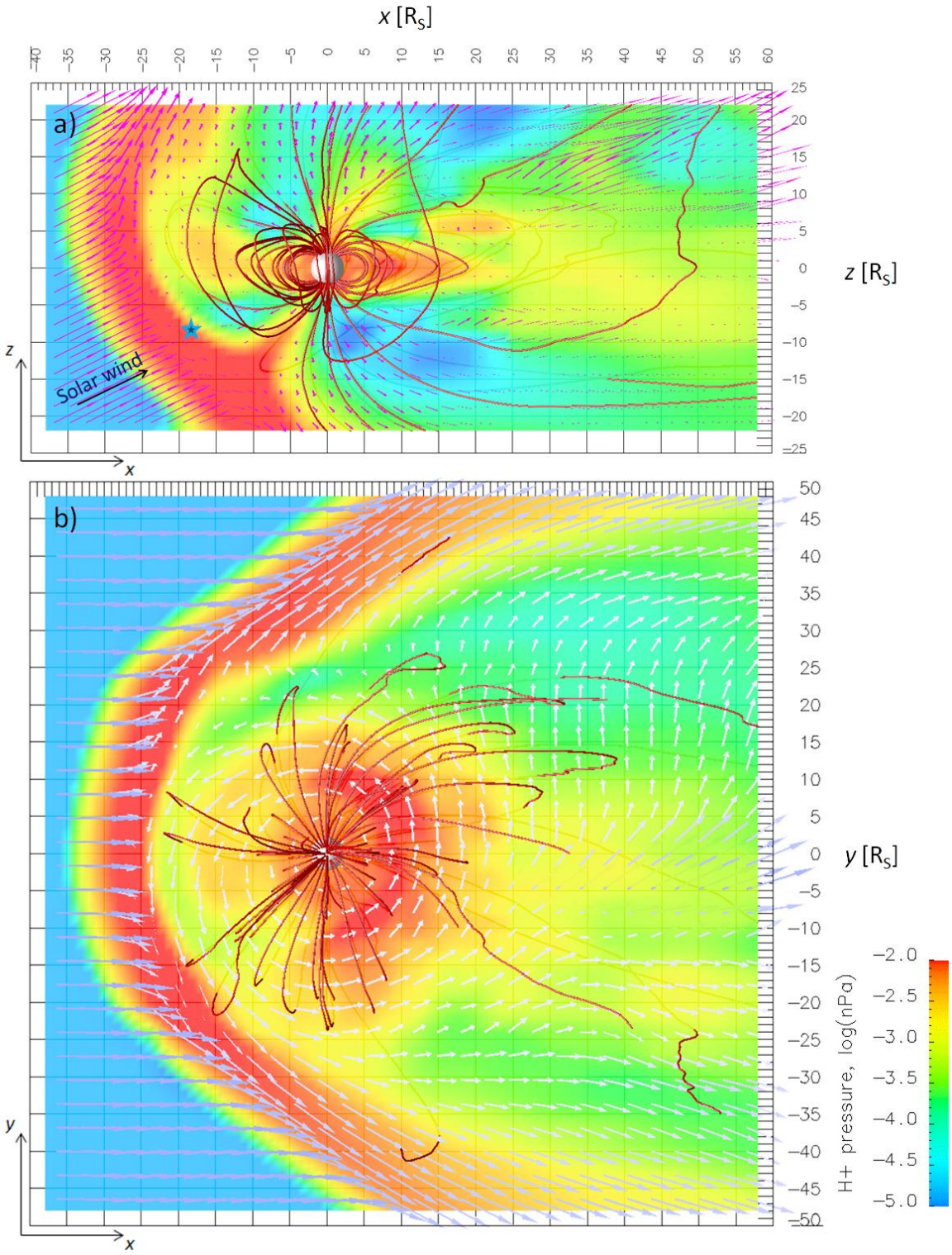

Figure 4.1a) meridional and b) equatorial view of global morphology of Saturn's magnetosphere. Vectors represent the density-averaged total plasma velocity, contours show proton pressure, field lines represent the magnetic field inside the magnetopause, blue star represents subsolar magnetopause standoff distance.

field lines in the inner magnetosphere implies a largely sub-corotational flow field (see Figure 4.4 and accompanying description). The apparent inner-magnetosphere pressure enhancement observed on the nightside is not a permanent structure, rather it is a dynamic feature that develops and dissipates with the evolving flow field.

4.2 Comparison with *in situ* data

Having examined the reproduction of the large-scale structure of Saturn's magnetosphere, we now explore the plasma parameters in the inner and middle magnetosphere, comparing the model output to Cassini data. The comparisons between simulation data and *in situ* observations below are only made possibly by both the use of a multifluid model, which allows differentiation between the properties of different ion fluids, and the incorporation of self-consistent neutral-cloud interactions, which dynamically evolves the local plasma variables in response to the production and transport of plasma. Figure 4.2 shows simulation results for density, pressure, and temperature in the equatorial plane of the two major ion fluids, protons and water group ions. The black lines represent the mean data, while the red bars represent the range of values at each radial location. The data have been averaged in both time and space, over approximately 4.25 Saturn rotations (45 hrs) with data sampled ten times per rotation, and radially along the noon-midnight and dawn-dusk meridians. We have overlaid the simulation results on the low-latitude, corotation field-of-view CAPS data from *Thomsen et al.* [2010] for comparison. The CAPS data are given as a function of L-shell. We restrict our comparison to CAPS data from passes where the instrument is pointed into the corotation field-of-view and when the spacecraft is at low latitudes in order to obtain the best representative comparison to our simulation results.

Figures 4.2a and b show radial equatorial-plane density and pressure profiles of the protons and W+ ions. Proton density decreases exponentially as radial distance increases, in agreement with the CAPS data throughout the range of radial locations. In general, the simulation results are on the higher end compared to the instrument data, a consequence of needing to maintain a high enough densities inside of 3 R_S to prevent extremely high Alfven speeds in this region (see Section 3.5). The simulated mean W+ density peaks at around 25-30 cm^{-3} slightly outside of the location of Enceladus' orbit

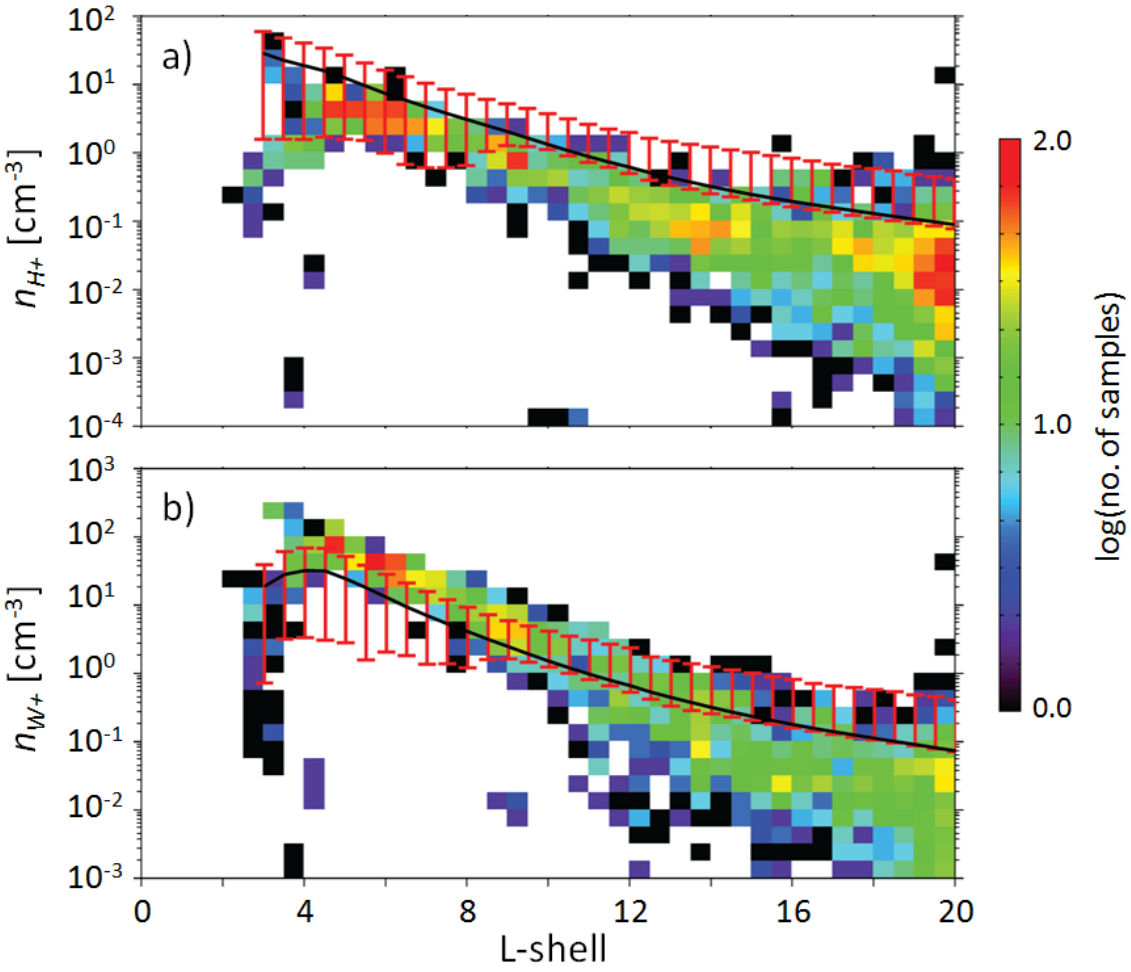

Figure 4.2 a) proton and b) W+ time-averaged radial density profiles at z = 0 overlaid on CAPS data (by L-shell) from *Thomsen et al.* [2010]

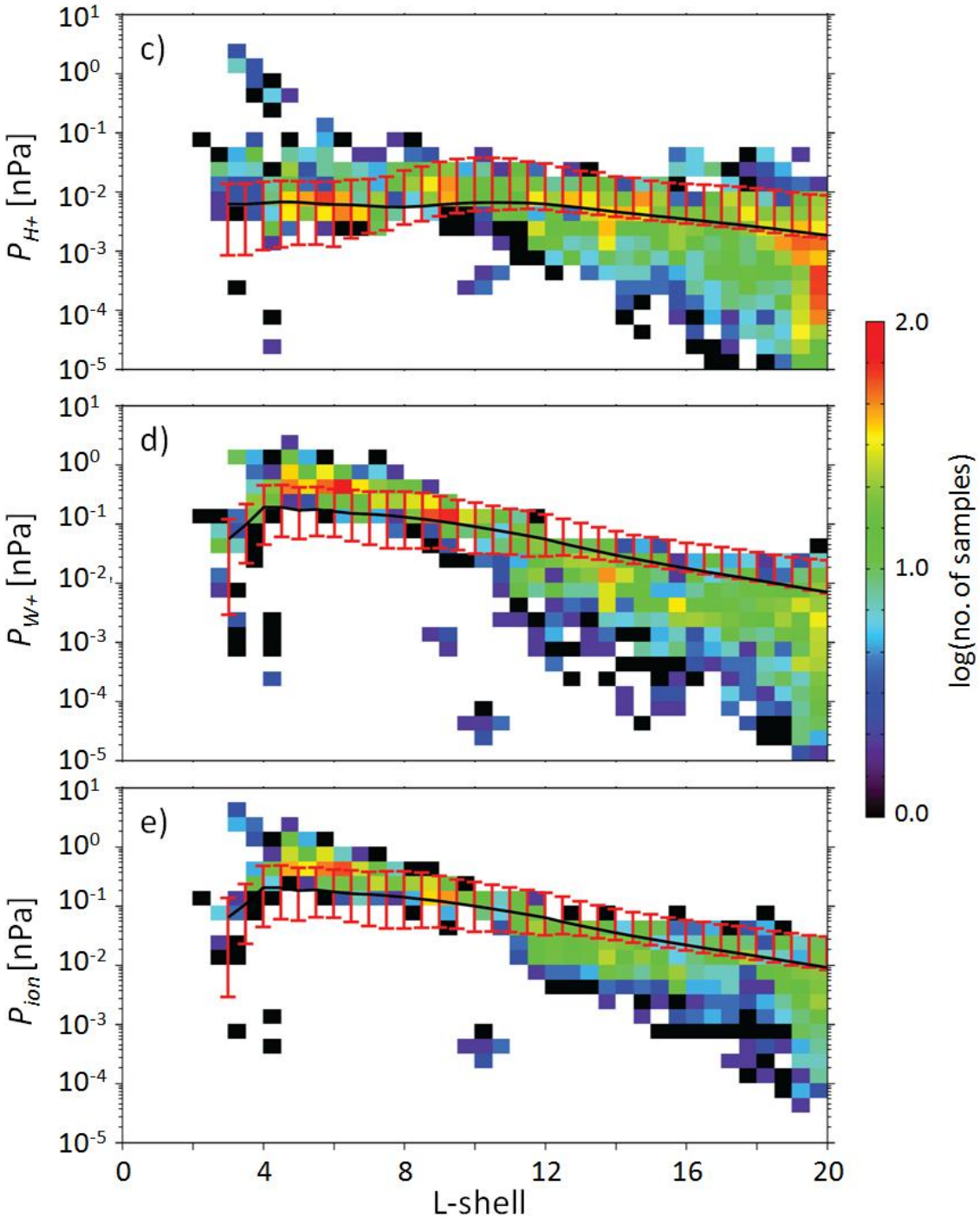

Figure 4.2 (continued) c) proton, d) W+, and e) total ion time-averaged radial pressure profiles at $z = 0$ overlaid on CAPS data (by L-shell) from *Thomsen et al.* [2010]

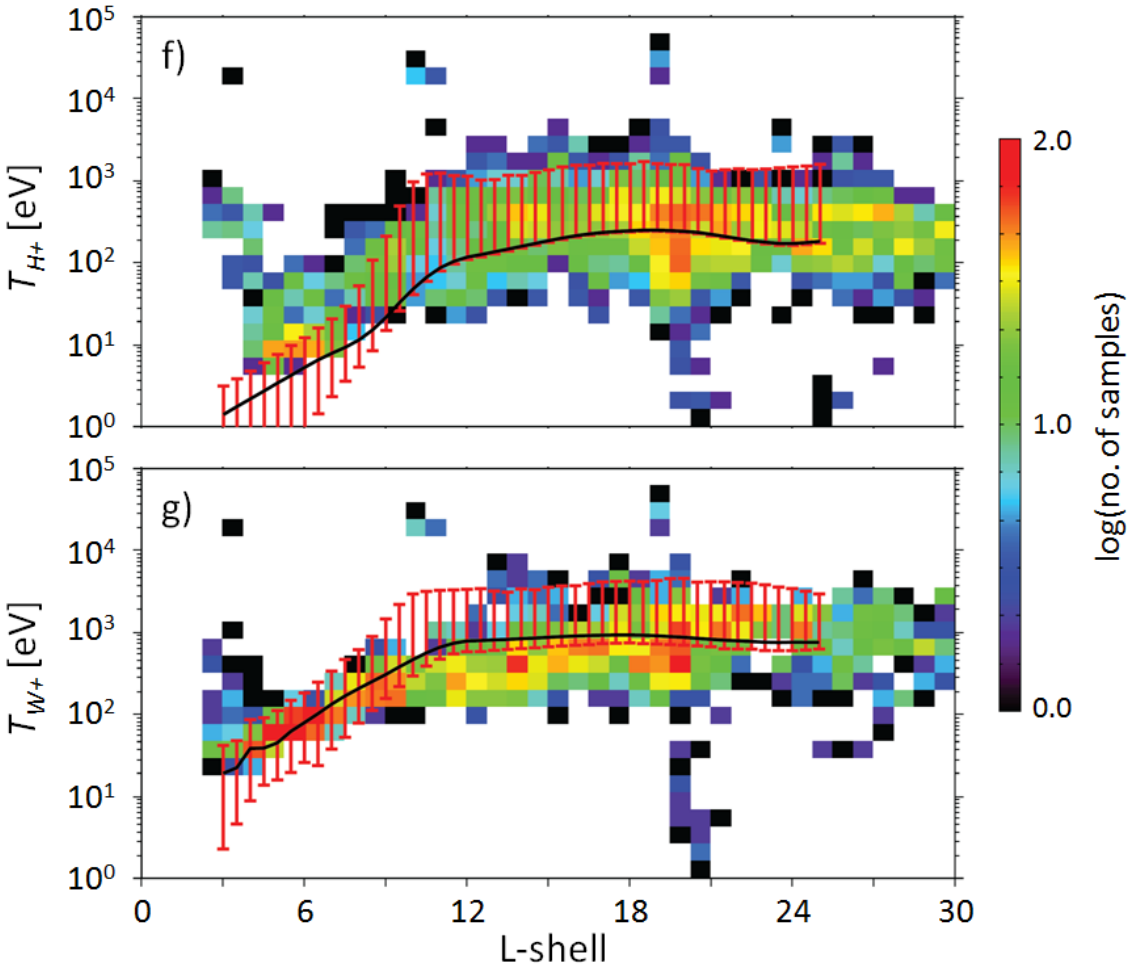

Figure 4.2 (continued) f) proton and g) W+ time-averaged radial temperature profiles at z = 0 overlaid on CAPS data (by L-shell) from *Thomsen et al.* [2010]

(r_{En} = 4 R_S). The location of the peak is consistent with observations, while the density profile for r < 8 R_S is in reasonable agreement with *in situ* data: somewhat lower than the mean CAPS values but within the bounds *in situ* data. Qualitatively, the simulation results show that W+ is the dominant ion species in the inner magnetosphere. The simulation and CAPS data are in excellent agreement outwards of 8 R_S.

The simulated radial pressure profiles for protons, W+, and the total ion population (Figures 4.2b, c, and d) are likewise in excellent agreement with the CAPS

data throughout the inner and middle magnetosphere. The proton pressure is in excellent agreement with spacecraft data, with values between 0.01-0.003 nPa observed throughout the inner and middle magnetosphere. W+ plasma pressure peaks at approximately 0.2 nPa in the vicinity of Enceladus' orbit, with a broad region where $P_{W+} > 0.1$ nPa extending between $4\ R_S < r < 9\ R_S$. Consistent with observations, the simulation data clearly shows that W+ pressure dominates the total plasma pressure in the inner and middle magnetosphere. Ion temperatures are derived from the density and pressure data, assuming an ideal gas law relationship. The simulation temperature results (Figures 4f and g) are therefore also reasonably consistent with the CAPS data, with the W+ plasma data showing excellent agreement. Proton temperatures inside of $r = 6\ R_S$ are lower than the observed values but this is expected, since the higher-than-average simulated proton densities in this region would act to depress the temperature.

Figures 4.3a and b show the magnetic pressure and electron temperature profiles respectively. Figure 4.3a is overlaid on the Rev 20 data from *Kellett et al.* [2011], which shows that our magnetic pressures are consistent with those measured by the MAG instrument early in the Cassini mission, further confirming that our model captures the overall conditions of Saturn's inner and middle magnetosphere. Figure 4.3b may be compared against inner-magnetosphere electron temperature data from *Persoon et al.* [2009], which shows that our electron temperatures are in good overall agreement with the observed values. This is of great importance to the accuracy of the updated model, as the electron temperature profile directly impacts the rate of plasma production due to electron-impact ionization, and therefore the mass- and momentum-loading processes.

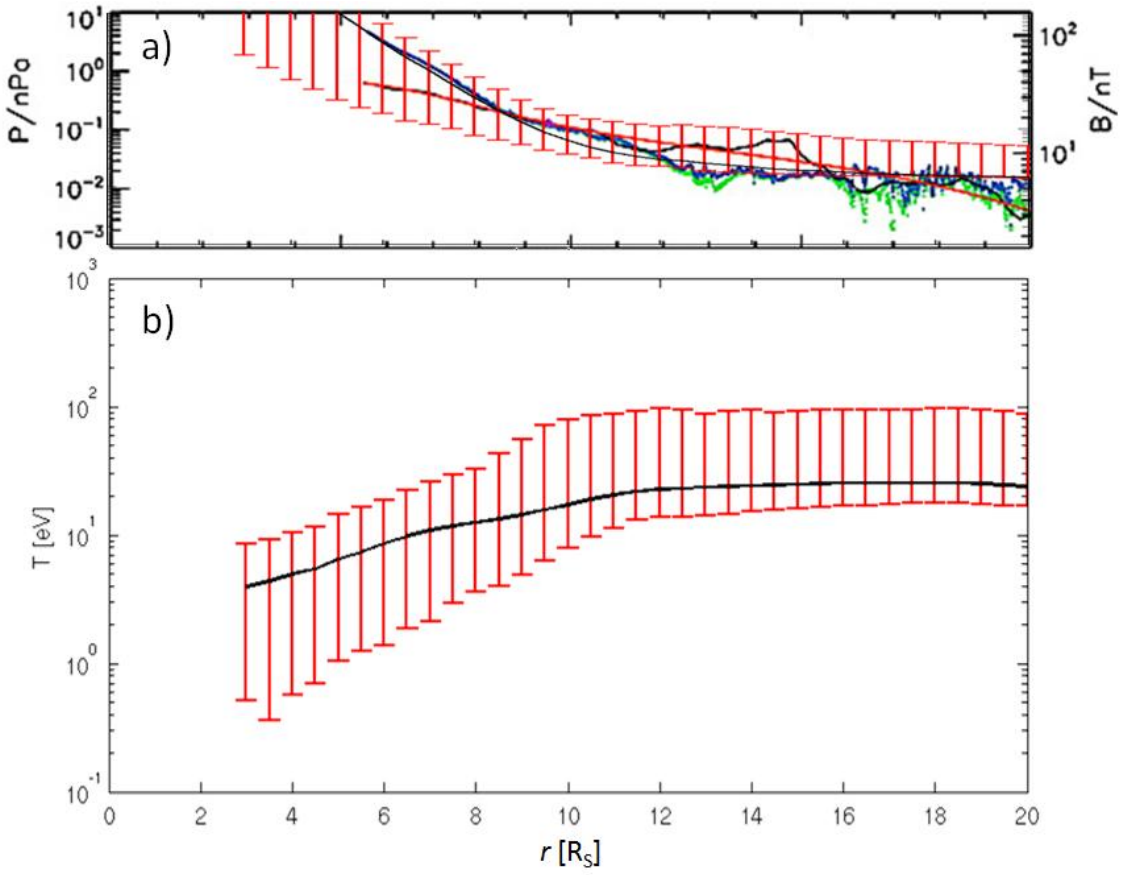

Figure 4.3 a) magnetic pressure and b) electron temperature time-averaged radial profiles at $z = 0$. Magnetic pressure data is overlaid on CAPS and MAG data for Cassini Rev 20 from *Kellett et al.* [2011]. Blue line in a) represents the magnetic pressure derived from MAG data.

The final stage of validating the updated model is comparing the corotation lag exhibited by the simulation with results derived from CAPS data. Figure 4.4 shows the time-averaged (same interval as Figures 4.2 and 4.3) radial corotation lag (v_φ/v_{corot}) profiles at dawn, noon, dusk, and midnight. Moderate supercorotation ($v_\varphi/v_{corot} < 1.2$) is evident between 7 $R_S < r < 12$ R_S at both midnight and dawn, but the rest of the inner and middle magnetosphere is subcorotational. Supercorotation at dawn may also be the result of intermittent high-speed return flows, based on findings from *Masters et al.* [2011].

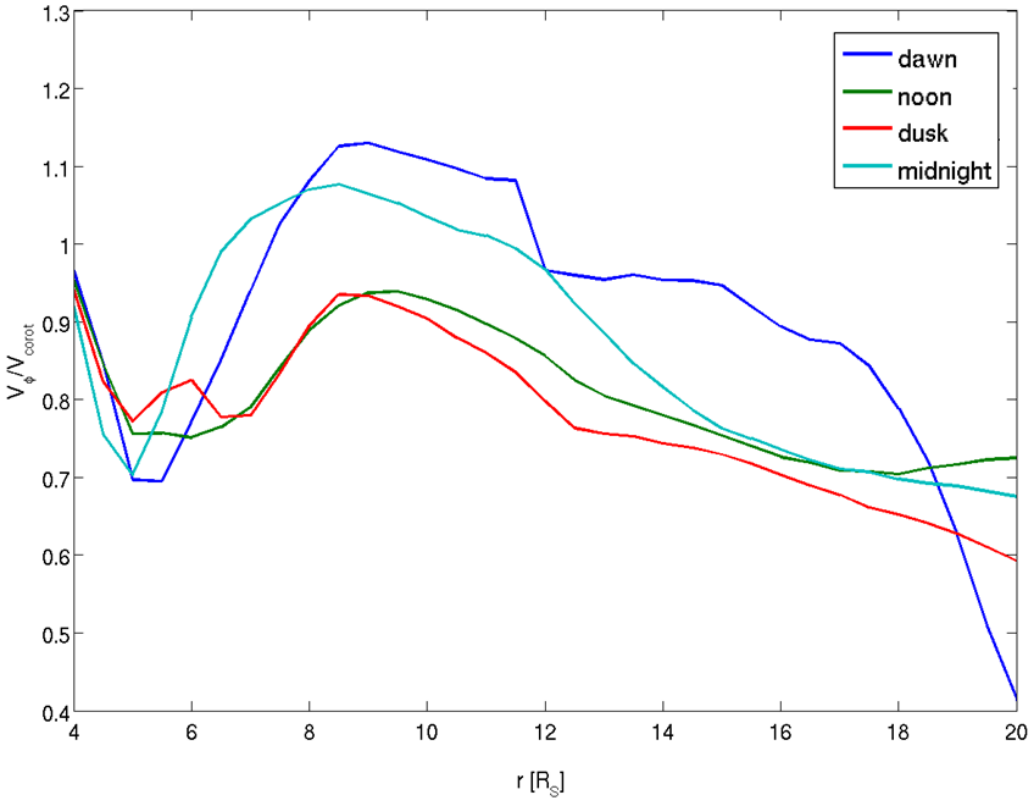

Figure 4.4 Corotation lag radial profiles at dawn (06:00 hrs SLT), noon (12:00 SLT), dusk (18:00 SLT) and midnight (24:00 SLT)

Furthermore, when compared with CAPS data from *Wilson et al.* [2009], the lag exhibited by our model is similar (~10-20% between 5 R_S < *r* < 10 R_S at noon and dusk). The largely subcorotational magnetosphere, coupled with the presence of swept-back flow structures is strong qualitative evidence that the updated multifluid model is a valid representation of Saturn's magnetosphere.

4.3 Summary of findings

We have compared the output of our updated multifluid model with published CAPS and MAG data from the Cassini prime mission, and have shown that the simulation is in good agreement with *in situ* data. In particular, the inner magnetosphere

radial profiles from the model output exhibit a fidelity to instrument data that has thus far not been achieved by previous investigators, implying that the inclusion of plasma-neutral interactions is essential for the quantitatively accurate simulation of Saturn's inner magnetosphere dynamics.

CHAPTER 5

PLASMA PRODUCTION AND RADIAL TRANSPORT IN SATURN'S INNER AND MIDDLE MAGNETOSPHERE

5.1 Water group plasma production

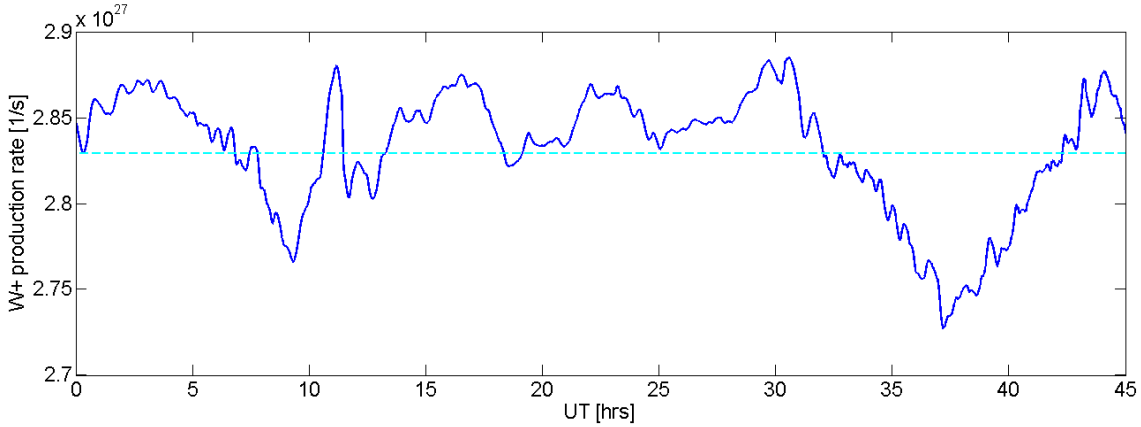

Figure 5.1 W+ ion production rate (blue solid line is the instantaneous rate in blue solid line; cyan dashed line represents time-averaged rate over the displayed interval)

New plasma in Saturn's magnetosphere is produced primarily by electron-impact ionization and photoionization of the neutral cloud. In this section, we examine mass- and momentum-loading during southern hemisphere solstice. Figure 5.1 shows global W+ production due to electron-impact ionization over 45 hours of simulation time (4.25 Saturn rotations) after the model has achieved equilibrium. The mean rate of plasma production due to electron-impact is 2.83×10^{27}/s (~80.5 kg/s), approximately fifteen times the rate of production due to photoionization (1.92×10^{26}/s, ~5.5 kg/s). The time-variability of electron-impact ionization over this interval is relatively low, less than 5%. There have been a wide range of estimates for the total, globally integrated rate of mass-loading based on analyses of Hubble Space Telescope and Cassini data, from as low 10

kg/s to as high as ~300 kg/s ([*Jurac and Richardson*, 2005; *Sittler Jr et al.*, 2008; *Cassidy and Johnson*, 2010; *Fleshman et al.*, 2010]). Our simulation results are thus consistent with observations, falling towards the lower end of this range.

Figure 5.2 shows an equatorial time sequence ($z = 0$) of the inner-magnetosphere electron temperature, electron-impact ionization frequency (υ_e, see section 2.2.1), and volumetric W+ production (S_{W+}) due to electron impact ionization for the interval 17.22 hrs < t < 26.71 hrs UT (0.9 T_S). The sphere in the center represents the inner boundary, while the white circle at r = 4 R_S represents the location of Enceladus' orbit. The inner magnetosphere may be divided into two separate regions in terms of spatial and temporal variability in the rate of electron-impact ionization: r < 5 R_S, where the variability in ionization rate is negligible, and r > 5 R_S, where significant spatial and temporal variability exist. It is in the low-variability region (3 R_S < r < 5 R_S) where the vast majority of new W+ plasma is produced ($S_{W+} > 10^{-4}$ cm^{-3} s^{-1}), despite the low local impact-ionization frequency in this region ($\upsilon_e < 1 \times 10^{-5}$/s). Since T_e < 10 eV in this region, only the sub-population of the tail of the thermal electron distribution is capable of ionizing the water group neutrals (T_e > 13.2 eV), implying that the high plasma production in this region is due simply to the very high local electron and neutral densities. The radial extent of this maximal production region is consistent with observations, confirming that it is the thermal electrons that are responsible for the bulk of new plasma production from the neutral cloud.

Most of the variability occurs in the region r > 5 R_S, with transient structures in the W+ production rate contours developing and dissipating over a matter of hours. An example is the protrusion at approximately 21:00 hrs Saturn Local Time (SLT) visible at

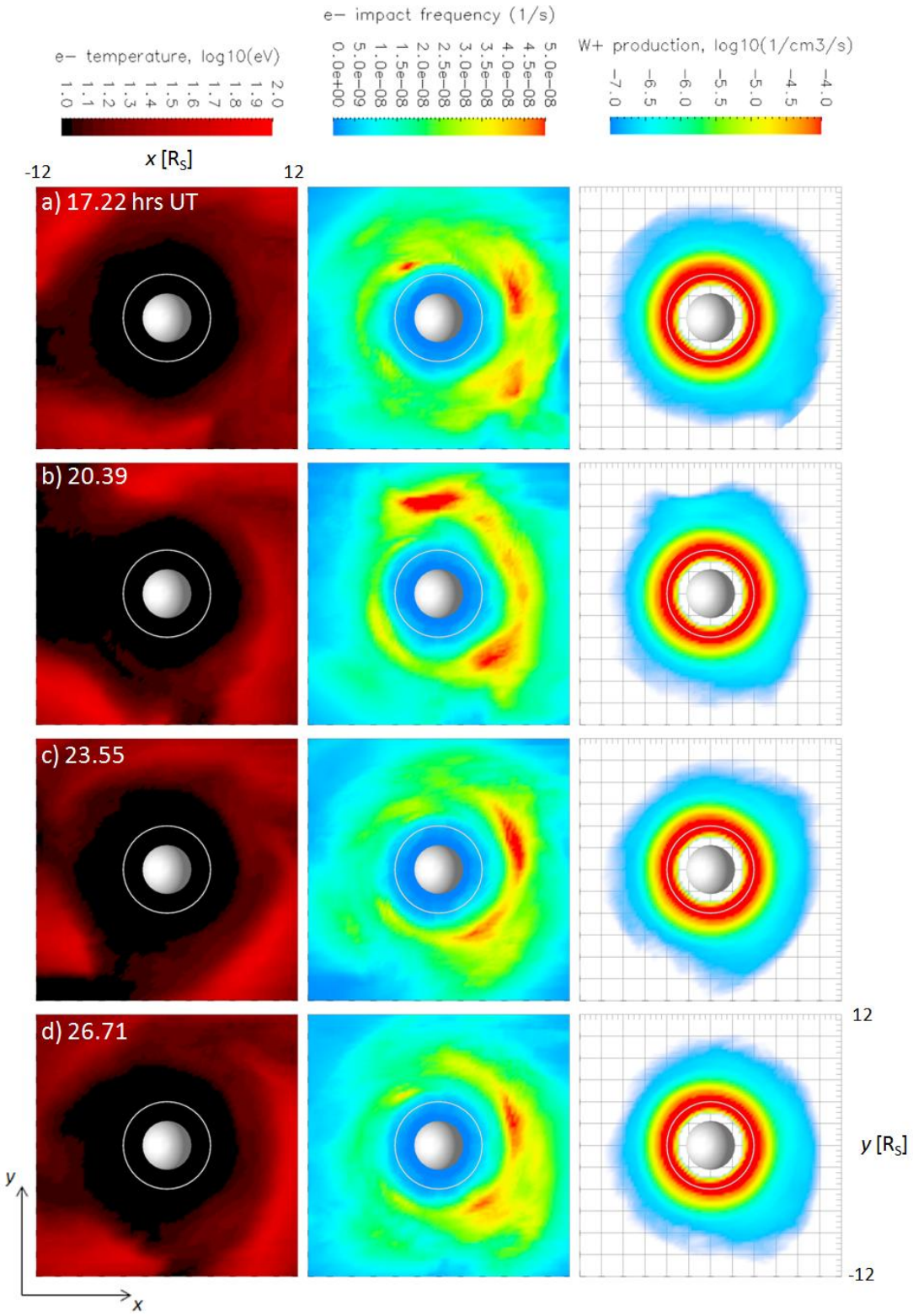

Figure 5.2 Equatorial time series (z = 0, looking down on Saturn's north pole) displaying (from L to R) electron temperature, electron impact ionization frequency, and W+ production rate for 0.9 Saturn rotations, a) 0 T_S, b) 0.3 T_S, c) 0.6 T_S, d) 0.9 T_S

0 T_S (Figure 5.2a), which roughly corotates with the planet and then dissipates before reaching midnight prior to 0.3T_S (Figure 5.2b). From Equation 10 and the fact that our neutral cloud representation is static, any variability that does arise must therefore be due to either changes in the local electron density or temperature. The dynamics of these features are therefore governed by the flows of warmer electrons (T_e > 10 eV) from the middle magnetosphere. One example of this is effect of the band of warm electrons that has just moved into the inner magnetosphere at a distance of r = 10 R_S at approximately 06:00 hrs SLT in Figure 5.2b. This, together with sufficiently high electron density in this region, produces the increased ionization frequencies in this region at the same time step, which in turn produces a co-located and very pronounced "bulge" of increased ionization at 06:00 SLT. At 0.6 T_S, this warm-electron region has advanced to approximately 15:00 SLT, the region of increased electron impact frequency and ionization has dissipated as it passed through the dayside. We observe that the largest ionization frequencies tend to occur on Saturn's nightside, which corresponds with the dayside densities of the hotter electrons sourced from the middle and outer magnetosphere being somewhat lower.. Please refer to Figure A1.1 in Appendix A1 for an animation of Figure 5.2 over the given time interval.

Note that the electron impact-ionization frequencies υ_e shown in Figure 5.2 are derived from assuming the electron temperatures have a Maxwellian distribution and are isotropic (see section 3.4.1). There has been debate in the community about the role of hot electrons in producing plasma: the density of hot electrons in the inner-magnetosphere, where neutral density peaks, is relatively low [*Schippers et al.*, 2008], but the large ionization cross-sections that they produce may be sufficient to compensate

for this. In order to investigate the effects of hot electrons on ionization rates, we implemented a data-informed, constant high temperature electron population in our model (T_e = 200 eV). This hot population density was treated as a radially-dependent fraction of the overall electron population as a function of L-shell using a profile from *Schippers et al.* [2008]. We found that this simple representation of the hot population produced very few W+ ions compared to the thermal population, due to the fact that the hot electron density for $r < 9\ R_S$ (where neutrals were most abundant) was extremely low. Since the effect of the increased ionization cross-sectional values of the hot population was unable to compensate sufficiently for its low abundance, we therefore neglected this phenomenon in our other model runs.

5.2 Radial transport

While the global rate of production exhibits little overall variation, the radial transport of plasma is a highly dynamic process, with flow features rapidly developing and decaying on time-scales much shorter than the planetary rotation period. *Kidder et al.* [2009] described radial transport in terms of the evolution of "fingers" of outward-flowing inner-magnetosphere plasma, using results from a version of the multifluid model featuring a constant source rate of new water group plasma. In this section, we present an updated description and analysis of this phenomenon using our model featuring self-consistent neutral cloud interactions.

We begin with a qualitative description of the radial outflow of water group plasma from the inner magnetosphere. Figure 5.3 is an equatorial time sequence showing the azimuthal and radial flow of the cold, dense inner magnetosphere W+ plasma, covering approximately the same time interval as Figure 5.2 with three times the

temporal resolution. The contours represent the plasma density, which peaks in a band extending between 3.5 $R_S > r > 5$ R_S, consistent with the region of highest W+ production (see Figure 4.3b). As in Figure 8, the inner circle represents the location of Enceladus' orbit, while the outer circle at $r = 15$ R_S is relevant to the calculation of radial flux in the next section. The purple arrows show the radial component of the total (density-weighted) plasma velocity.

Figure 5.3 shows that the outward flow of W+ plasma is a dynamic and highly variable process that operates primarily through the formation of outflow structures. These are regions of cold, higher-density, inner-magnetosphere W+ plasma which grow radially outwards over time. The radial velocity of plasma inside these regions is predominantly positive, thus transporting inner-magnetosphere plasma outwards. These structures are similar to the "fingers" described by *Kidder et al.* [2009], but with much greater azimuthal extent and exhibiting markedly different behavior as they evolve. The primary forces acting upon a mass-loaded flux tube are the magnetic field attempting to accelerate the plasma azimuthally and confine the plasma radially, and the outward centrifugal acceleration of the plasma, which is moving at speeds far in excess of Keplerian orbital velocities throughout most of Saturn's magnetosphere. Since the mass-loading processes are continuous, the centrifugal stresses dominate the magnetic field's ability to confine the plasma, resulting in the radially-outward flow of W+ ions observed in the outflow regions of Figure 5.3. The continuous rate of W+ production also prevents the plasma from reaching corotation velocities, which therefore lags behind the planetary rotation rate. This effect is also evident in Figure 5.3, in which the outflow structures display a distinct "swept-back" morphology. The amount of lag increases with the age

and therefore radial extent of the structure, consistent with our earlier results on corotation lag (see Figure 4.4) showing the rate of corotation lag increasing with radial distance. While the dayside magnetopause ($r \approx 25$ R_S on the dayside in Figure 5.3, not shown) acts to radially confine the growing outflow structures, the inability of the magnetic field to arrest radial flow results in the outward-moving inner-magnetosphere plasma and their associated magnetic flux tubes eventually reconnecting and leaving the magnetosphere on the nightside, which is required to avoid inflating the plasma sheet indefinitely. While we do not track the location of reconnection, Figure 5.3 shows a stable region at approximately 21:00 hrs LT where the direction of radial flow changes from negative to positive between $15\ R_S < r < 18\ R_S$. It is in this vicinity that we observe parcels of inner-magnetosphere plasma detaching and flowing tailward, strongly suggesting that this is how mass is shed from Saturn's inner magnetosphere. Finally, note that radial velocities are very small inside of 10 R_S (absence of vector implies $v_r < 10$ km/s), and increase radially outwards of this region. This is consistent with findings obtained from CAPS observations, both from forward modeling plasma moments [*Wilson et al.*, 2008] as well as inference based on the statistics of hot injection regions [*Chen et al.*, 2010].

The behavior of the outflow structures themselves is highly complex. We therefore qualitatively describe the initiation, development, and destruction of these structures over this time period, focusing on four specific outflow regions that are denoted by the colored markers: Regions 1 (purple), 2 (green), 3 (red), and 4 (yellow). Each structure is identified and marked by inspection. The markers are therefore intended to provide qualitative information about the development of a given outflow finger, and

do not represent the trajectory of a given fluid parcel over the time sequence. At the beginning of the sequence (Figure 5.3a, 0 T_S), Regions 1, 2, and 3 are visible, each at a different stage of development. Region 1 is at the beginning of its development, visible as a slight outward bulge of the main inner-magnetosphere plasma distribution. Centrifugal forces cause this structure to steadily grow in radial extent, with sweep-back signifying increasing corotation lag becoming apparent by 0.2 T_S (Figure 5.3c), as the structure moves through the dawn-dusk meridian. Region 1 continues to grow radially as it rotates around the planet, until it is confined by the magnetopause on the dayside (Figure 5.3e-g, 0.4-0.6 T_S). Sweep-back continues to increase over this period, as shown by the long, rarefied tail extending from Region 1. By 0.9 T_S (Figure 5.3j), the bulk of Region 1 has crossed the dawn-dusk meridian on the dusk side, and has grown to extend more than 25 R_S in the radial direction. Between 1.0 and 1.1 T_S (Figures 5.3i-j), the distended Region 1 enters the area of stable radial flow reversal at around 21:00 hrs LT described above, whereby the bulk of its plasma outside of 15 R_S streams radially away from the planet.

The evolution of Region 1 may be viewed as typical of the lifecycle of an outflow structure: most begin to grow in the late midnight/early dawn sector, and lose much of their mass as they pass 21:00 LT. Region 2 (green), an outflow structure with well-developed sweep-back in the dusk sector at 0 T_S, develops in a similar manner, expiring between 0.3 and 0.4 T_S having shed much of its mass. However, more complex behavior can arise as exhibited by Regions 3 and 4. At the beginning of the time sequence, Region 3 (red) is already in the process of sweeping through the dayside sector. Unlike Region 1, this structure does not simply grow through increased radial extent and sweep-back, but instead appears to inflate over time. As a result, by the time it encounters the reversed-

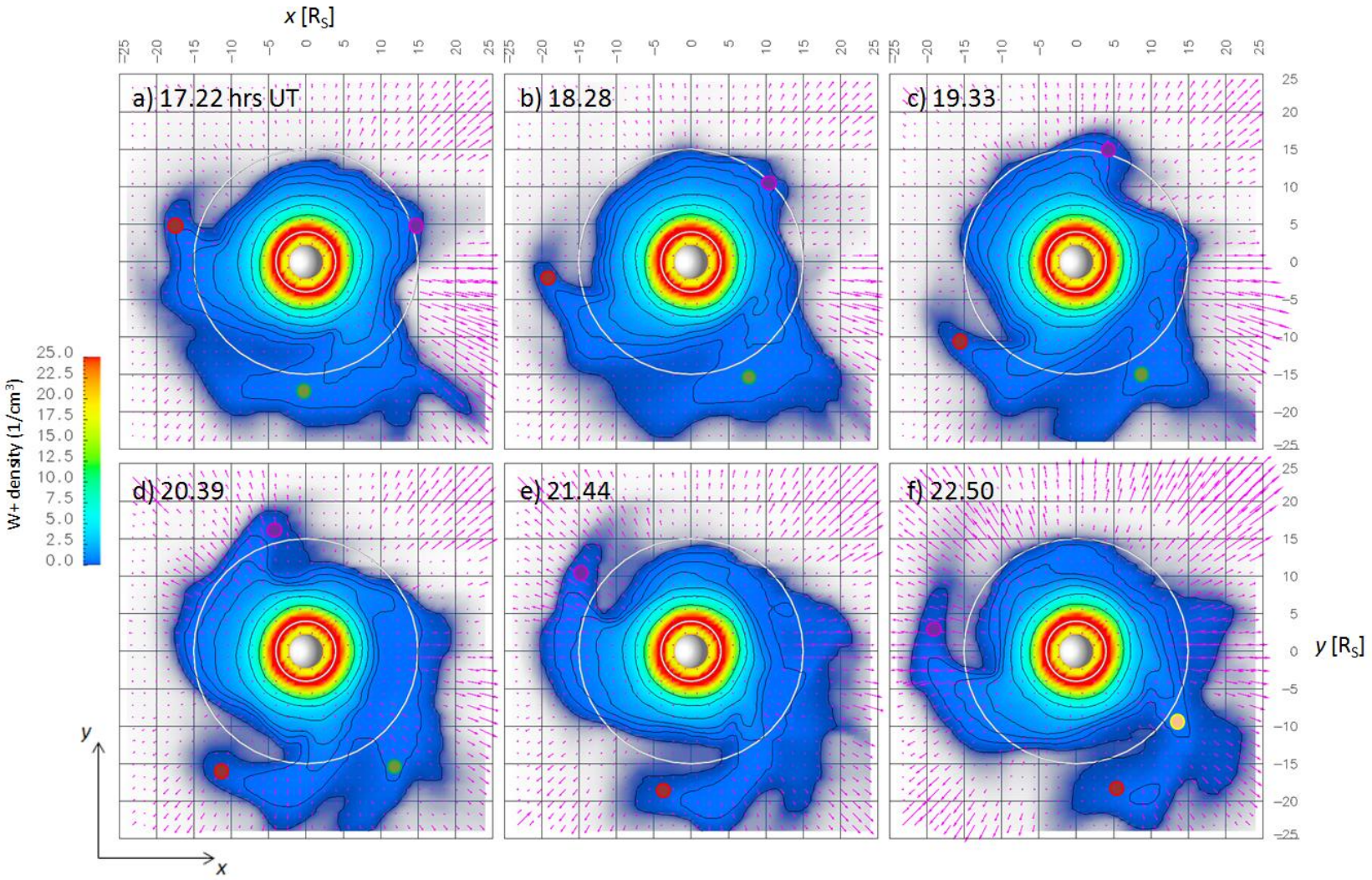

Figure 5.3 Equatorial time series (z = 0, looking down on Saturn's north pole) displaying W+ density contours for 1.1 Saturn rotations, a) 0 T_S , b) 0.1 T_S , c) 0.2 T_S , d) 0.3 T_S, e) 0.4 T_S , f) 0.5 T_S

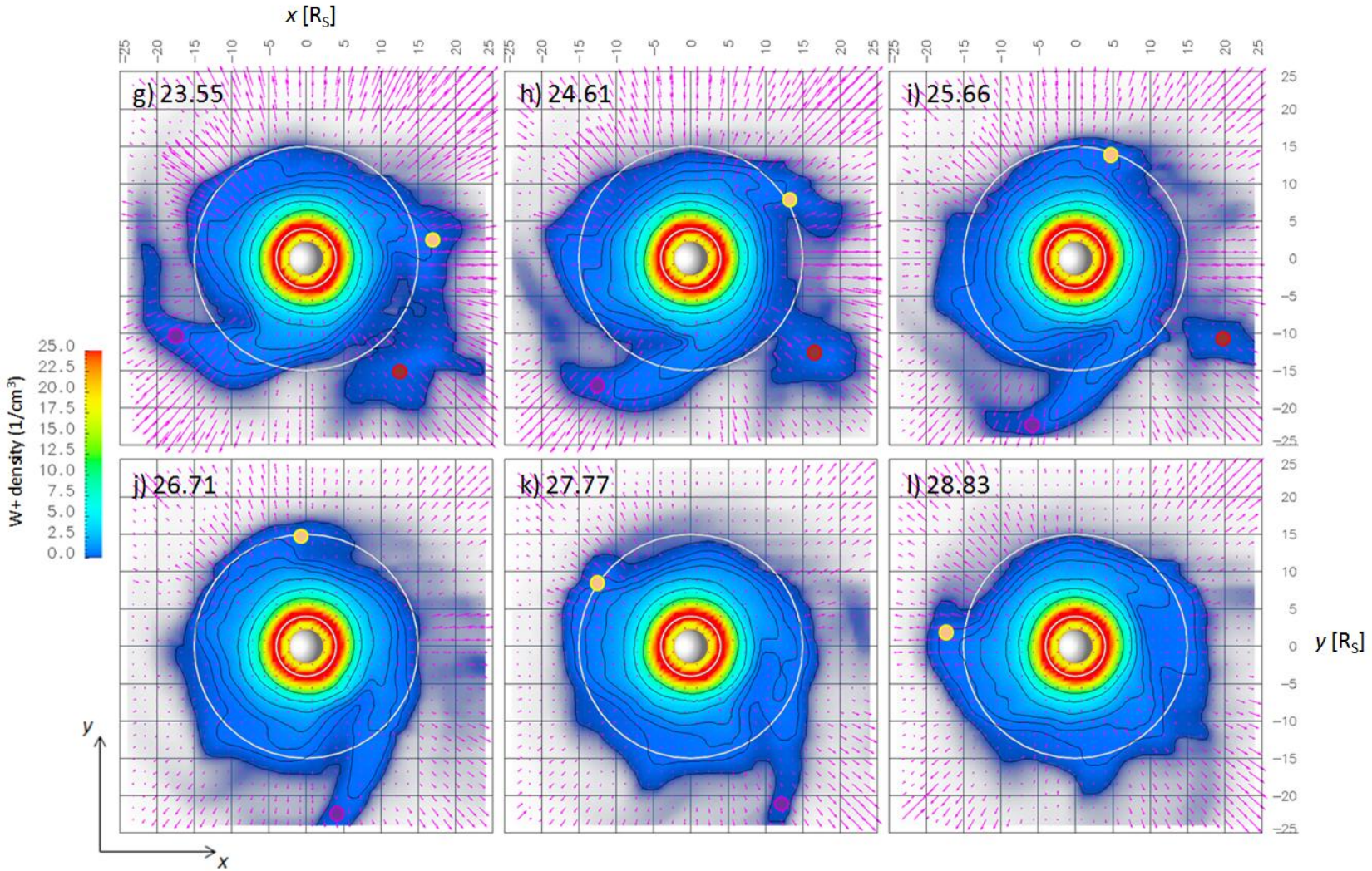

Figure 5.3 (continued) g) 0.6 T_S , h) 0.7 T_S , i) 0.8 T_S , j) 0.9 T_S , k) 1.0 T_S , l) 1.1 T_S

flow area at 21:00 hrs SLT (Figure 5.3e-h), its plasma does not simply stream away, but instead detaches from the main inner-magnetosphere structure in a well-defined "bubble", shown distinctly in Figure 5.3i, which the local velocity field then advects in both the corotation and tailward directions, thus presenting an alternate route by which inner-magnetosphere plasma may be lost. Region 3 exhibits yet another interesting behavior: while in the process of shedding the bubble of plasma, the swept-back portion of the outflow structure inside of $r \approx 16$ R_S persists. This then forms the nucleus of a new outflow structure, Region 4 (yellow), which then begins growing at 0.5 T_S, before the bubble detaches from the main structure. For further clarity, please refer to Figure A1.2 in Appendix A1 for a combined animation of the equatorial W+ density and electron temperature contours over this timer interval, showing how outflow structures evolve alongside injection fingers.

Having described in detail the evolution of radial outflow regions and how mass is shed from the inner magnetosphere, we now examine the mean and time-varying rates of radial W+ ion flux normal to Saturn's spin and dipole axes, $\dot{n}_r$, shown in Figure 5.4a for the same interval over which we examined the rate of W+ production. $\dot{n}_r$ is derived from the multifluid output by calculating the flux of ions through the surface of a cylinder of radius $r = 15$ R_S with an axis aligned with the rotational and dipole axes and symmetric across the equatorial plane ($-4.5 < z < 4.5$ R_S):

$$\dot{n}_r = \int_{-h/2}^{h/2} \int_0^{2\pi} n v_r \, r d\varphi dz \tag{14}$$

The use of a cylinder height of 9 R_S allows us to compensate for both the finite thickness and the curvature of the plasma sheet. We restrict our discussion to flows in the *x-y* plane,

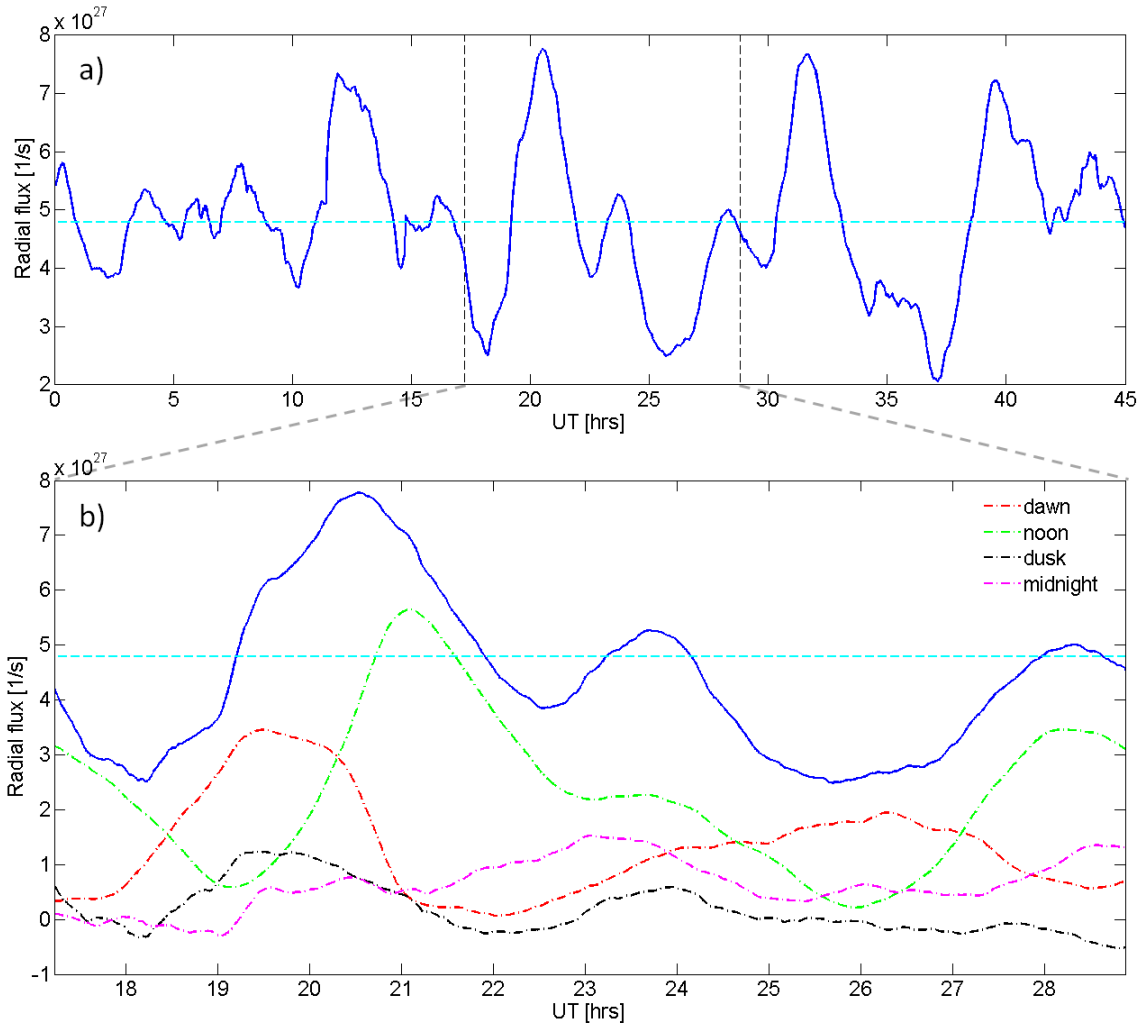

Figure 5.4 Radial number flux at r = 15 R_S, over a) 4.25 T_S, and b) 1.1 T_S (same time interval as Figure 5.3)

since out-of-plane velocities are significantly lower than in-plane velocities in the inner- and middle-magnetosphere region.

The mean outward radial flux at 15 R_S is 4.79 × 10^{27}/s over the given 45-hour time interval (136 kg/s), which is approximately within a factor of two of the 280 kg/s value obtained by *Chen et al.* [2010] from CAPS measurements. Compared to the rate of

W+ production, the variability of radial flux is much greater, with a maximum deviation from the mean of about 63%. This is consistent with the time sequence in Figure 5.3, which demonstrates the dynamic nature of the evolution of the outflow structures. Figure 5.4b shows a subset of the total radial flux data corresponding to the Figure 5.3 time sequence. The dashed lines represent the radial fluxes for individual Saturn Local Time sectors: dawn (03:00-09:00 SLT), noon (09:00-15:00 SLT), dusk (15:00-21:00 SLT), and midnight (21:00-03:00 SLT). Note the peak at dawn between 18-21 hrs UT. This represents the outflow of Region 1 in Figure 5.3 as it moves through the dawn sector. The leading edge of this region enters the noon sector between 19 and 20 hrs UT, and exits after approximately 24 hrs UT. It is clear that the highest rate of outflow in Region 1 occurs during its passage through the noon sector. This behavior is repeated by Region 4, which grows faster in the noon sector (26 hrs UT onwards) than it does in the dawn sector (24-27 hrs UT). Note that the rates of radial flow at $r = 15\ R_S$ are substantially lower at dusk and midnight, with some inward flow apparent at dusk. This is consistent with our earlier results showing that most of the plasma in an outflow structure outside of $r = 15\ R_S$ escapes in the vicinity of 21:00 SLT.

Since the total radial flux is the sum of the fluxes from each sector, we may infer that each peak in the total flux signal represents the development of a large outflow structure. A Fast Fourier Transform (FFT) analysis of the total radial flux signal from Figure 5.4a reveals two strong frequencies, at 2.89×10^{-5} Hz ($1.11/T_S$) and at 6.89×10^{-5} Hz ($2.63/T_S$), as shown in Figure 5.5. We do not suggest that these frequencies are somehow related to the SKR frequencies that govern many periodic phenomena in Saturn's magnetosphere, nor do we suggest that there are fundamental physics driving the

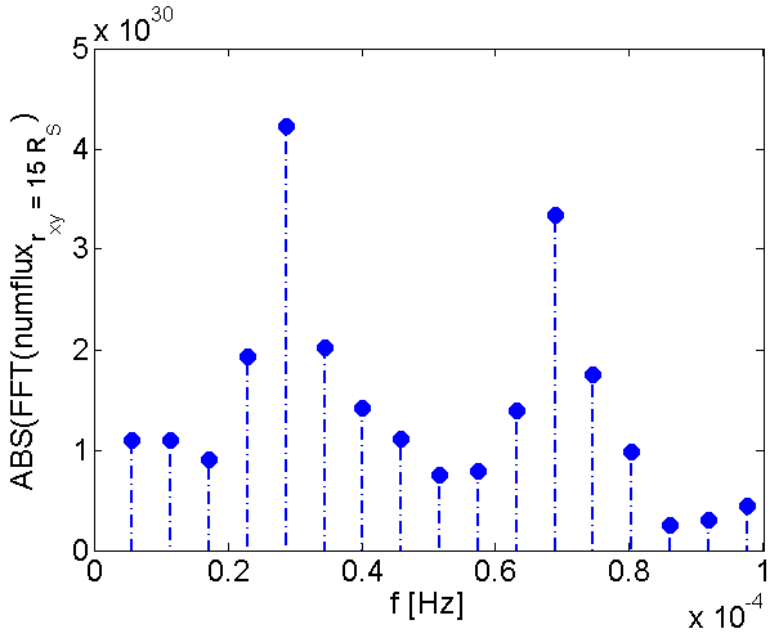

Figure 5.5 Absolute value of Fourier coefficients in frequency space from FFT analysis of signal in Figure 5.4a

evolution of outflow structures on these timescales. In the absence of longer intervals of data, we simply use them as a way to quantify the production of outflow regions. Thus, depending on the phase relationship between the two frequencies, our results show that outflow structures develop and shed mass at the approximate rate of $3.5/T_S$. However, there is considerable variability in this rate, which we infer both from the spread of frequencies in the FFT analysis and by inspection of Figure 5.4a.

We previously calculated an average combined rate of W+ production rate due to both electron-impact ionization and photoionization of the neutral cloud of 3.02×10^{27}/s (85.9 kg/s). This is too low to account for the mean radial number flux of 4.79×10^{27}/s (136.2 kg/s), which in turn implies an ionospheric source rate of 1.77×10^{27}/s (50.3 kg/s). Combined with the mean mass of the plasma sheet, this allows us to calculate a

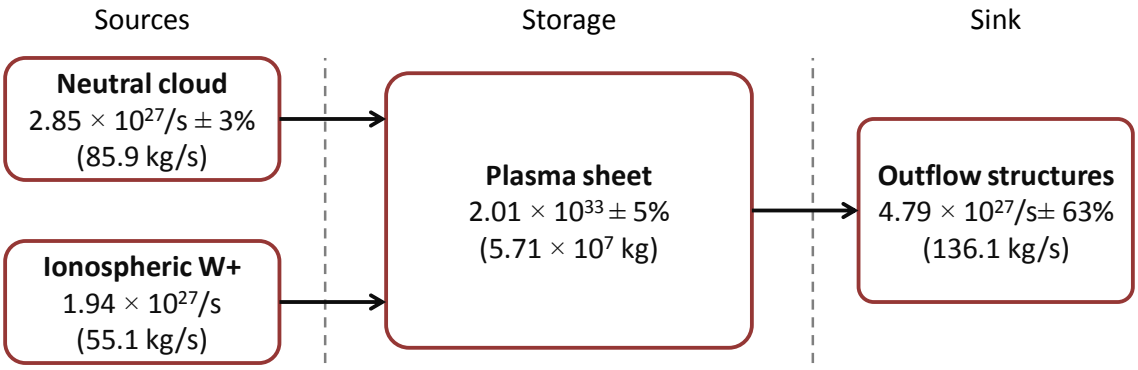

Figure 5.6 Conceptual model of plasma production and transport in Saturn's inner and middle magnetosphere

characteristic residence time of W+ plasma in the inner magnetosphere plasma sheet. Integration over a cylindrical region extending -4.5 R_S < *z* < 4.5 R_S in height and with radial extent 5 R_S < *r* < 15 R_S gives an mean plasma sheet W+ ion content of 2.01 × 10^{33} (5.71 × 10^7 kg). Incidentally, integration over the radial distance used by *Chen et al.* [2010] gives a mass of 2.7 × 10^7 kg, once again approximately half their calculated value. Figure 5.6 thus shows the resulting conceptual model of inner-magnetosphere plasma transport: mass enters the inner-magnetosphere plasma sheet from both the ionospheric source as well as through self-consistent ionization of the neutral cloud, flows through the plasma sheet, and is eventually lose through outflow structures. Assuming steady input and output at the mean values, the characteristic transport time over this interval would therefore be 116 hrs, or approximately 11 T_S.

Having described in detail both the qualitative and quantitative aspects of the outward transport of inner magnetosphere plasma, we now discuss our simulation results on the injection of hot plasma into the inner magnetosphere (described in section 1).

Figure 12 shows equatorial electron temperature contours and radial flow vectors at 23.93 hrs UT. Injections of hot plasma (T_e > 30 eV) penetrating the inner magnetosphere are clearly visible between regions of strong outward radial flow which correspond to the outflow structures identified in Figure 5.3. This hot plasma mostly originates in the region between midnight and dawn, outside of r = 15 R_S, and may be heated by reconnection events in this region. As these hotter regions move azimuthally around the planet, they also move radially inwards, driven by the $\boldsymbol{E} \times \boldsymbol{B}$ drift. The maximum penetration of the injections in our results is relatively shallow, with the fingers' radial motion stopping at $r \approx 10$ R_S, compared to *in situ* data which shows injections reaching between 5 R_S < r < 10 R_S [*Burch et al.*, 2005; *Hill et al.*, 2005; *Mauk et al.*, 2005; *Chen et al.*, 2010]. Moreover, the simulation also produces fewer fingers, with greater radial extent. Some of these issues may be because the maximum grid resolution in the inner and middle magnetosphere ranges between 0.25 and 0.5 R_S, which likely restricts the minimum size of a developing injection. Please refer to Figure A1.2 in Appendix A1for a combined animation of equatorial W+ density contours and electron temperature over the above time interval.

To verify that the characteristics of the simulated injection fingers are similar to those observed by Cassini, we take a trajectory through one of the fingers in Figure 5.7, denoted by the arrow at r = 12.5 R_S. This trajectory begins at 12:00 hrs SLT and terminates at 14:45 SLT, for a total arc length of 18 R_S. The synthetic spectrograms from this trajectory for all ions, protons , and W+ ions are shown in Figures 5.8a- c while Figures 5.8d and e show the variation in magnetic pressure and radial plasma velocity. The dashed vertical lines denote the boundaries of the injection finger that intersects with

this arc (~12:45-14:30 SLT, determined by inspection). When compared to the CAPS data presented by *Burch et al.* [2005], Figure 5.8a exhibits similar qualitative trends, showing the presence of two distinct ion populations outside of the injection region. The lower energy component of both populations drops out inside the injection, leaving only hotter, low-density plasma sourced from the middle and outer magnetosphere. The individual spectra of the major ion constituents show that the lower-energy species is, as expected, the protons, with the higher energy species being the water group ions. Figure 13d shows that the magnetic pressure within the injection finger is somewhat depressed

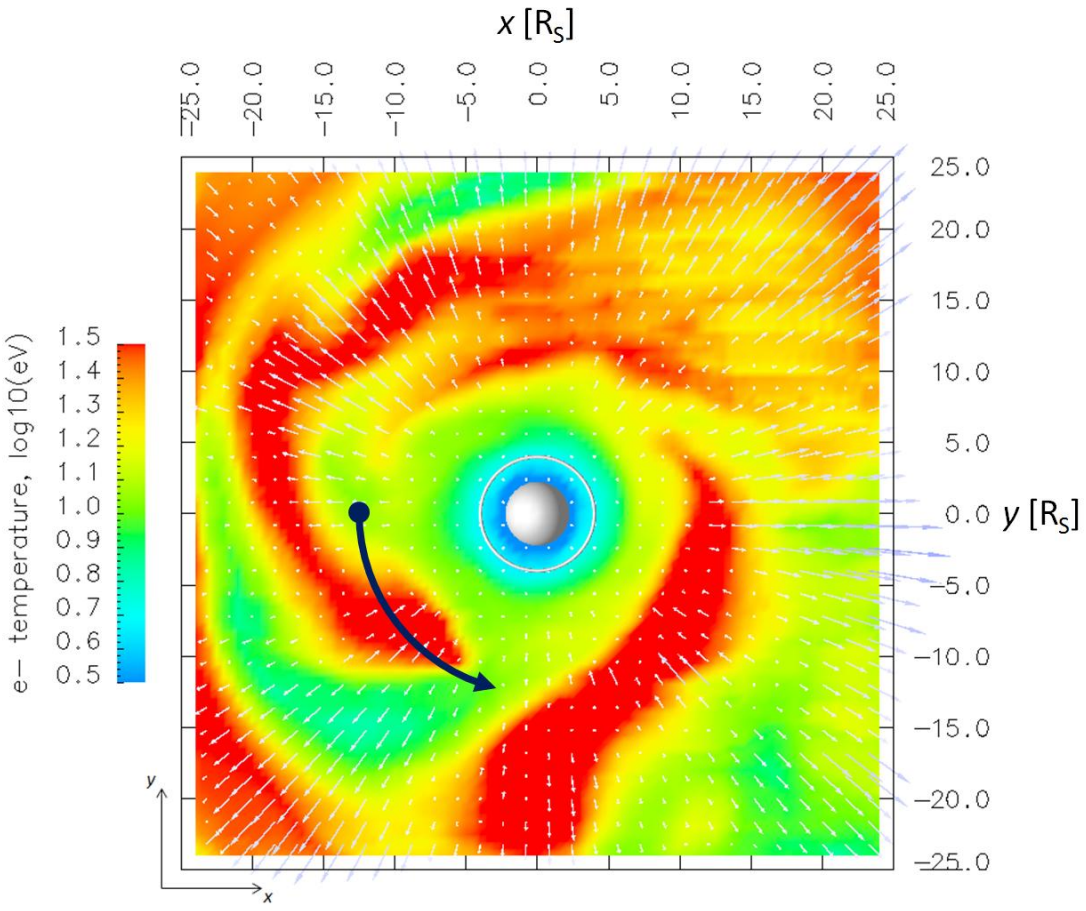

Figure 5.7 Equatorial electron temperature contours at 23.93 hrs UT (0.63 T_S)

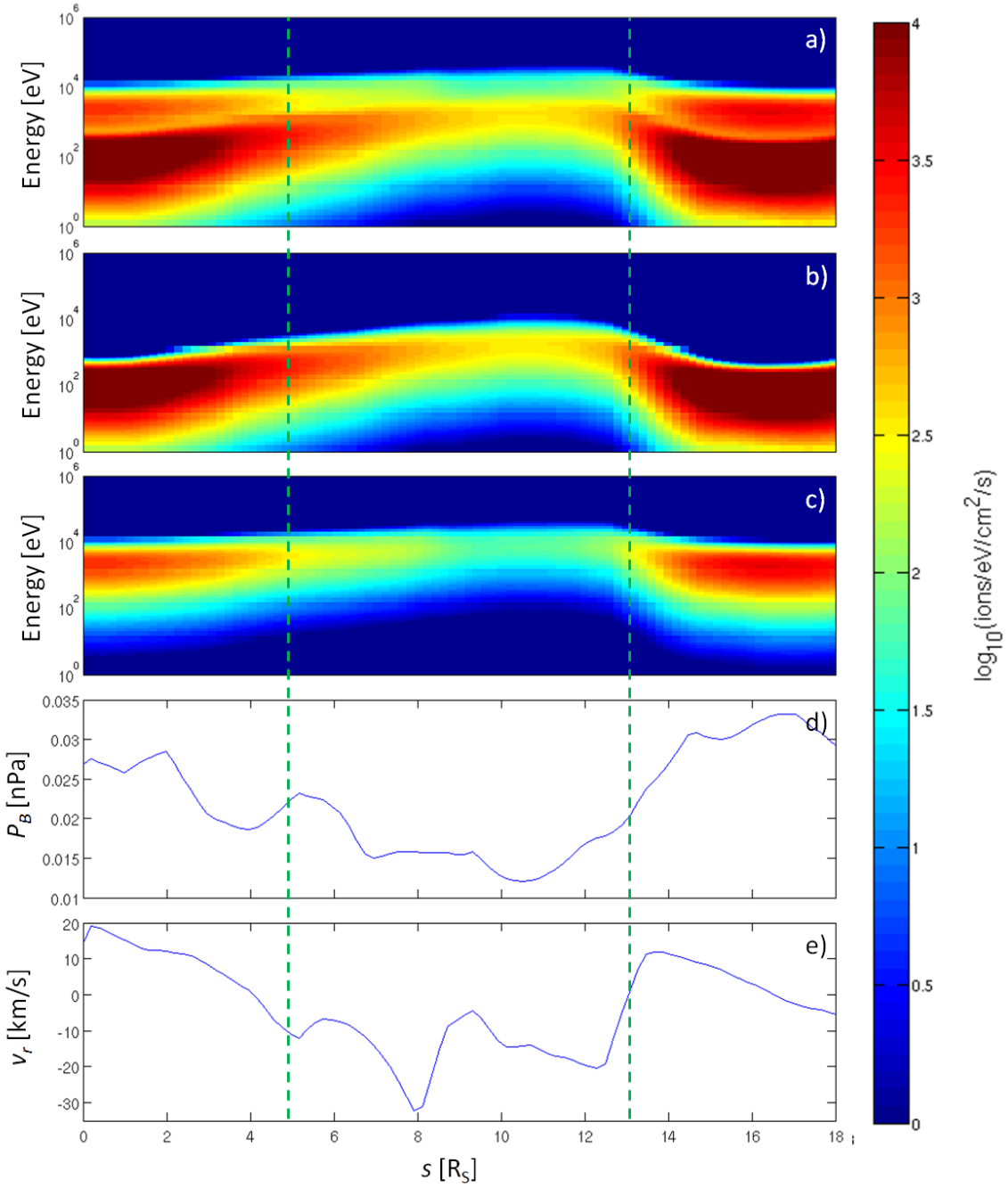

Figure 5.8 Synthetic spacecraft data across injection finger shown in Figure 5.7, synthetic spectra for a) total plasma, b) protons, and c) W+ ions, d) magnetic pressure and e) radial velocity profiles across injection finger

inside the injection region, in agreement with previous studies that have identified reduced magnetic pressures or total field strengths in flux tubes with hotter, lower-density

plasma that are involved with the interchange process [*André et al.*, 2005; *Leisner et al.*, 2005; *André et al.*, 2007]. Finally, Figure 5.8e shows that radial flow inside and outside the injection region is predominantly inwards and outwards respectively, in accordance with our assertion that this structure is similar to injection fingers that have been observed *in situ*. Note that quantitatively, while the spectra and magnetic pressures in Figure 5.8 are somewhat different from the CAPS and MAG results referred to above, they are fully consistent with the fact that our measurements are at a significantly greater radial distance (r = 12.5 R_S vs. 5 < r < 10 R_S for the available *in situ* data).

5.3 Summary of findings

Our results show that the overall rate of water group plasma production is relatively steady in both time and space, with a mean rate of 86 kg/s, 92% of which is due to electron-impact ionization. Moreover, without considering more exotic electron energy distributions with heavier tails (e.g.: the Kappa distribution) , we find that a small hot population accounts for very little ionization, and that the vast majority of new W+ ions are produced by the thermal electron population inside a radial distance of 6 R¬S. Conversely, the radial flux rate is much more variable, depending on the development, growth, and destruction of outflow regions which transport inner-magnetosphere plasma radially outwards. The mean radial flux rate at 15 RS is 136 kg/s and displays variability exceeding 60%. The imbalance between the radial outflow and the mass produced from the neutral cloud is accounted for by an ionospheric source of W+ which is included to ensure that the model's computational performance is acceptable. The simulation also shows that the growth of outflow structures and how they shed mass is a complex and dynamic process. Outflow structures typically develop over the course of a single

rotation, and shed plasma when passing through 21:00 hrs SLT. The shed plasma typically flows radially away and down the tail, but may also flow azimuthally as well, depending on the time-varying local flow-field. The remnants of outflow structures from previous rotations can act as the nucleus of new structures. Most of the growth and inflation of these structures takes place as they sweep through the dawn and noon sectors.

CHAPTER 6

IMPACT OF SEASONAL VARIABILITY ON SATURN'S MAGNETOSPHERE

In the previous chapter, we examined the production and radial transport of mass, processes with characteristic timescales on the order of the planet's rotation period (~10.6 hrs) or less. We also introduced a second timescale, that of the radial transport of inner magnetosphere plasma (~100 hrs). A single Saturnian year lasts approximately 29.5 years, with an aphelion of 10.1 AU, and a perihelion of 9 AU. Saturn's significant axial tilt (approx. 26°) combines with the close alignment of its magnetic dipole and rotational axes to produce marked seasonal variability over the course of an orbital period. This is most apparent in the change in curvature of the current sheet as the planet moves from equinox to solstice and back: the angle of attack (AOA - the effective angle between the dipole axis and the oncoming solar wind flow) varies from 0° at equinox, resulting in little to no curvature, to 26° at Northern and Southern solstice, when the magnetosphere is deformed into a "bowl" or "basin" shape [*Arridge et al.*, 2008; *Sergis et al.*, 2011]. In this chapter, we use the Saturn multifluid MHD to investigate the changes in magnetospheric morphology and dynamics that result from seasonal variation, expressed as a function of AOA. Model output is used to study the relationship of plasma sheet curvature with the solar wind AOA as a function of local time, as well as the implications of changes in plasma sheet curvature for production and transport of plasma in the inner and middle magnetosphere.

6.1 Mean plasma sheet curvature

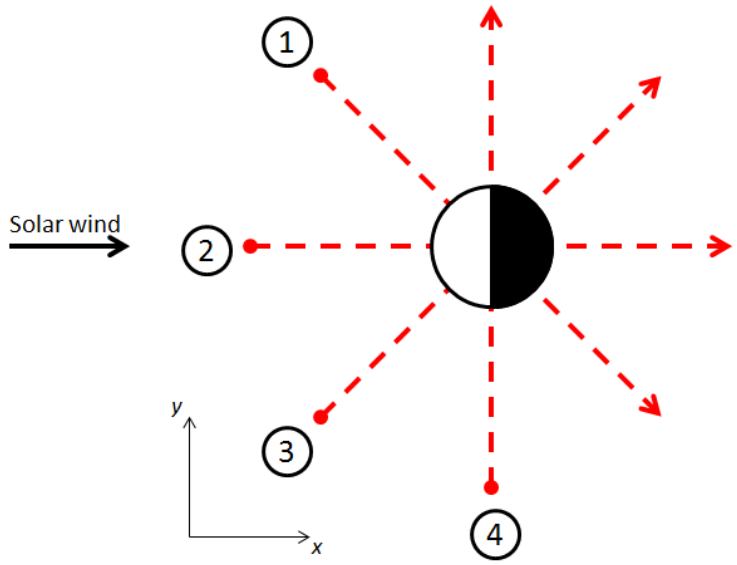

Figure 6.1 Schematic showing four meridional planes (red dashed arrows) along which plasma sheet position is calculated. Filled red circle represents starting point of each profile, arrowhead represents end. (1) pre-noon → pre-midnight, (2) noon → midnight, (3) pre-dusk → pre-dawn, (4) dusk → dawn.

The bowl morphology of Saturn's magnetosphere is well-established, and major modeling efforts have been successful in reproducing the curved plasma sheet [*Hansen et al.*, 2005; *Kidder et al.*, 2009]. We likewise demonstrated in Chapter 5 that the Saturn multifluid model, when modified with the inclusion of self-consistent plasma-neutral interactions, was likewise able to demonstrate the curved plasma sheet, as visualized in the dawn-dusk meridian (see Figure 4.1a). We now investigate the curvature of Saturn's plasma sheet as a function of both season (i.e.: AOA) and local time, using four radially symmetric planes as shown in Figure 6.1. Each plane is coincident with a specific meridian (i.e.: passes through Saturn's rotational axis) and is aligned with the following

local times: (1) pre-noon → pre-midnight [09:00 → 21:00 hrs SLT], (2) noon → midnight [12:00 → 24:00 SLT], (3) pre-dusk → pre-dawn [15:00 → 03:00 SLT], and (4) dawn → dusk [18:00 → 06:00 SLT]. We obtain the profile of the plasma sheet in a given plane by designating the largest value of $n_{W+}(z)$ for every radial point r_n along the length of the plane as the center of the sheet for -25 R_S < r < 25 R_S.

Figure 6.2 shows the resultant plasma sheet profiles for the magnetosphere at solstice (a, AOA = 26°), at AOA = 15° (b), and at equinox (c, AOA = 0°). The red solid lines show the mean position of the plasma sheet from a time interval of ~45 hrs the multifluid simulation output, while the blue solid lines show the mean position ± 2σ, and are thus represent the envelope within which 95% of all plasma sheet locations in z may be found. The dashed red lines represent an analytic solution for the shape of the magnetodisc from *Arridge et al.* [2008], reproduced below:

$$z_{PS} = \left[r - R_H \tanh\left(\frac{r}{R_H}\right)\right] \tan\theta_{sun} \quad (15)$$

z_{PS} is the current sheet location in z, r is the radial distance from the rotation axis in the equatorial plane, θ_{sun} is the angle of attack, and R_H is the hinging distance, a characteristic distance which determines at which radius the curvature becomes significant. Using Cassini MAG data from a series of trajectories reaching deep into the inner and middle magnetosphere (June 2004 - April 2006; 25° > θ_{sun} > 20°), *Arridge et al.* [2008] found that a value of R_H = 29 R_S gave the best prediction efficiency (percentage of correct identifications) for Equation 6.1, while *Arridge et al.* [2011a] found that 16 R_S < R_H < 32 R_S. Note that the value from *Arridge et al.* [2008] is intended to encompass data over a range of AOA values and local times, while the range includes local time dependence and is used to analyze periodic motion of the plasma sheet, a topic

Table 3 Hinging distances for each half of the four meridional plasma sheet profiles (see Figure 6.1)

Profile	$R_H(r < 0)$ [R_S]	$R_H(r > 0)$ [R_S]
(1) pre-noon → pre-midnight	15	45
(2) noon → midnight	19	[-]30
(3) pre-dusk → pre-dawn	22	20
(4) dusk → dawn	45	15

which is beyond the scope of this investigation (see section 2.4). Note also that there exists a broad range of R_H values for which prediction efficiency is greater than 90%. We have thus chosen an R_H value for each half of each meridional profile in Figure 6.2 (i.e.: for $r < 0$ and $r > 0$), selected by inspection based on how closely it matched the model results for mean plasma sheet at solstice, shown in Table 3. We use the *Arridge et al.* [2008] analytic formulation for three primary reasons: 1) to quantify the dependence of hinging distance and therefore the degree of curvature of the plasma sheet with local time, 2) to provide a comparison between simulation data and observations within a range of R_H values with high prediction efficiencies for *in situ* data, and 3) to enable comparison of model results for different seasonal conditions. We note that the R_H values selected by inspection in Table 6.1 all have prediction efficiencies > 90%.

Figure 6.2a shows that the plasma sheet curvature, or "bowl" morphology is very pronounced at most local times, with the greatest curvature (smallest radius of curvature) most pronounced on the dayside (06:00-18:00 hrs SLT). This is likely due to the direct effect of the solar wind exerting a northward stress on the southern bow-side magnetopause at this angle of attack. Note, however, that the mean plasma sheet profile at midnight exhibits a noticeable negative (southwards) curve. In this case, we have mirrored the analytic profile from Equation 6.1 in the *x-y* plane in order to approximate

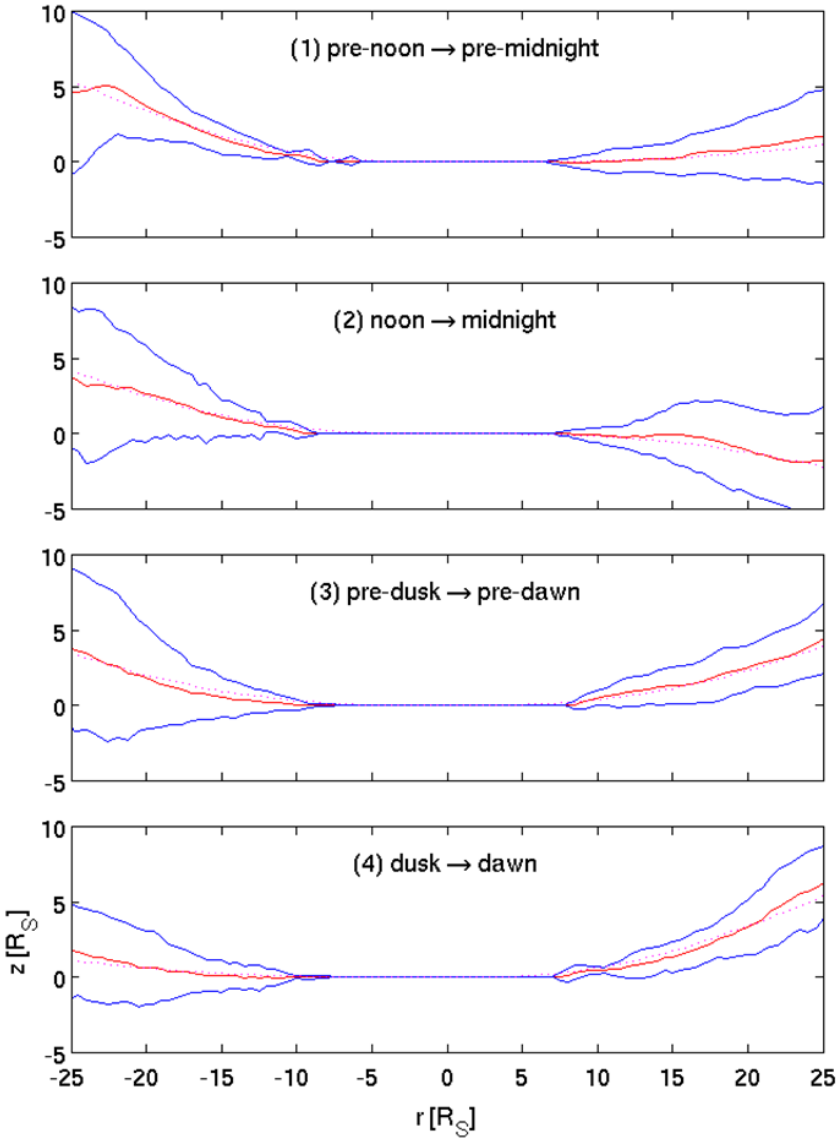

Figure 6.2 a) Plasma sheet curvature at southern hemisphere solstice (AOA = 26°). Red and blue lines represent simulation output mean position and 2σ envelope respectively, red dashed lines represent analytic solution from *Arridge et al.* [2008].

the model output. This southward mean curvature is unusual compared to the overall northward curving morphology, but it is important to note the plasma sheet is a dynamic structure, and has been observed to exhibit behavior such as "flapping" (northward and southward periodic motion [*Arridge et al.*, 2011a]) which results in excursions of the

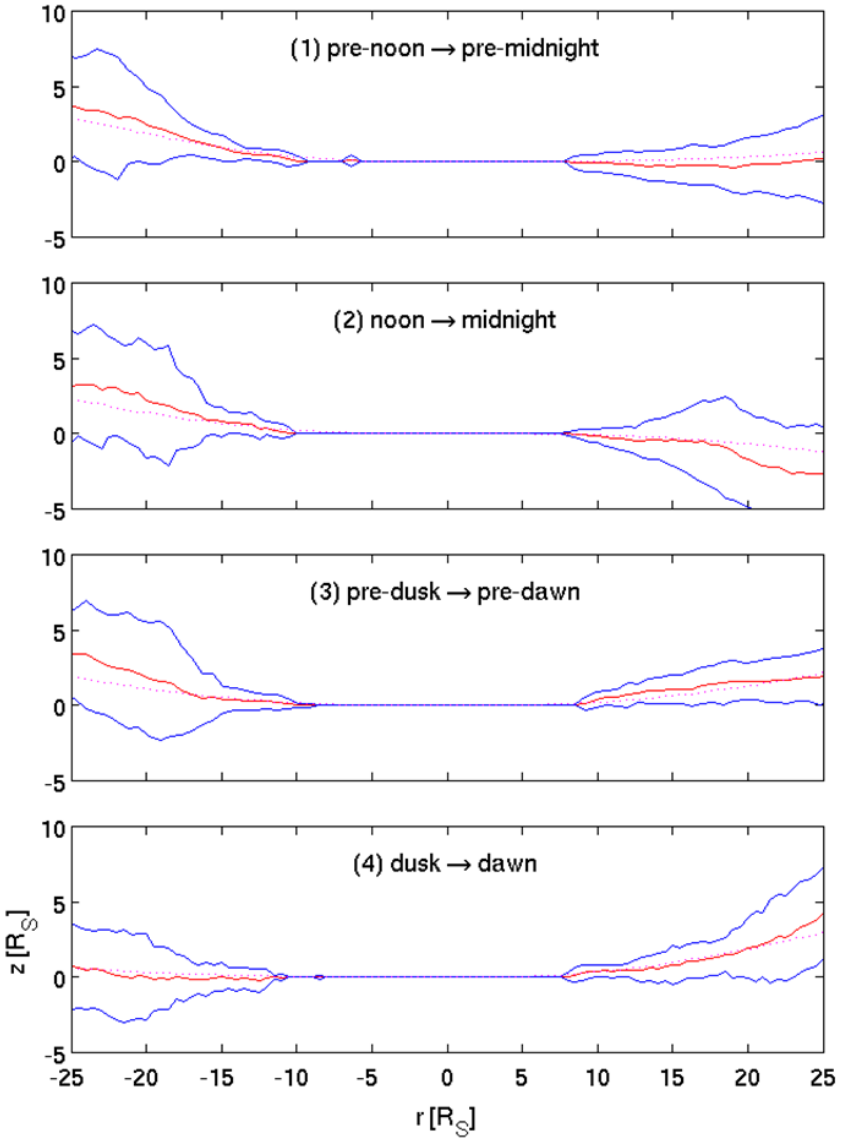

Figure 6.2 (continued) b) Plasma sheet curvature at AOA = 15°

plasma sheet south of the rotational equator. We will resume our discussion of the southward curvature at midnight in section 6.2, when we describe the dynamics of the plasma sheet. Inspection of the 2σ envelopes at each local time shown in Figure 6.2a reveals that the greatest variability in plasma sheet location is on the dayside, specifically between 09:00 and 15:00 hrs SLT. This may be due to the motion of the bow-side

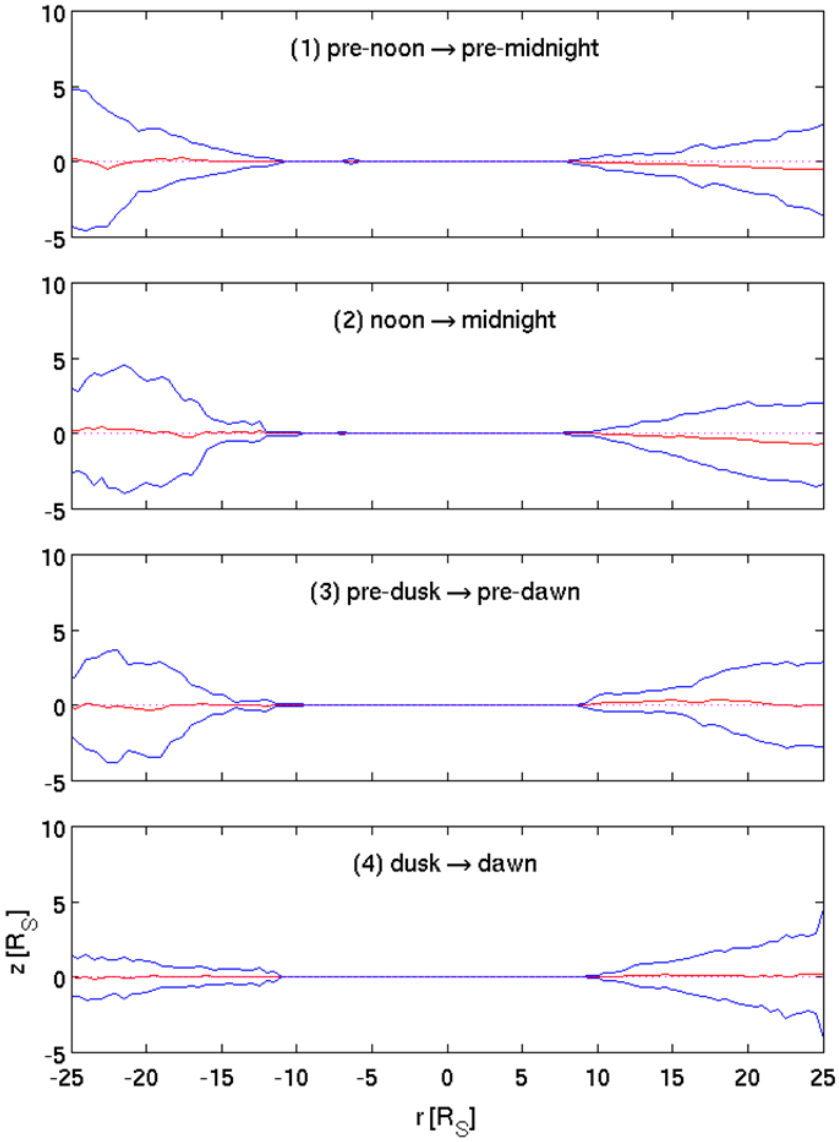

Figure 6.2 (continued) c) Plasma sheet curvature at equinox (AOA = 0°)

magnetopause, when the inward and outward moving boundary causes the curvature of the plasma sheet behind it to intensify or abate. We direct the reader to Figure A2.1 in Appendix A2 with an animation of the magnetosphere in the *x*-*z* plane showing how the moving magnetopause affects the plasma sheet curvature. Interestingly, there is also

substantial variability in the midnight plasma sheet, with extreme positions ranging from slight positive curvature to extreme negative curvature.

The range of motion at midnight is significantly larger than at the local time profiles on either side (21:00 and 03:00 hrs SLT).

The effect of reducing AOA from solstice to equinox values (26° to 0°) is visible in Figures 6.2b and c. While Figure 6.2 is based on ~45 hours of data for all AOA values, we emphasize that the increased smoothness of the profiles at equinox and solstice is due to the increased frequency of model output (3× of the output at 15° AOA), and therefore a greater number of data files that were averaged to obtain the mean profiles. Taking that into account, we nevertheless see that Figure 6.2b (AOA = 15°) exhibits the reduced curvature at all local times, while the plasma sheet is largely flat at all local times in Figure 6.2c (equinox), consistent with observations that the curvature of the bowl morphology decreases as Saturn transitions from solstice to equinox. Both figures also show that the regions of greatest variability in plasma sheet location remain the same (dayside and at midnight), suggesting that the processes that cause increased plasma sheet motion at these local times remain present regardless of changing AOA. We also note that the analytic prediction for plasma sheet morphology falls well within the variability envelope for all local times at both equinox and 15° AOA, but it is also clear that solutions with numerous values for hinging distance would satisfy the model outputs, and hence that the hinging distances may change significantly during Saturn's orbit. Interestingly, the best match between the analytic solution and the model observations is found along the dusk-dawn meridian. In both cases, we also see that there is a southwards deflection of the plasma sheet at midnight.

6.2 Nightside plasma sheet dynamics

In the previous section we saw that, while the mean plasma sheet curvature decreases with AOA, the sheet moves through a wide range of motion at all seasons. We now investigate the instantaneous morphology of the plasma sheet and examine how it behaves over time for both southern solstice and equinox. We restrict ourselves to the nightside plasma sheet in box 2 of our simulation domain ($0 < x < 25$ R_S, $-25 < y < 25$ R_S, $-12.5 < z < 12.5$ R_S), since this magnetopause does not encroach in this region, and thus allows the plasma sheet to be easily defined as those points with the largest W+ densities. It is important to understand that simulations are invaluable to understanding the global motion of the plasma sheet: the nature of spacecraft data means that investigators are only able to examine events along a trajectory, and therefore cannot easily relate them to phenomena occurring in other regions of the magnetosphere, whereas our model results can provide instantaneous snapshots of how the plasma sheet structure evolves in time.

Figure 6.3 shows two such instantaneous snapshots at solstice and equinox, exhibiting the typical nightside plasma sheet morphologies during both seasons. The plasma sheet is bounded on the northern and southern edges by the purple surfaces, the red lines represent the magnetic field inside the magnetosphere, and the contours represent the proton pressure in the *x*-*y*, *x*-*z*, and *y*-*z* planes. The instantaneous plasma sheet is extremely flat inside of $r = 10$ R_S at both equinox and solstice, consistent with Figure 6.2 which shows that the mean sheet is essentially flat and exhibits very little variability inside of this distance. Outside of 10 R_S, the nightside plasma sheet displays a significantly rugose or "wrinkled" texture. Despite this texture, the average bowl

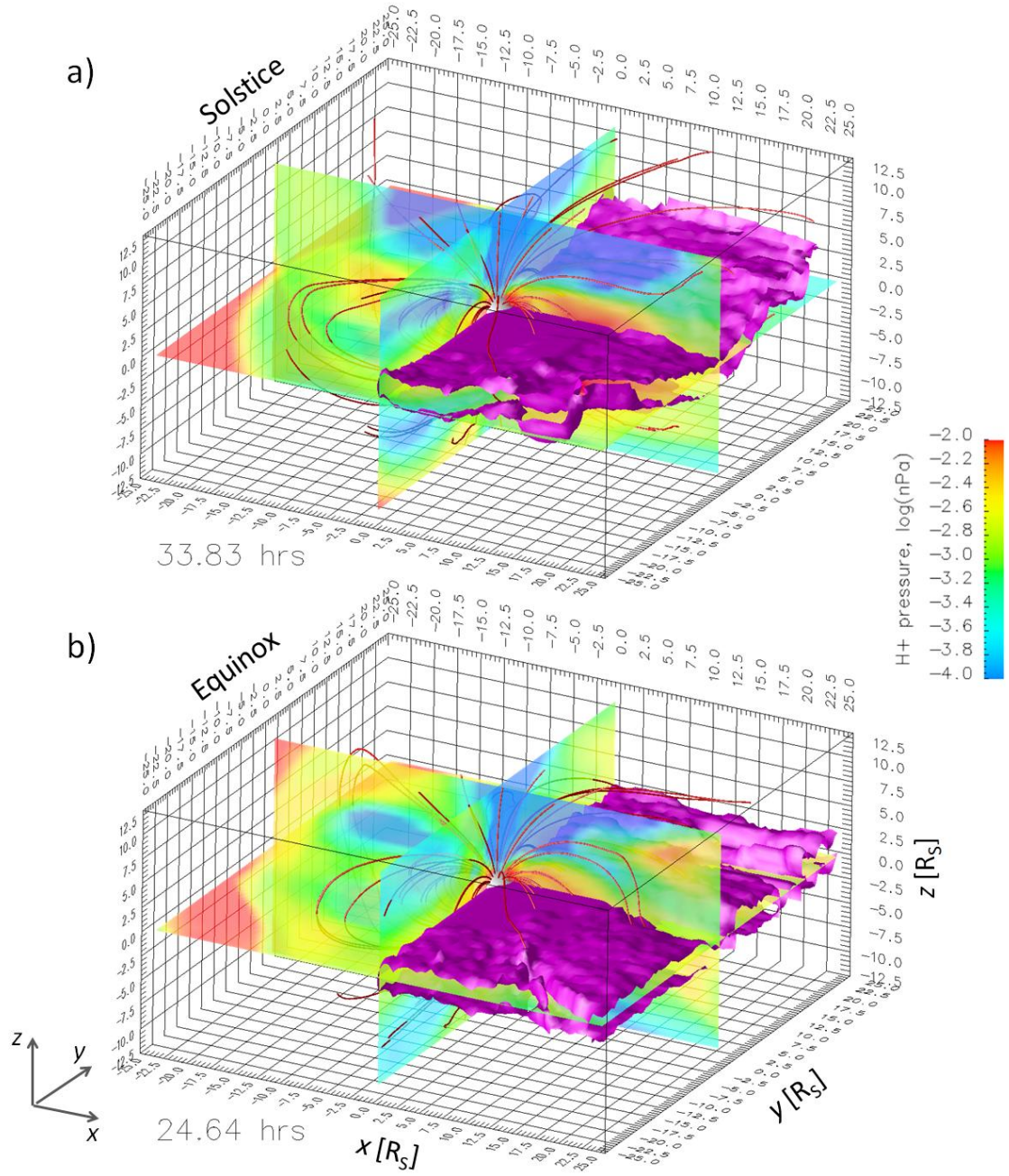

Figure 6.3 Proton pressure contours and instantaneous nightside plasma sheet morphology at a) solstice (UT = 33.83 hrs), and b) equinox (UT = 24.64 hrs)

morphology at solstice is readily discerned, while the equinox plasma sheet is clearly moving around a flat mean position.

While the instantaneous plasma sheet morphologies are in good agreement with the *in situ* data and mean simulation output, it is necessary to examine a time sequence in order to understand the motion of this structure. Therefore, we present Figures 6.4 and 6.5, showing equatorial (*x*-*y*) time sequences of the plasma sheet at solstice and equinox respectively. As before, the contours represent proton pressure (see Figure 6.3 for color bar) while the nightside plasma sheet is denoted by the purple surface. Each sequence is approximately 0.17 T_S in duration, approximately the same as the timescale for plasma sheet motion depicted in Figures 6.4 and 6.5. An advantage of examining the nightside plasma sheet in the equatorial plane is that when the plasma sheet dips below the equatorial plane ($z = 0$), it shows up as a "gap" in the structure, allowing for easy identification of vertical motion.

At 0 T_S (Figure 6.4a), the solstice plasma sheet maintains a morphology similar to Figure 6.3a (i.e.: flat inside of $r = 10$ R_S, northward curvature and rugose texture outside of this distance). There is a noticeable southward excursion of the sheet at approximately 19:00 hrs SLT and $r = 20$ R_S. This localized feature is typical of many northward and southward excursions that occur at all local time sectors, are greater in amplitude than the typical rugose texture of the plasma sheet, and which grow and dissipate on the timescale of a few hours. Moreover, these features also tend to move azimuthally around Saturn, in approximate corotation with the planet, accounting for the local lag (see section 4.2, Figure 4.4). Over the course of the next 1.42 hrs (Figure 6.4e, 0.13 T_S), this region of the plasma sheet moves northward and the large-deflection local motion ends. These features

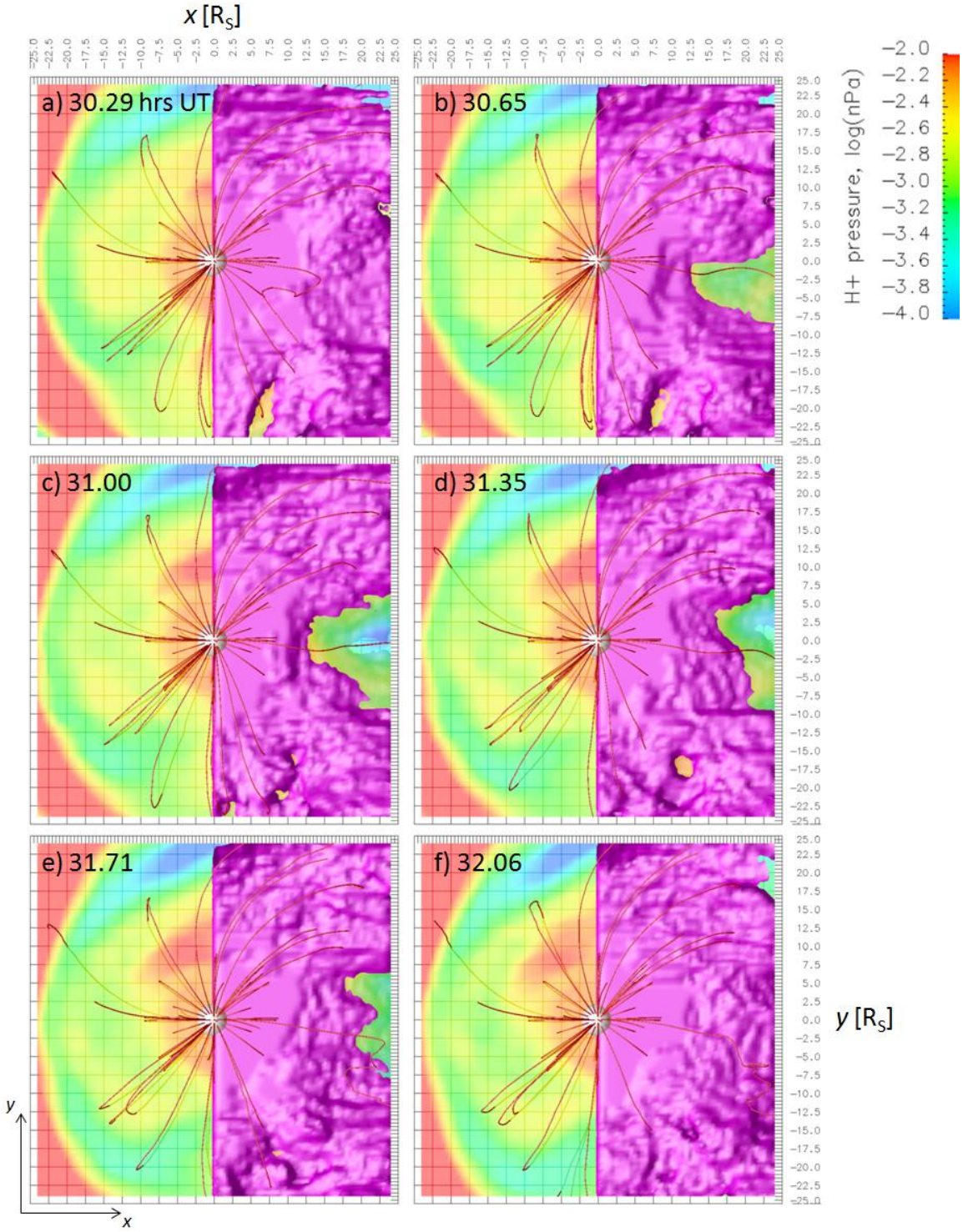

Figure 6.4 Equatorial time series of nightside plasma sheet motion at solstice over 0.18 Saturn rotations, a) 0 T_S , b) 0.033 T_S , c) 0.067 T_S , d) 0.1 T_S, e) 0.133 T_S , f) 0.167 T_S

are transient: they are formed and then move across the surface of the plasma sheet for a few hours before dissipating. They are thus likely due to fluctuations in the local magnetic field and plasma population. Any periodic perturbations would therefore be imposed on this motion (see section 2.4).

The formation and dissipation of a much larger and more localized southward excursion of the solstice plasma sheet is visible in the vicinity of midnight in Figure 6.4 (b-e). Unlike the previous case, this motion is strongly confined to 23:00-01:00 SLT and $r > 10\ R_S$, and involves a large-scale southward deflection of the plasma sheet below the $z = 0$ [equatorial] plane followed by a northward recovery, a motion that may be described as "flapping". The midnight plasma sheet dips below the equatorial plane at $0.033\ T_S$, reaching as far southward as $z = -2\ R_S$ (see Figure A2.2 in Appendix A2 for *y*-*z* plane view of solstice plasma sheet at $0.033\ T_S$), and remains there for just over $0.1\ T_S$ before recovering northwards. We note that this is roughly co-incident with a short period of increased plasma *x*-velocities in the vicinity. However, our examination of numerous southward excursions of the midnight plasma sheet has revealed no specific combination of local plasma or magnetic field conditions that correlate specifically with these events.

Figure 6.5 shows that the plasma sheet at equinox experiences largely similar behavior. The sheet exhibits the same rugose texture in the middle and outer magnetosphere, while there are larger southwards excursions at all local times on the nightside (e.g.: at 21:00 and 03:00 SLT in Figure 6.5). There is also a notably persistent southward deflection of the plasma sheet in the vicinity of midnight, which remains confined to this region and does not corotate the planet. Like the similar feature observed at solstice, this deflection of the plasma sheet in this region also reaches $z = -2\ R_S$ before

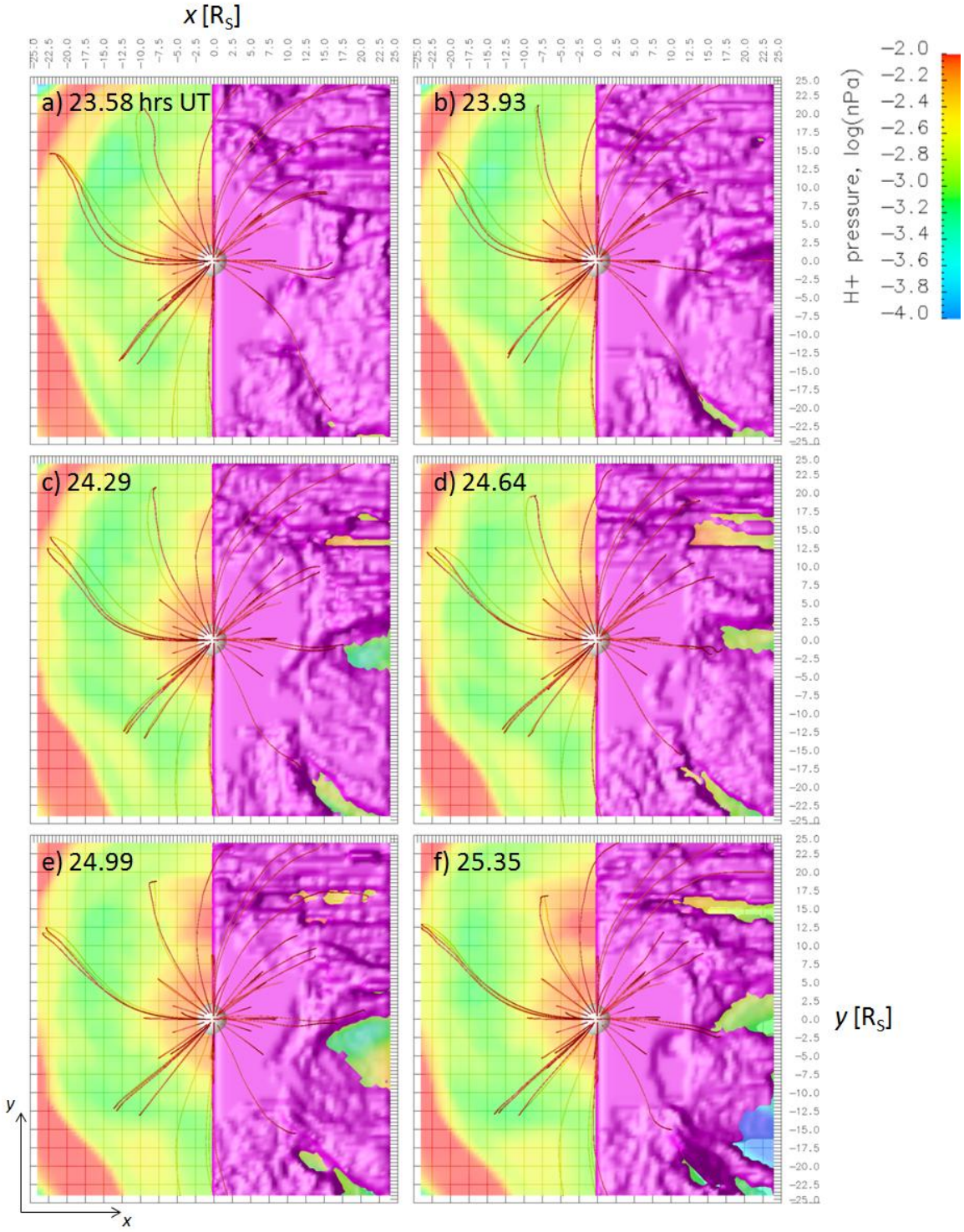

Figure 6.5 Equatorial time series of nightside plasma sheet motion at equinox over 0.18 Saturn rotations, a) 0 T_S , b) 0.033 T_S , c) 0.067 T_S , d) 0.1 T_S, e) 0.133 T_S , f) 0.167 T_S

moving northward again, similar to the "flapping" motion observed at solstice. The overall duration of this motion is generally a few hours, but it does not display obvious periodicities. Note that those southward excursions at solstice that cross the $z = 0$ plane would necessarily have to be larger than what would be required at equinox. However, an inspection of the nightside plasma sheet in the *y*-*z* plane reveals that both those deflections at midnight as well as those that are visible at other local times tend to be of the same size (see Figure A2.3 in Appendix A2 for *y*-*z* plane view of equinox plasma sheet at 0.133 T_S).

While the plasma sheet is always in motion for $r > 10$ R_S, the rugose texture in this region remains at both seasonal extremes, and is similarly absent inside this distance. Furthermore, it is clear that in qualitative terms, the dynamics of the plasma sheet at either seasonal extreme remain unchanged, except for the overall mean curvature that is present at solstice. Finally, the mean southward curvature of the plasma sheet at midnight discussed in section 6.1 appears to be the result of highly confined an intermittent "flapping" of the plasma sheet in this region, which results in mean deflection of the plasma sheet below the equatorial plane in the vicinity of this local time, thus disrupting the "bowl" morphology. However, southward excursions of the plasma sheet during southern solstice is a well-established observation, though these are due to the oscillation of the plasma sheet related to Saturn's periodicities [*Arridge et al.*, 2011a]. These midnight excursions are occasionally associated with accelerated tailward flows in the immediate vicinity, but are generally do not correlated with a specific magnetic configuration or plasma distribution. Note that "flapping" generated by Saturn's magnetospheric periodicities will be imposed on the plasma sheet motion that has been

described in this section, and thus may either mask or completely override the phenomena observed here.

6.3 Inner magnetosphere plasma production and transport

6.3.1 Global W+ production

The dynamics of the plasma sheet tell us how Saturn's magnetosphere responds globally to changes in season, since the curvature of the plasma sheet in turn determines the overall curvature of the magnetosphere. In this section use our model results to examine whether the overall curvature of the plasma sheet qualitatively or quantitatively affects the mass-loading and radial transport processes in the inner and middle magnetosphere. Figure 6.6 shows global W+ production in Saturn's magnetosphere at a range of different AOA values spanning equinox to southern solstice. The blue dots represent the mean global W+ production rates over at least 40 hours (~4 T_S) once the individual simulations have reached a quasi-equilibrium state (determined by inspection), the bars represent the 2σ envelope (i.e.: mean ± 2σ; 95% of all results fall within envelope), and the red line is the result of a least-squares regression through the mean values. The raw data (global W+ production vs. *t* line plots) are included in Appendix A2 for reference (Figure A2.4).

Figure 6.6 shows that there indeed appears to be a positive correlation between AOA and the global W+ production rate (correlation coefficient between AOA and production rate ~0.73). However, the least squares regression line suggests that the relationship is not particularly strong, with Saturn's orbital position only weakly influencing the mean rate of W+ production. We also observe that the range of variability between seasonal extremes is on the same order of magnitude as the variability in

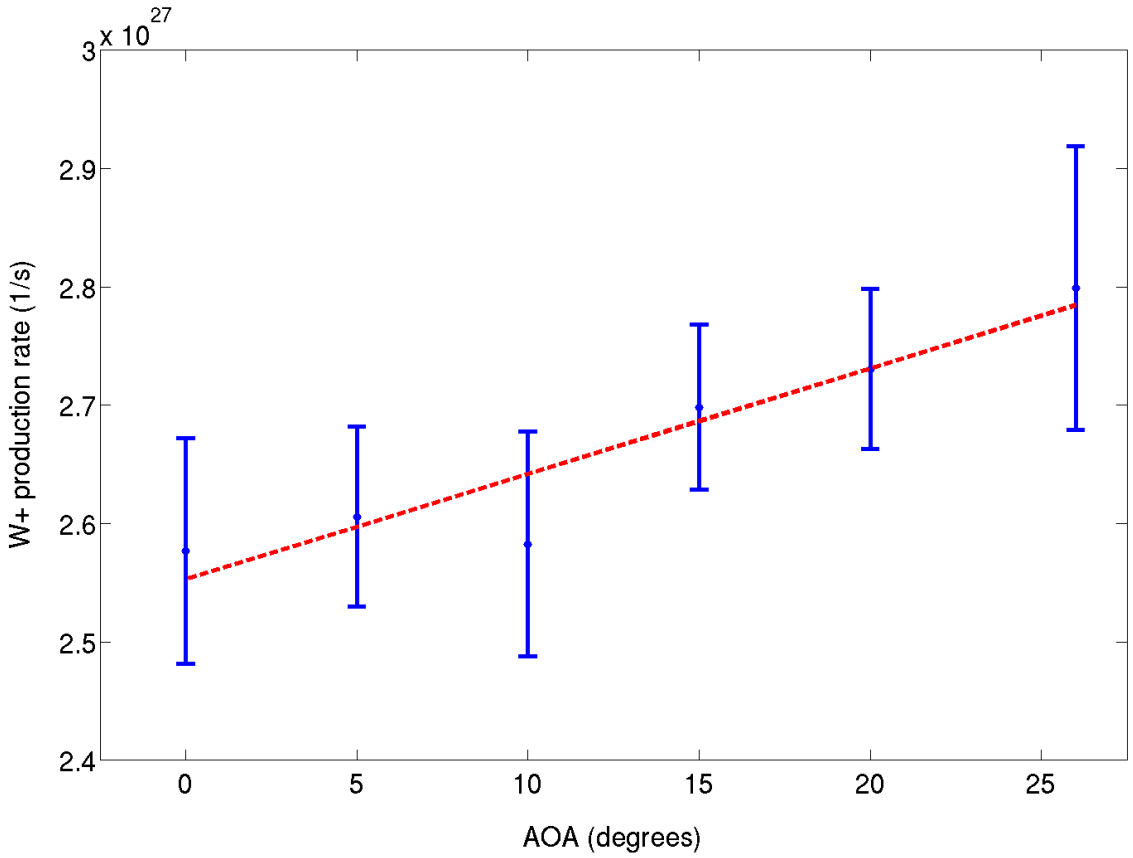

Figure 6.6 Global W+ production vs. AOA

production rate at a given AOA value. The overlap in ranges is such that it is not clear if the two quantities are related linearly or by some other function. Moreover, it is also important to remember that we have obtained these results by running with steady solar wind and IMF conditions for several tens of hours in order to reach equilibrium, which removes the effects of upstream perturbations on the magnetosphere. The *in situ* data show that the solar wind dynamic pressure and density at Saturn, as well as the IMF orientation, are constantly changing. These fluctuations, combined with the time delay required for these disturbances to travel into the inner magnetosphere and produce an effect, would therefore make it extremely difficult to determine if this trend holds from *in*

situ data. For confirmation, we ran the equinox case with antiparallel IMF for several rotations to see if this produced measurable changes in production rate. After running the simulation for a period of approximately 2.5 T_S after reversing the IMF, we found that the mean value of global production was 2.58×10^{27}/s, with a 2σ range 2.45×10^{27}/s < production < 2.70×10^{27}/s. While the mean value is very close to the corresponding case in Figure 6.6, the range of variability is larger, showing both that a change in external conditions does indeed produce fluctuations, and that rapid changes in upstream conditions would likely prevent the magnetosphere from settling to an equilibrium that would allow this trend to be discerned from the Cassini instrument data.

6.3.2 Water group plasma radial transport

Unlike the previous correlation between AOA and W+ production rate, there appears to be no such relationship between AOA and the radial flux at $r = 15\ R_S$, shown in Figure 6.7. As in the previous Figure, the blue dots and bars represent the mean and 2σ envelope of variability, while the red dashed line is a least squares fit to the mean value. The mean values at all AOA's are approximately similar, but the range of mean values is substantially larger than what we obtained for the global W+ production rate (4×10^{27}-5.5×10^{27}/s, or 114-156 kg/s; approx. 30%). We obtained a correlation coefficient of ~0.06, almost zero, confirming that there is no statistical relationship between these two quantities, which is also reflected by the insignificant slope of the linear regression line. The overall range of variability is large and comparable across AOA values, which is to be expected, as this is a function of the temporal and spatial variability of the initiation and evolution of outflow structures, which is in turn highly dependent on local plasma and magnetic field conditions. In summary, there appears to be no significant relationship

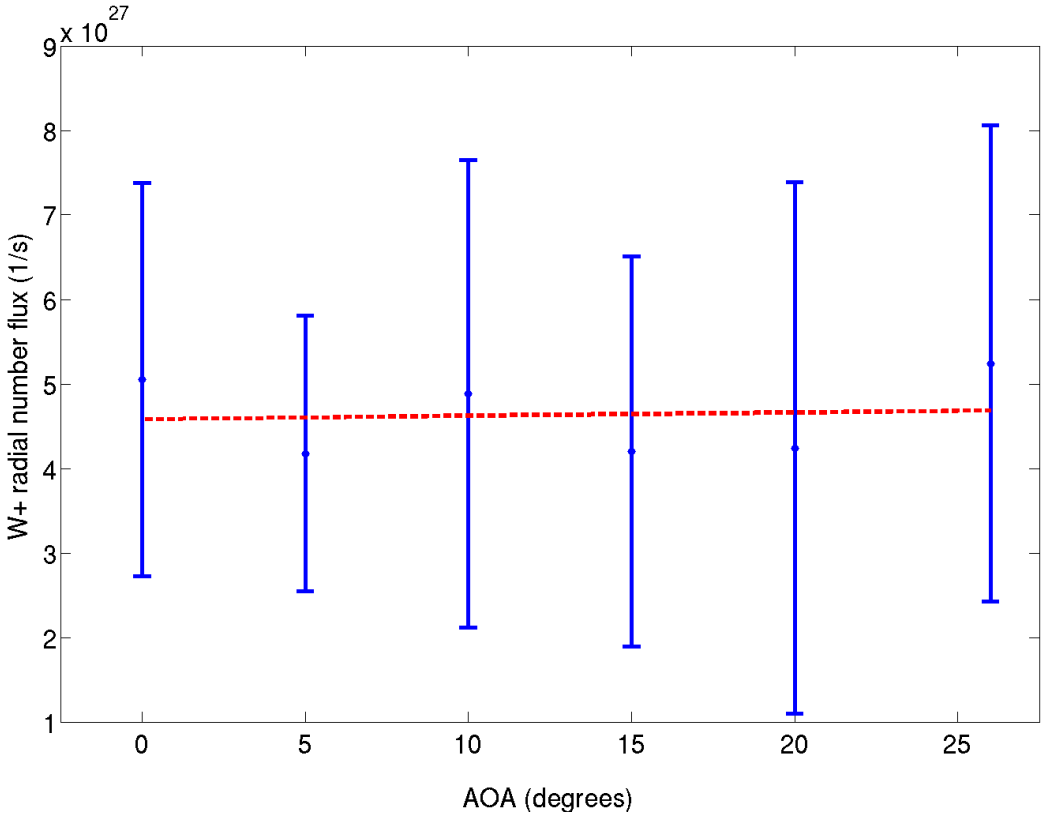

Figure 6.7 Radial W+ flux at r = 15 R_S vs. AOA

between radial transport in the inner and middle magnetosphere and Saturn's orbital position. The raw W+ radial flux vs. time data for these intervals are included in Appendix A2 for reference (Figure A2.5).

An FFT analysis of the radial flux data for the range of AOAs in Figure 6.7 reveals that while there is a certain range of frequencies that is prominent at several AOA values (0.2-0.4 × 10^{-4} Hz), there is no overall trend to the frequency spectra (see Appendix A2, Figure A2.7). This suggests that there are no underlying fundamental frequencies at which outflow structures develop and shed mass over the timescales that we have simulation data for (i.e.: different ranges would yield different spectra depending on the local conditions controlling the development of outflow structure), or that longer

runs comprising several transport periods (T_{trans} ~ 100 hrs, see section 5.2) are required to obtain sufficient data for statistically significant results. Using the range of simulation data available, we conclude that it is unlikely that the frequencies of outflow structures are related to the fundamental periodicities observed in Saturn's magnetosphere. Figure A2.6 in Appendix A2 shows an animation of the equatorial W+ density and electron temperature contours at equinox to further illustrate that there are few differences in qualitative terms between the evolution of outflow structures at equinox and solstice (compare to Figure A1.2).

6.3.3 Comparison of radial profiles

As we have established that the plasma sheet is largely flat inside of $r = 10\ R_S$, the correlation of W+ production with AOA must be due to second order effects that are not directly related to plasma sheet curvature. Figure 6.8 shows radial profiles of electron temperature as well as proton and water group ion density at $z = 0$ (equatorial plane) in order to understand what might be driving this trend. The equinox data (blue and green) are overlaid on the solstice data from Figures 4.2 and 4.3 (see Section 4.1), and show the mean values and the envelope containing 95% of all observations. To a first approximation, the mean profiles and envelopes for $r < 10\ R_S$ at both solstice and equinox are very similar, showing that the inner magnetosphere is not strongly affected by seasonal variability, in agreement with our previous statements. The greatest deviation from occurs for $r > 10\ R_S$ in the proton and W+ density profiles, but this is due solely to the plasma sheet curvature: we expect to find higher densities in the $z = 0$ plane at equinox because at AOA = 0° the rotational and magnetic equatorial planes are aligned,

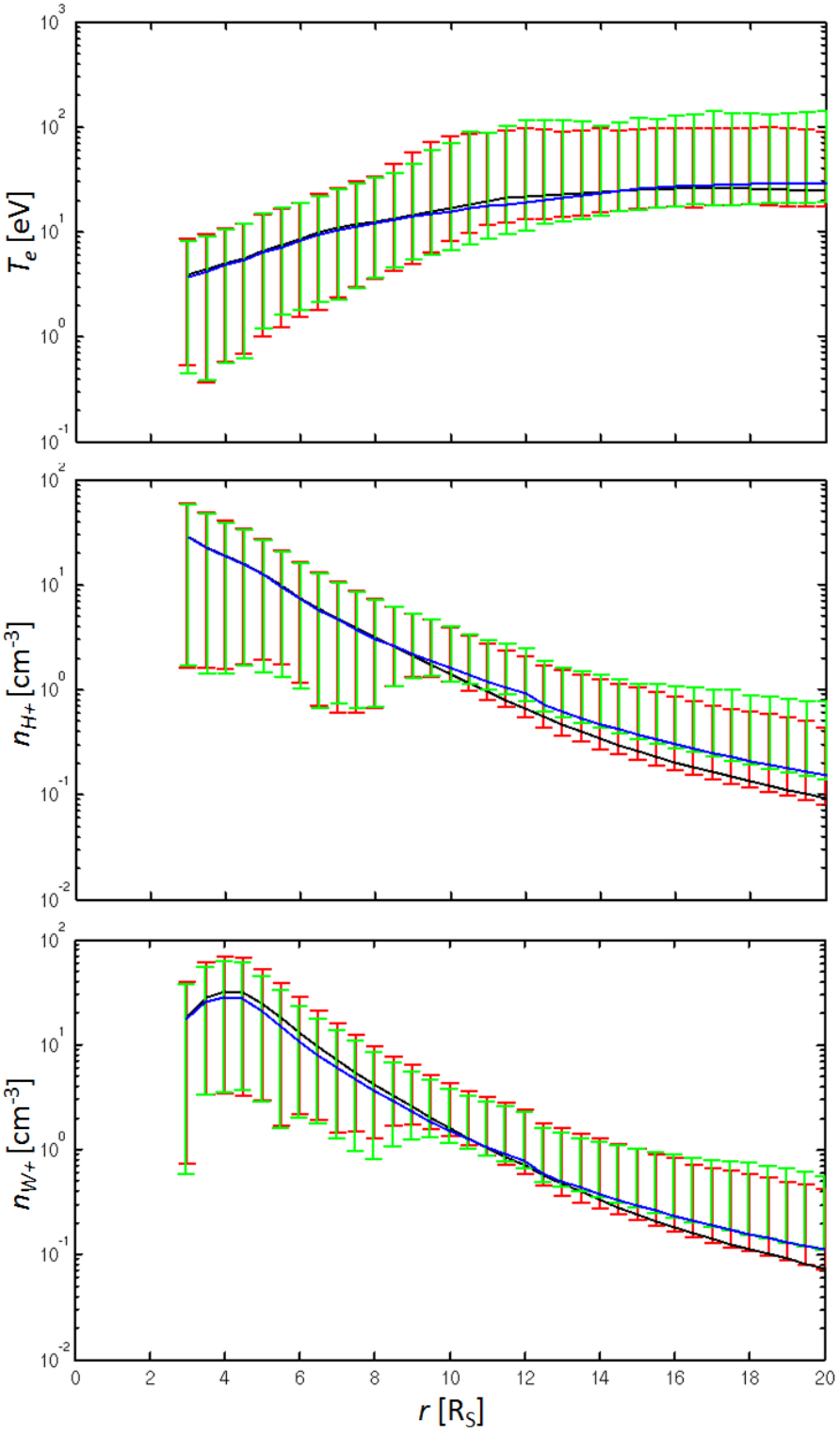

Figure 6.8 Radial profiles of at z = 0 (from top to bottom) electron temperature, proton density, and W+ density at equinox (blue lines [mean] and green bars [mean ± 2σ]) and solstice (black lines and red bars)

so the highest plasma densities would therefore no longer be displaced from $z = 0$ as they would be for AOA $\neq 0°$.

However, changing curvature outside of $r = 10\ R_S$ cannot account for changes in the global ionization rate, since the density of neutrals outside this distance is negligible. Moreover, the electron temperature, which determines the impact-ionization cross section is close to identical at equinox and solstice, suggesting that this is not driving the trend seen in Figure 6.6. The same is true for the proton density, but at equinox for $r < 8\ R_S$, we do see a small decrease in the mean W+ density. Since our electron density is treated as the sum of the ion densities (to ensure quasi-neutrality), this small decrease seen at equinox may be what is driving the change in global ionization rate with AOA. However, this is a very small difference, and well within the envelopes of variability. It may thus be very difficult to discern this effect from the *in situ* data from Cassini.

6.4 Summary of findings

In terms of overall morphology, the results of the updated multifluid model incorporating plasma-neutral interactions accurately reproduces the mean curvature of Saturn's plasma sheet at solstice and, while the decrease in curvature with decreasing AOA is in good agreement with the analytic formulation from *Arridge et al.* [2008]. The plasma sheet is highly dynamic at all local times, with the greatest variability presenting at the dayside. The characteristic timescale of small-scale northward-and-southward plasma sheet motion is on the order of minutes to hours, while the overall dynamics of the plasma sheet do not change appreciably from solstice to equinox. An interesting deviation from the mean profile is found at midnight, where the mean plasma sheet curves consistently southwards at all AOAs (southward curvature decreases with AOA).

Our investigation of the plasma sheet dynamics reveals that the plasma sheet in the vicinity of midnight experiences substantial "flapping" motions which drive the sheet into the southern hemisphere most of the time. These southward excursions are sometimes but not always associated with accelerated tailward plasma flows in the same region.

While there is a weak but discernible dependence of global W+ production rate on AOA, there is no such relationship between radial flux and AOA. We conclude that Saturn's orbital position is not a strong driver of internal dynamics, especially in the inner and middle magnetosphere. This is reasonable, since both the mean and instantaneous plasma sheet morphologies across all AOA values tested in this chapter show that the sheet is essentially flat in the inner magnetosphere. As such, radial transport and mass- and momentum-loading are not significantly affected by changes in AOA. There may be second order effects (e.g.: whether injections of hot, outer-magnetosphere plasma change with AOA, thus changing the inner magnetosphere plasma temperature), but the current state of the model and our resolution limitations preclude our investigating some of these effects (see section with injection analysis). Moreover, we have also shown that perturbations in upstream conditions are at least as important in producing changes in behavior as seasonal changes. This means that while certain trends (e.g.: the seasonal variability of W+ production) may be extracted from simulation data, and may furthermore accurately reflect how the magnetosphere behaves under steady conditions, they are unlikely to be extracted from *in situ* data due to the fact that the upstream conditions are constantly changing. In effect, beyond the broad morphological changes due to the changing angle of attack over Saturn's orbit, we find that there is little evidence of seasonal variability in Saturn's magnetospheric dynamics.

CHAPTER 7

MULTIFLUID INVESTIGATION OF SATURN'S MAGNETOTAIL

We now discuss the results of a short exploratory study of the dynamics of Saturn's magnetotail using the updated multifluid model. In chapter 2 we described the two major processes that affect the magnetotails of rotationally-driven magnetospheres, the Vasyliunas and Dungey cycles (see section 2.4). We focus first on the Vasyliunas cycle, examining the flow of water group ions in Saturn's magnetotail with an emphasis on the spatial distribution of W+ flows as well as the rate at which mass is lost downtail. We then briefly describe a plasmoid observed by a virtual spacecraft placed downtail at midnight and slightly above the mean plasma sheet location ($\boldsymbol{x}$ = [40, 0, 2] R_S), the characteristics of which could be ascribed to either the Dungey or Vasyliunas cycles. All results in this chapter come from a simulation with steady solar wind conditions, where AOA = 0° (equinox), and the IMF is antiparallel to the magnetic field at the bow of the magnetopause ($\boldsymbol{B}_{IMF}$ = [0, 0, 0.25] nT), thus allowing reconnection on the dayside. We chose the equinox viewing geometry as it ensures that any plasmoids produced will largely remain in the equatorial plane of our simulation grid, simplifying visualization.

7.1 Water group plasma loss down the magnetotail

The highly dynamic behavior and rapid motion of plasmoids makes them very difficult to visualize, especially if one attempts to obtain time series showing the development of an individual plasmoid. Like those of all previous modeling studies, the plasmoids from our simulation results all have a flux-rope geometries. Figures 7.1a and b show a representative example of a flux-rope plasmoid in the pre-midnight sector of

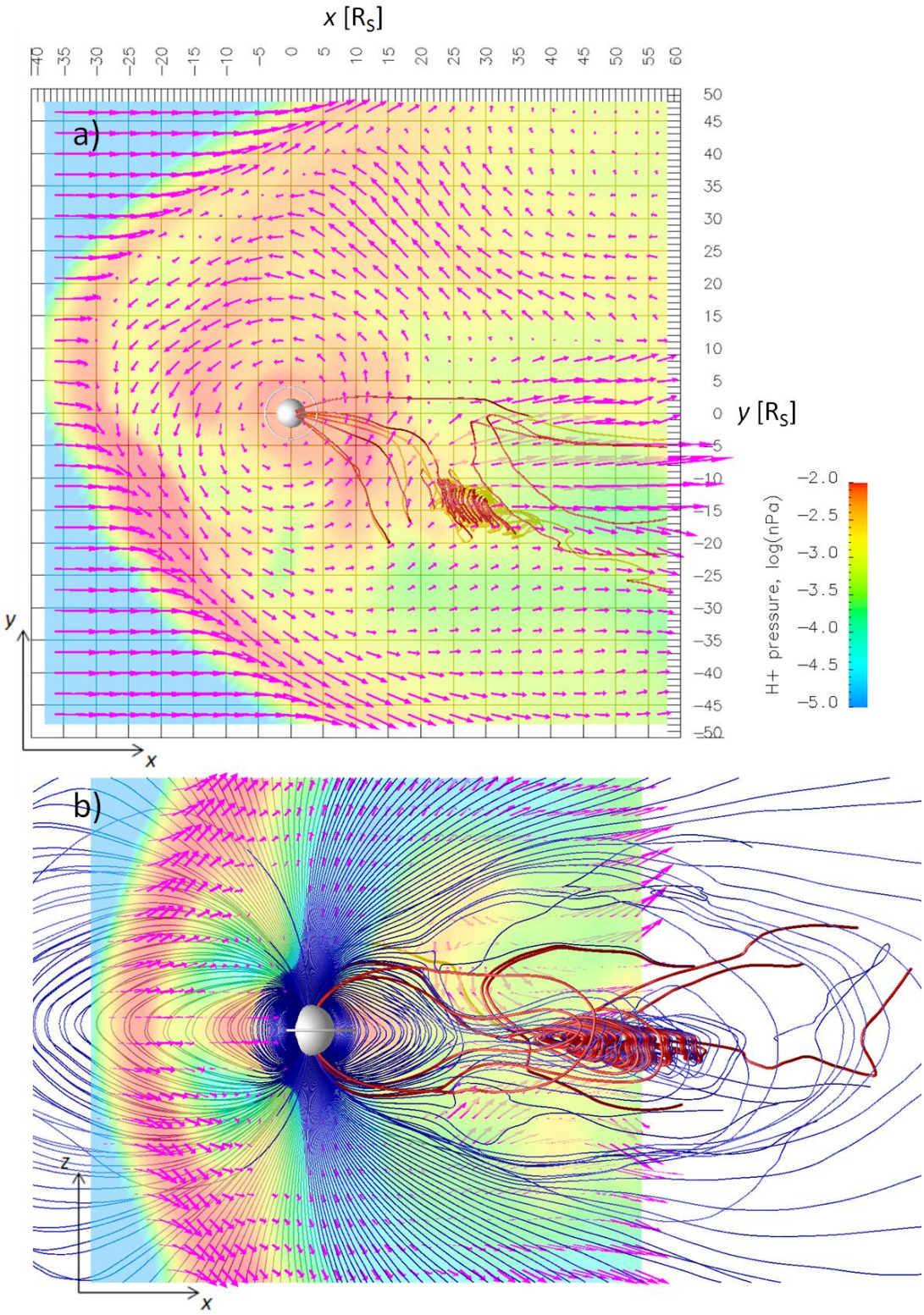

Figure 7.1 Snapshot of developing flux rope plasmoid (red field lines) overlaid on planetary field (blue field lines), H+ pressure contours, and total plasma velocity, a) equatorial view, b) rotated meridional view (60° rotation in *z* in corotation direction)

Saturn's magnetosphere. Such flux ropes form, reconnect, and flow downtail continuously in the dusk sector. The curled loop structure of the evolving plasmoid is visible in both Figures 7.1a and b, with the axis of the center of the plasmoid approximately parallel to the *x*-axis. The axes of the pre-midnight plasmoids produced by our simulation are found at various orientations, but are generally aligned with or close to the *x*-*y* plane. Figure 7.1b shows that the developing flux rope is enclosed by closed field lines originating from the planet, suggesting that this is an example of closed flux reconnection, and thus part of the Vasyliunas cycle [*Vasyliunas*, 1983]. Note that the velocity in the vicinity of the flux rope is predominantly in the positive *x* direction, implying that the plasmoid is being advected tailward.

Given our examination of the evolution of outflow structures and the manner in which they shed mass as they pass through the vicinity of 21:00 hrs SLT (see section 5.2, Figure 5.3), we thus expect that plasmoids formed due to closed-flux reconnection between dusk and midnight are responsible for transporting W+ plasma created in the inner magnetosphere downtail. In order to confirm this, we present Figure 7.2, showing a time sequence of the mass flux of water group plasma in the *x*-direction on the *y*-*z* plane (looking Sunwards) at three locations along the magnetotail, x = 20, 30, and 40 R_S. Note the presence of the dusk magnetopause boundary at x = 20 R_S on the far left of the image, which is absent at x = 30 and 40 R_S due to the flaring of the magnetopause. The flow of water group plasma is highly confined spatially, such that W+ flows downtail only in the pre-midnight sector along the plasma sheet (i.e. $y < 0$, $|z| < 10$ R_S). If we examine a single time step we find that the morphologies of the W+ flow structures at each *x* location exhibit something resembling self-similarity. For example, at every *x* location in

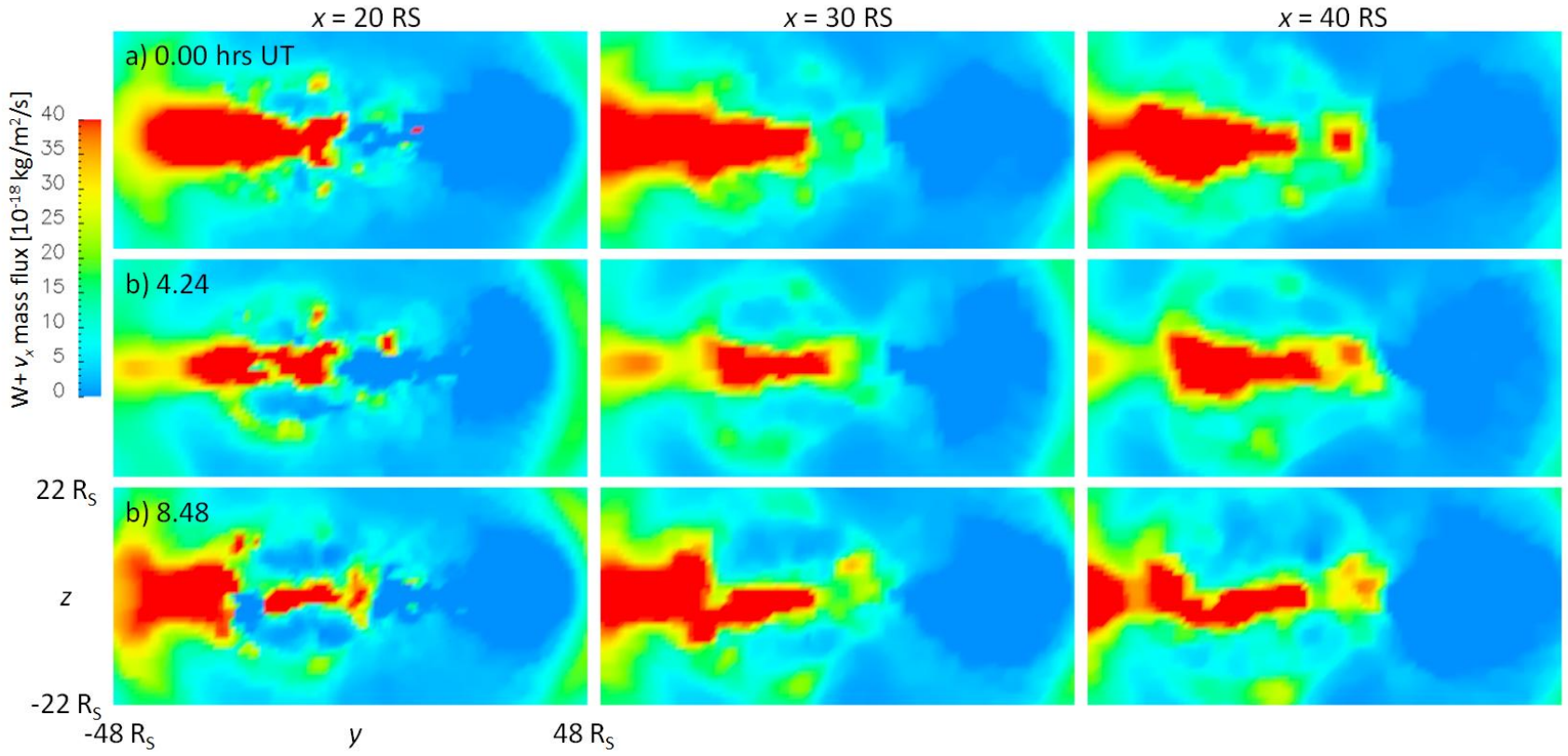

Figure 7.2 Downtail (*x*-direction) W+ mass flux in the in the *y*-*z* plane at (from L-R) *x* = 20, 30, and 40 R_S, over approximately a single Saturn rotation a) 0 T_S, b) 0.4 T_S, and c) 0.8 T_S

Figure 7.2c (0.8 T_S), the downtail W+ flow can be separated into two regions, one that is very thin in *z* immediately before midnight, and another extending to the dusk magnetopause where the flow is less confined, with both regions being separated by a gap at $y \approx -25\ R_S$. The flow structure evolves in time, with the morphology changing on a timescale of tens of minutes to hours. Over the course of the 0.8 T_S sequence shown in Figure 7.2, the downtail flow at $x = 20\ R_S$ evolves from a single structure at 0 hrs UT to the bifurcated structure at 8.48 UT described above. Despite the seeming self-similarity at any given time step, it is unlikely that these structures stretching tens of Saturn radii downtail are large plasmoids or flux ropes. They may instead be composed of trains of plasmoids ranging from those of a similar size to the flux rope in Figure 7.1 to ones that are smaller than our simulation can resolve in this region. In order to better illustrate the dynamic and evolving nature of the tailward W+ flow, we have included an animation of this process in section A3 of the appendix (see Figure A3.1).

Figure 7.3 shows the time-averaged linear W+ mass flux across the *y*-axis, obtained by integrating over the entire duration of the model output (~35 hrs, or 3.4 T_S) and then over *z*. This plot is essentially a proxy for the time-averaged flow along the plasma sheet, and is in broad agreement with the previous figure. Moreover, Figure 7.3 also shows that not only is the downtail W+ flow concentrated in the pre-midnight sector, but the bifurcation of the flow seen in Figure 7.2c is typical of the flow field in this region, with the greater flow rate found in the segment that is further away from midnight ($y < -12\ R_S$). On average, the post-midnight sector contains planetward flows, which are much smaller in magnitude. The decrease in the mean linear mass flux with increasing *x* distance is likely due to the flaring of the magnetopause: at $x = 30$ and $40\ R_S$, the dusk-

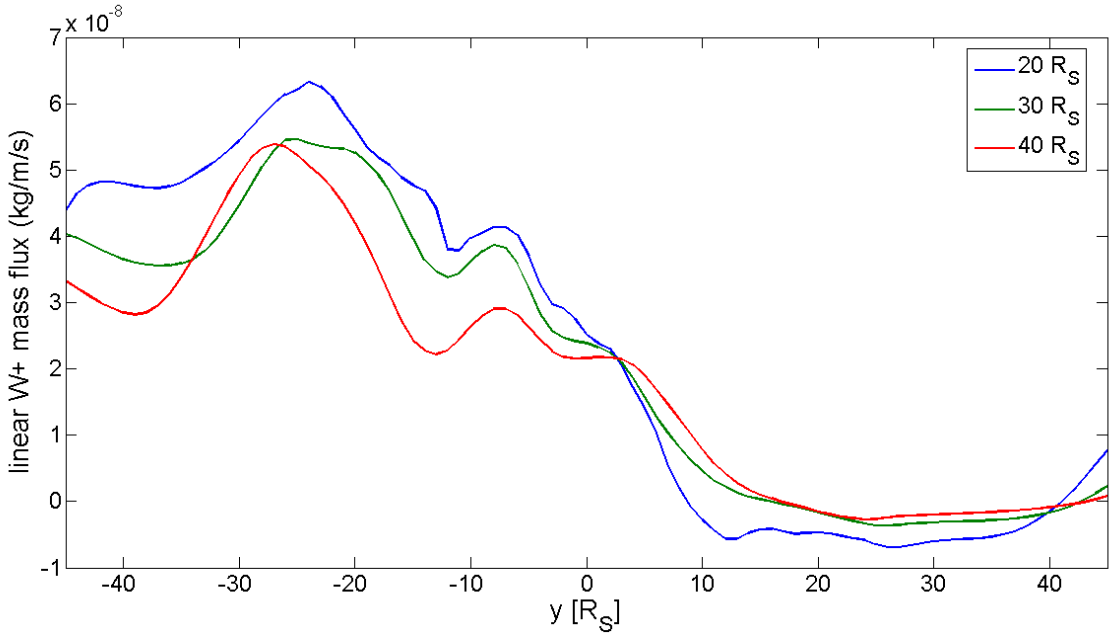

Figure 7.3 Linear *x*-direction mass flux of W+ across the *y*-axis at x = 20, 30, and 40 R_S

side magnetopause boundary is outside the frame of the images in Figure 7.2, thus the downtail W+ transport in this region would not be included in our calculation.

By also integrating across *y* for the entire available duration of the simulation we obtain the mean W+ mass flux at each *x* location in Figure 7.2: 138 kg/s at x = 20 R_S, 125 kg/s at x = 30 R_S, and 110 kg/s at x = 40 R_S. These values are in reasonable agreement with the range of rates of radial transport that we calculated in Section 6.3.2. In Figure 7.4, we show the results of integrating the total *x*-direction W+ mass flux at every time step, which gives an instantaneous value for mass flux through each plane over the interval under consideration. Consistent with our observations about the variability in radial flux rate at r = 15 R_S from Section 6.3.2, we find that the total rate of mass flux at each *x* location is also highly variable, with maximum values several times that of the

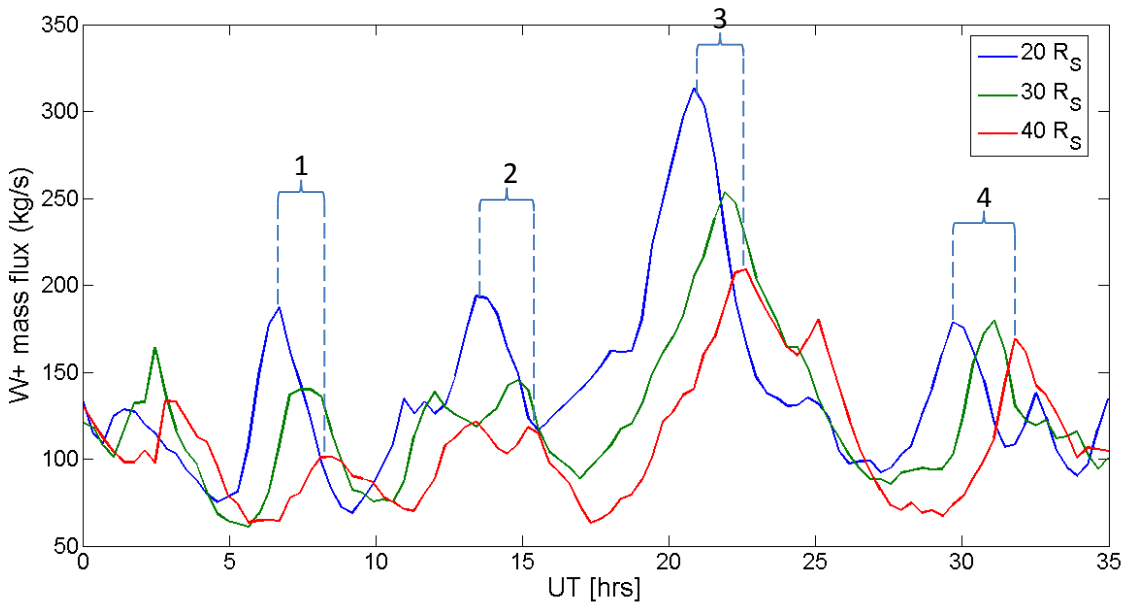

Figure 7.4 Total *x*-direction mass flux of W+ plasma at x = 20, 30, and 40 R_S

time-averaged values stated above. This is consistent with a process is highly dependent on the local plasma and magnetic field conditions, which is the case both with the initiation and evolution of the outflow structures, as well as the development and shedding of plasmoids. Figure 7.4 is annotated with the numbers 1 to 4, which indicate four specific events where the tailward mass flux spikes above the mean. The self-similarity that we discussed earlier means that the spike is visible at all three x locations, and is delayed in time with increasing tailward distance. We have used these delays, read as the time between the peaks at x = 20 and 40 R_S, as an approximation for the travel time which enables us to calculate transport velocities, if these structures are indeed indicative of the tailward flow of a series of small-scale plasmoids. We therefore obtain pre-dusk plasmoid velocities of approximately 190 km/s, which is significantly slower than the large-scale loop plasmoids observed in the post-midnight sector by Cassini (~800 km/s,

Jackman et al. [2014]). This may be due to the smaller size of these plasmoids, as the dipolarization and acceleration during reconnection would be less energetic as plasmoid size decreases.

7.2 Plasmoid properties

Plasmoids are generally identified using their magnetic field characteristics. As we discussed in Section 2.4.3, there are specific magnetic field signatures for flux ropes and loops. In this section, we examine data from a virtual spacecraft placed in the midnight magnetotail in order to confirm that we are able to characterize the plasmoid from magnetic field and plasma data. Figure 7.5 shows the particular flux rope of interest, while the position of the virtual spacecraft is denoted by the blue star ($\boldsymbol{x}$ = [40,0,2] R_S). The developing flux rope itself is the tightly-wound loop structure in the vicinity of midnight extending from x = 35 to 55 R_S, marked by the black circle. This structure is larger than the plasmoid in Figure 7.1 by a factor of two or three, making this a large plasmoid of the scale studied by *Jackman et al.* [2014]. The flux rope has been evolving prior to the time step depicted in Figure 7.5, but still remains attached to the planet. The axis of symmetry across the flux rope is lies in the *x*-*y* plane, as is the case for most of the large-scale flux ropes observed in this region. The scale and evolution of these plasmoids is reminiscent of the time series presented in *Kidder et al.* [2012].

We present the data from the virtual spacecraft in the stack plot in Figure 7.6, showing how the perturbation magnetic field strength $|\boldsymbol{B}|$ and the *z*-component of the magnetic field B_z (i.e.: minus the dipole field values), and the number densities of protons and W+ ions, n_{H+} and n_{W+}, vary at the spacecraft location. The dashed lines show the approximate start and end of plasmoid signature. In order to identify the passage of the

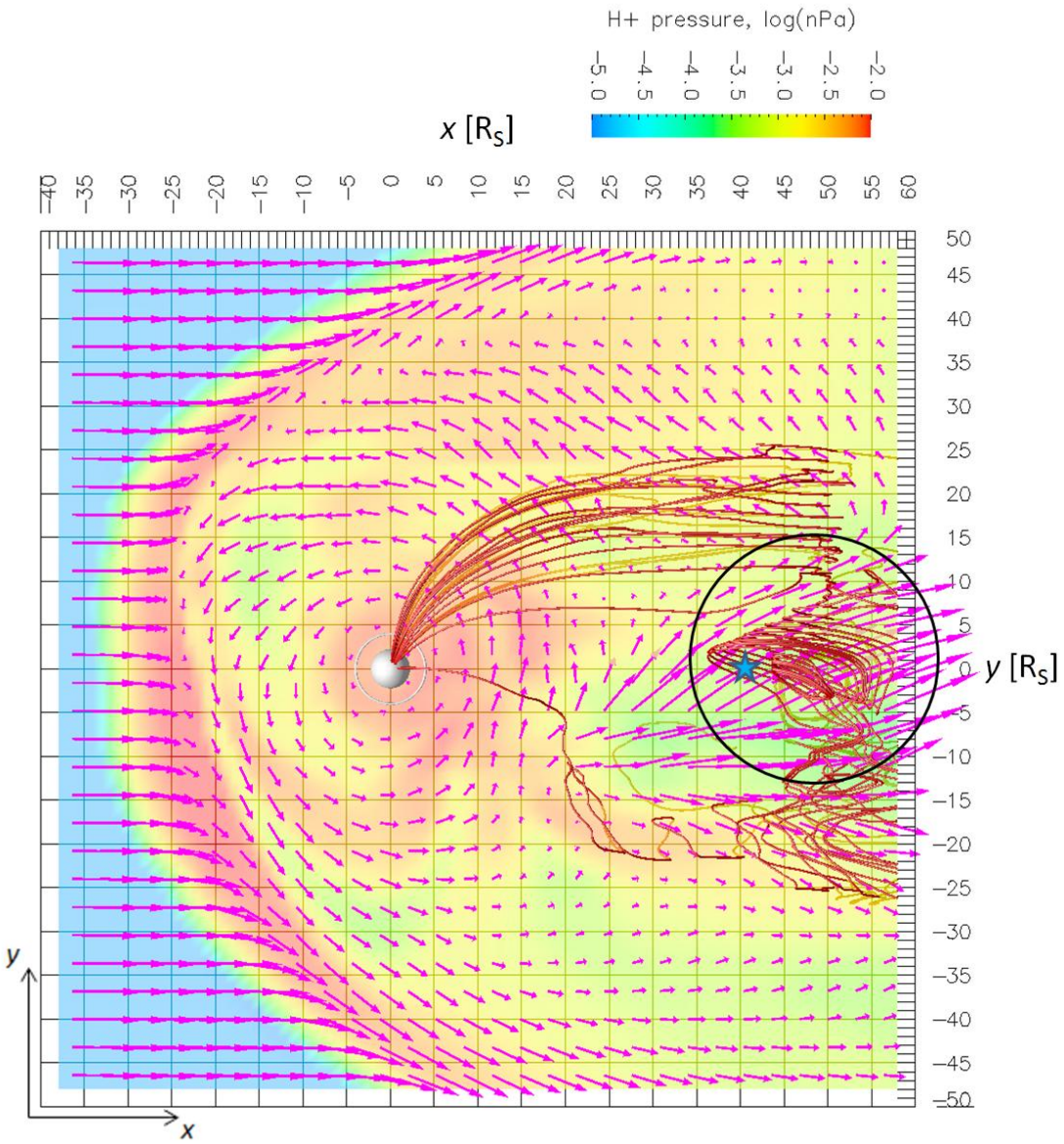

Figure 7.5 Equatorial view of flux rope plasmoid at 5.30 hrs UT (developing flux rope enclosed by black circle)

plasmoid, we rely on a number of indicators, specifically a drop in total magnetic field strength, the turning a specific magnetic field component, and an increase in plasma density (see Section 2.2.2). The event occurring between 4.5 and 6 hrs UT in Figure 7.6 satisfies all these criteria, with a 50% drop in the perturbation magnetic field strength, a turning in the perturbation B_z component, and a 50% increase over the local mean density

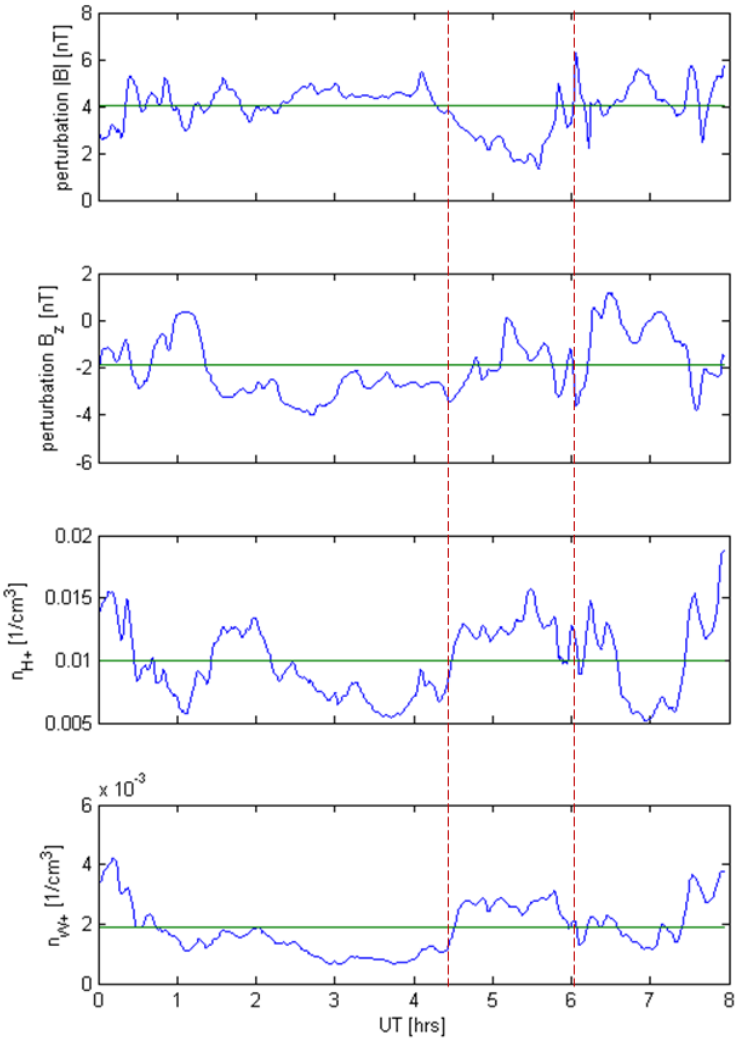

Figure 7.6 Virtual spacecraft data output vs. UT

of both W+ and protons. However, whether this flux rope is part of the Vasyliunas or Dungey cycle is ambiguous, as its location is such that it could be due to either process, and the relative abundances of protons and water group ions do not uniquely indicate if it results from open or close flux reconnection.

7.3 Summary of findings

Our brief investigation of the dynamics of Saturn's magnetotail has revealed that most of the water group plasma flows anti-Sunward in the pre-midnight sector of the plasma sheet. This flow is highly variable but nevertheless continuous. Combined with the creation of small-scale flux rope plasmoids in the pre-midnight sector, this suggests that the Vasyliunas cycle at Saturn is completed by a stream of small-scale plasmoids which are formed from constant closed-flux reconnection and are then advected tailwards. Quantification of the tailward flow of W+ reveals excellent agreement with the radial flux rates calculated in Chapter 5, and exhibits similarly high variability. It is clear that for tailward distances up to $x = 40\ R_S$, most of the water group plasma remains in the magnetotail, with potential loss mechanisms (e.g.: through the dusk-side magnetopause by the Kelvin-Helmholtz instability) either not proving important in this region, or occurring on scales that are too small to resolve with the multifluid model.

We have also shown that the updated multifluid model with plasma-neutral interactions produces large-scale flux rope plasmoids in vicinity of midnight and in the post-midnight sector similar to those of previous investigators. Virtual spacecraft data revealed that the passage of a plasmoid can be discerned using well-established criteria. While these plasmoids are not of the loop type observed at Saturn by Cassini, they are an important signature of the Vasyliunas and Dungey cycles. This lays the foundation for future studies that will examine how to differentiate between plasmoids produced by either open or closed flux reconnection from the model results, and therefore determine how plasmoid content, size, and morphology varies depending on which their role in

Saturn's magnetospheric dynamics. Further examination of the deep tail may also reveal exactly how water group plasma exits the magnetosphere.

CHAPTER 8

CONCLUSIONS AND FUTURE WORK

8.1 Conclusions

In this dissertation, we have presented a modified and updated version of the Saturn multifluid multiscale model that incorporates self-consistent plasma-neutral interactions. We have validated this model against CAPS and MAG instrument data from the Cassini probe, and found that the simulation output matches inner magnetosphere plasma flows and conditions with more accuracy than any previous attempts. We were able to reproduce inner magnetosphere plasma density, pressure, and temperature profiles within an order of magnitude or less within the range $3 < r < 10\ R_S$, where the mass- and momentum-loading processes take place. The incorporation of plasma-neutral interactions also minimizes the issue of supercorotation that many previously published global models of rotationally driven magnetospheres suffer from (e.g.: *Kidder et al.* [2012] and *Jia et al.* [2012b]). The self-consistent modeling of mass- and momentum-loading terms based on local plasma and neutral conditions therefore allowed us to simulate neutral cloud interactions such as electron-impact ionization, photoionization, and symmetric charge exchange collisions between W+ ions and water group neutrals, as well as the transport process that moves plasma produced in the inner magnetosphere radially outwards.

We have used this model to study various phenomena in Saturn's magnetosphere, beginning with the global production and radial transport of W+ plasma in the inner and middle magnetosphere ($r < 20\ R_S$). We found that the updated model produces mean

global W+ production rates ($73.1 < S_{W+} < 79.6$ kg/s across a range of AOA values) that fall well within the range of estimates based on *in situ* data and chemical modeling. The temporal variability of S_{W+} under a given set of steady-state upstream conditions is relatively small (~10%), due to the fact that most of new W+ plasma is produced in the region $3 < r < 5$ R_S, deep in the inner magnetosphere, where the neutral and electron densities are highest. The spatial and temporal variability of electron densities and temperatures in this region are very low, resulting in low variability in the rate of ionizing electron-neutral collisions. We briefly examined the ability of a radially-dependent hot electron sub-population (T_e = 200 eV) based on density profiles from *Schippers et al.* [2008] to influence the overall rate of ionization, but determined that the densities of these hot electrons in those regions where neutrals were abundant were simply too low to produce a significant effect. Most of the ionization is therefore carried out by the tail of the thermal electron population deep in the inner magnetosphere.

Our simulation results showed that the radial outflow process is highly dynamic, with the initiation, growth, and shedding of plasma by the outflow structures being strongly dependent on local plasma and magnetic field conditions. We examined this process qualitatively by considering time series of equatorial W+ contours, and quantitatively by calculating the radial flux of water group plasma at r = 15 R_S. Compared to the production process the radial transport is extremely variable, with a time averaged mean mass flux of 136 kg/s and an instantaneous flux that deviated from the mean by up to 60% at southern solstice under parallel IMF conditions. Since radial transport is dependent on the development of outflow structures, this extreme rate of variability is not surprising.

Our investigation of the effects seasonal change on Saturn's magnetosphere by varying the angle of attack (AOA) showed that the "bowl" morphology at southern solstice is a good approximation of the time averaged shape of the plasma sheet when compared to the analytic solution presented by *Arridge et al.* [2008], assuming that one uses local time-dependent values for the hinging distance R_H. We found that our simulation results for plasma sheet shape were in reasonable agreement with this analytic expression, using the R_H values determined at solstice by inspection, over a range of AOA values from southern solstice to equinox. However, our simulation also showed that the plasma sheet is considerably more dynamic than the simple "bowl" morphology suggests. There are perturbations along the plasma sheet surface that cause localized regions to move northwards or southwards on the timescales of a few tens of minutes. There is also a region in the nightside magnetotail in the vicinity of midnight which exhibits a "flapping" behavior, which results in the mean position of the plasma sheet being deflected below the equator (i.e.: negative curvature compared to the rest of the sheet). These southward excursions at midnight are present at all tested AOA values and are sometimes associated with the tailward acceleration of plasma flows. However, beyond the curvature, there does not appear to be differences in plasma sheet dynamics at the seasonal extremes of equinox and solstice. Likewise, the plasma sheet in the inner magnetosphere remains remarkably flat in both cases, with the rotational and magnetic equators being closely aligned at all AOA values for $r < 10\ R_S$. This flat inner magnetosphere plasma sheet is the most likely explanation for why the W+ production and radial transport processes are relatively unaffected by changing AOA. The former increases slightly with increasing AOA, while the latter appears to have no dependence

whatsoever on seasonal changes. While changes in season may have a measurable effect on some processes in Saturn's magnetosphere under prolonged steady-state conditions, the large scale fluctuations that occur due to changes in upstream conditions or the development of outflow structures, plasmoids, and other complex, nonlinear global phenomena are far more important in determining the dynamics of this system.

Finally, we investigated the behavior of Saturn's magnetotail, focusing on the Vasyliunas and Dungey cycles. We described the flow of water group plasma up to a distance of 40 R_S downtail from the planet, showing that the tailward flows are confined to the pre-midnight plasma sheet. The tailward mass flux rate is comparable to the radial flux rate mentioned previously in both magnitude and variability, while the return flows along the post-midnight plasma sheet are less than 10% of the pre-midnight flow, suggesting that essentially all of the W+ transported out of the inner magnetosphere flows downtail and to exit the magnetosphere. The exact mechanism by which this plasma is transported is not yet clear. Small-scale flux rope plasmoids are visible in the pre-midnight sector, and appear to be continuously forming and moving downtail. However, we have not yet established if these flux ropes are still on closed field lines at x = 40 R_S. Using the downtail flow structure's approximate self-similarity, we have established that between x = 20 and 40 R_S, the flow moves at approximately 190 km/s, substantially slower than the large-scale plasmoids observed in the post-midnight sector by Cassini. We briefly examined a simulation output for a large-scale flux rope plasmoid in the vicinity of midnight, and showed that it was possible to use virtual spacecraft data to find plasmoids using their distinctive magnetic field structure and plasma content.

In summary, we have used our powerful new model to investigate the dynamics of Saturn's magnetosphere, and have been able to quantify for the first time key processes like the time rate of production of new W+ plasma from the neutral cloud, the radial flux of this plasma, and its eventual downtail flow. While Saturn's orbital location has a profound impact on the global morphology of the magnetosphere, our investigations have revealed that seasonal changes do not seem to affect the magnetosphere's dynamic behavior to a significant degree. We have thus verified that the inclusion of plasma-neutral interactions is vital to understanding the behavior of Saturn's inner magnetosphere, and have also established the accuracy of the model. It should thus prove useful in a slew of future projects to investigate other unanswered questions about Saturn's magnetosphere.

8.2 Future work

8.2.1 Further investigation of plasma production and transport

We have determined that the characteristic timescale of radial plasma transport in the inner magnetosphere is an order of magnitude longer than the rotation period. As we have very few instances of the simulation that have run beyond a single radial transport timescale, we have thus far been unable to quantify the variability in this process, and whether it drives variability in the frequency or behavior of outflow structures. An relatively simple extension of our previous work will therefore involve running our simulations continuously for several months of wall clock time in order to collect sufficient data to examine the variability of plasma production and transport on this longer timescale. This will be somewhat challenging, as we are not only constrained by

the very long times it takes to run these cases, but also in terms of obtaining sufficient storage on our cluster to store the output at the required temporal resolution.

Another potential avenue of investigation would be to examine the effects of treating the thermal electron population in the inner magnetosphere as having a long-tailed temperature distribution (i.e.: Kappa distribution), which would account for the warm populations observed throughout Saturn's magnetosphere. Since this would lead to increased ionization frequencies, this change would have significant effects on mass- and momentum-loading. We have always assumed that the electrons have a Maxwellian distribution, so any attempts to treat the electron population as having a Kappa distribution will have to involve the prescription of a value or values of Kappa by region. Moreover, such attempts will also have to include efforts to devise a computationally tractable way to integrate this distribution at every grid point in the inner magnetosphere, as this is more difficult than computing the tail of a Maxwellian as the Kappa distribution must be numerically integrated. One possible solution to this would be the use of a look-up table, similar to what we eventually employed for our Maxwellian population in order to improve performance. However, the simulation would no longer be fully self-consistent, as it would involve the *a priori* imposition of specific values of the Kappa parameter that would have to be taken from the publications of prior investigators. Nevertheless, this does not negate the utility and power of this model, and is thus a viable and valuable potential avenue of investigation.

8.2.2 Second-order effects of seasonal variation

Saturn's angle of attack relative to the solar wind is the most visible manifestation of the planet's changing seasonal conditions, but there two other effects that may

contribute to changes in magnetospheric behavior. Specifically, the change in UV irradiance over the course of Saturn's year (the difference between aphelion and perihelion is approximately 10% of the semi-major axis of the orbit) should drive changes in the rate of photoionization. Since we have obtained photoionization rate constants (k_{ph}) based on a position mid-way between aphelion and perihelion, a back-of-the-envelope calculation reveals that our photoionization rate might vary by up to 15% from the rates calculated from our simulation results under quiet Sun conditions. However, since we have shown that the overall W+ production due to photoionization rate is barely 6% of the global W+ production rate, this is not a significant change. However, the more important effect is likely to be the changing solar cycle. Since our results are based on UV irradiance during quiet Sun conditions, the active period of the Solar cycle can result in an increase in k_{ph} of 200-300%. This would result in a much larger increase in the photoionization contribution to W+ production, and would more importantly have important implications for the photodissociation that occurs in the neutral cloud. Thus one important avenue of investigation may be to investigate the implications of changing UV irradiance on both plasma-neutral interactions and the neutral cloud over the course of Saturn's year and the solar cycle.

Changes in UV irradiance will also change Saturn's ionospheric conductance. We believe a particularly interesting avenue of investigation would be applying a latitudinally varying ionospheric conductance to the inner boundary of our model, such as the one found in *Moore et al.* [2010]. This should impact the corotation lag of the inner and middle magnetosphere, as the Pedersen conductance plays a vital role in determining the distance of corotation breakdown [*Hill*, 1979]. However, this particular avenue may

prove problematic, as there has been very little work since 2010 on quantifying the changes in ionospheric conducanctace with season.

8.2.3 Response to dynamic perturbations

With the exception of the final chapter of this dissertation, where we created a step change in the IMF to instigate Dungey cycle open-flux reconnection, all of our data has come from instances where the simulation has been run long enough to reach a state of quasi-equilibrium. However, the utility of the multifluid model is that it is capable of accepting time-varying inputs for upstream conditions. Thus, it would be very interesting to subject the simulated magnetosphere to events such as corotating interaction regions, periodic forcing, or rapid changes in the IMF, all events that have been observed at Saturn, which result in the kind of fluctuations that mask trends such as the correlation that we observed between AOA and global W+ production rate. There exists a substantial body of literature describing these upstream conditions, as well as numerous publications in which investigators have used *in situ* data to analyze and quantify the response of Saturn's magnetosphere to these events. It would thus be exciting to see how our model handles such events, and whether interesting global behavior results that has not yet been deduced from Cassini data.

8.2.4 Magnetotail dynamics

Our investigation of magnetotail dynamics was exploratory and short in nature. Thus, there remains enormous scope for future projects. On a very simple level, it would be instructive to examine the downtail flow of W+ plasma at greater distances, to examine how it changes qualitatively and quantitatively. It is also important to understand the specific nature of downtail transport, i.e.: if this plasma is carried by small

or large plasmoids from the pre-midnight sector, and if so, where are the reconnection regions and what are their downtail speeds. Investigating the structure of the plasmoids themselves will be a challenging task as the flux ropes are not easy to visualize, and the tools at our disposal make it difficult to track the evolution of the single plasmoid over time as the structure deforms and moves downtail. Similar difficulties await investigators who are interested in examining the larger-sale post-midnight plasmoids, but it is important to understand whether these are part of the open-flux or closed-flux reconnection, and what role they have in removing plasma from Saturn's magnetosphere and transporting magnetic flux.

8.2.5 Incorporation of new model physics

Anisotropic ion pressures (i.e.: along and perpendicular to the magnetic field) have long been considered to be important in accounting for the total distribution of plasma pressures and temperatures throughout Saturn's magnetosphere [*Achilleos et al.*, 2010; *Sergis et al.*, 2010]. Work on another variant of the Saturn multifluid model at the University of Washington, Seattle by *Tilley et al.* [2015] incorporating the effects of anisotropic pressures have successfully simulated injection fingers that reach deeper into the inner magnetosphere, in better agreement with data. Thus, one extremely promising new avenue of investigation would be to combine this innovation with the modifications pioneered in our version of the model, to produce a more accurate depiction of Saturn's dynamic magnetosphere than has ever been achieved before. However, we do note that in both cases it is necessary to either wait until better computational resources become available, or search for additional ways in which to improve simulation performance, as

currently the performance of both versions of the global Saturn model have been adversely impacted by the addition of new physics.

APPENDIX A

SUPPORTING FIGURES AND ANIMATIONS

Appendix A contains figures that are used to conduct analyses or measurements that support but are not central to the main text, as well as the captions of animations that are helpful for visualizing Saturn's magnetospheric dynamics. The animations can be downloaded from the SMARTech thesis depository (smartech.gatech.edu)

A1. Chapter 5 supporting figures and animations

Figure A1.1 Animation of Figure 5.2 from 17.22-28.53 hrs UT. From left to right: electron temperature, election ionization frequency, and volumetric W+ production contours (filename: figure_a1.1.wmv)

Figure A1.2 Animation of solstice equatorial W+ density contours (left) from Figure 5.3 alongside electron temperature contours (right) for the interval 17.22-28.53 hrs UT (filename: figure_a1.2.wmv)

A2. Chapter 6 supporting figures and animations

Figure A2.1 Animation of *x*-*z* plane showing how the moving magnetopause can affect plasma sheet curvature. Contours are H+ pressure, arrows are the bulk plasma velocity, and the red lines represent the magnetic field inside the magnetopause (filename: figure_a2.1.wmv)

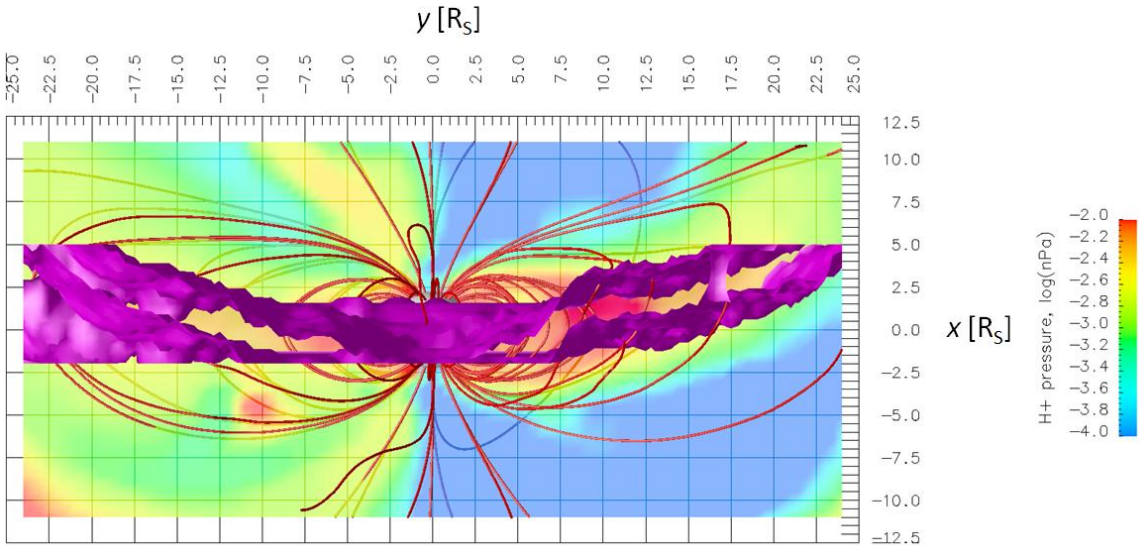

Figure A2.2 *y*-*z* view of solstice nightside plasma sheet at 30.65 hrs UT

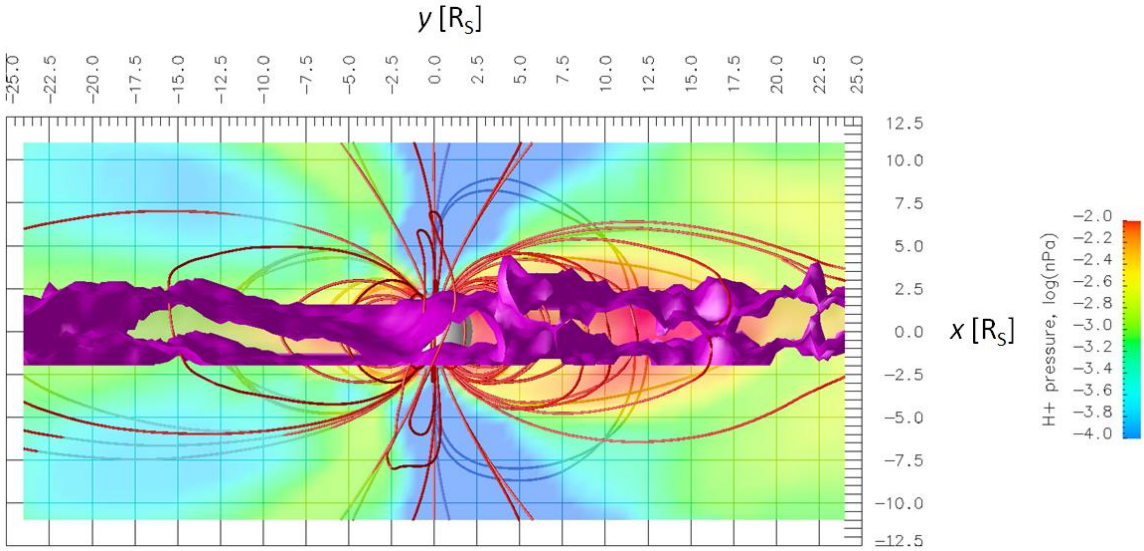

Figure A2.3 *y*-*z* view of equinox nightside plasma sheet at 30.65 hrs UT

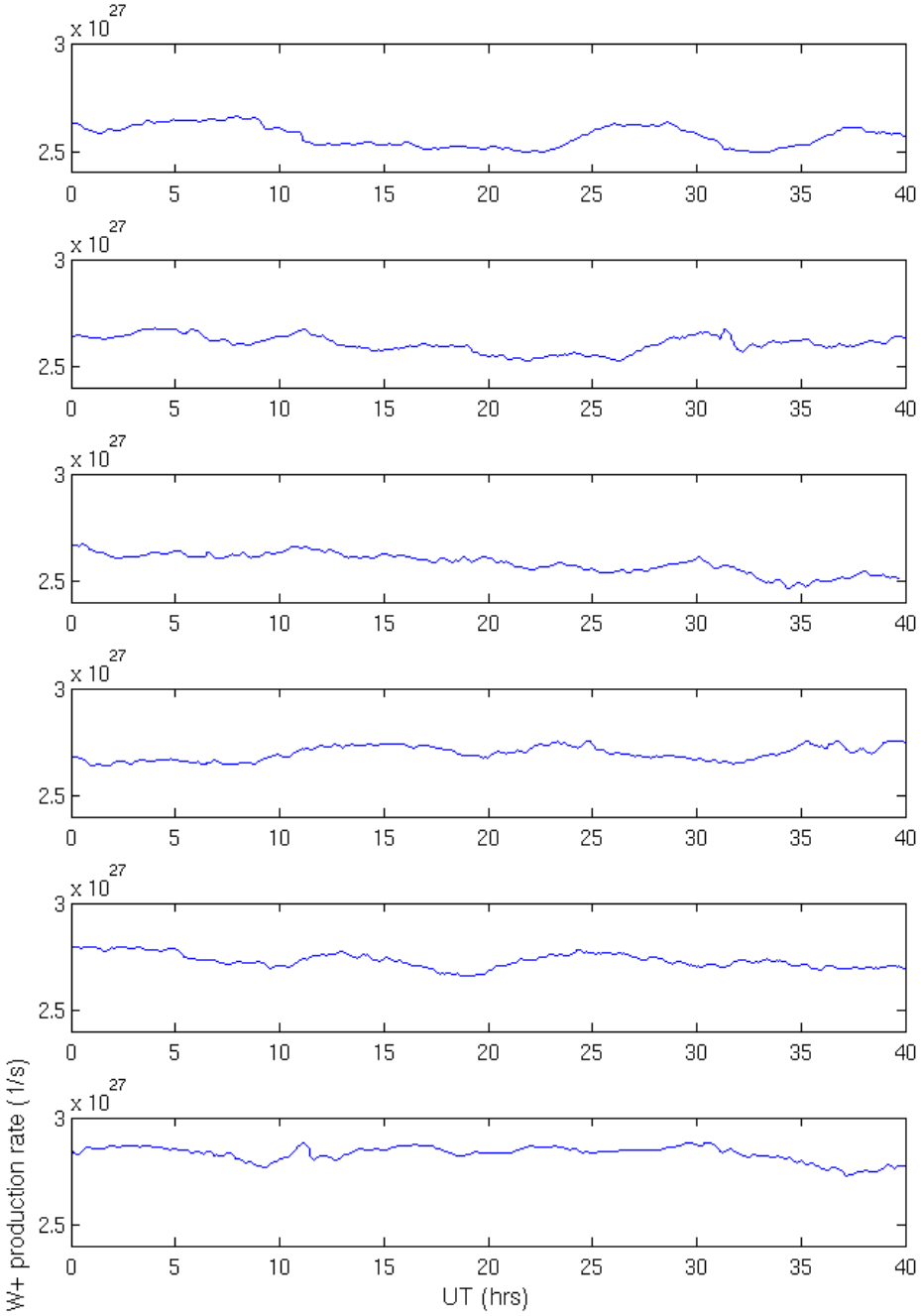

Figure A2.4 W+ production vs. *t* line plots. From top to bottom: AOA = 0° (equinox), 5°, 10°, 15°, 20°, 26° (southern solstice)

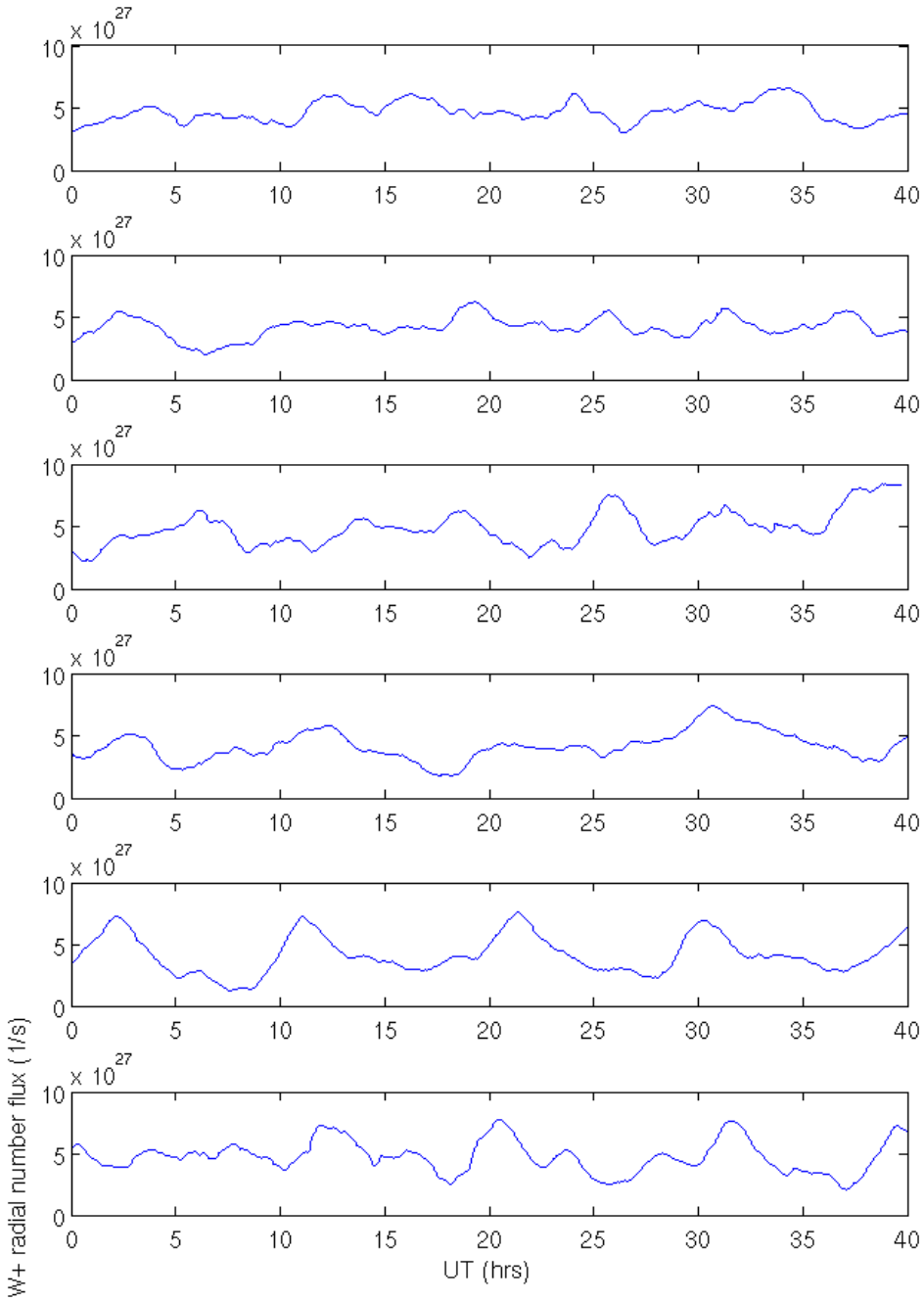

Figure A2.5 W+ radial flux at r = 15 R_S vs. t line plots. From top to bottom: AOA = 0° (equinox), 5°, 10°, 15°, 20°, 26° (southern solstice)

Figure A2.6 Animation of equinox equatorial W+ density contours (left) alongside electron temperature contours (right) for the interval 18.28-39.13 hrs UT (filename: figure_a2.6.wmv)

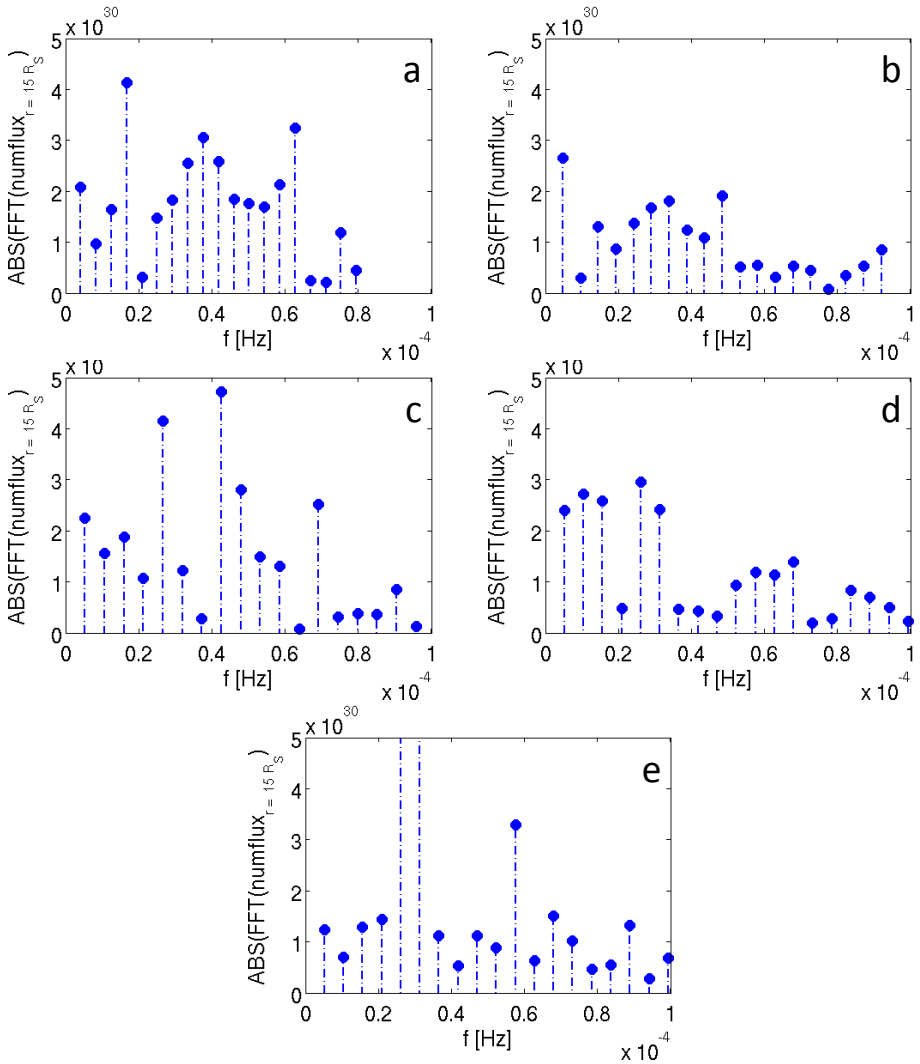

Figure A2.7 FFT frequency spectra of radial W+ flux vs. *t* signals. AOA = a) 0°, b) 5°, c) 10°, d) 15°, e) 20°

A3. Chapter 7 supporting figures and animations

Figure A3.1 Animation of Figure 7.2 (*x*-direction W+ mass flux contours in *y*-*z* plane) from 0-34.98 hrs UT. From top to bottom: x = 20, 30, 40 R_S (filename: figure_a3.1.wmv)

APPENDIX B

LARGE-SCALE CODE DEVELOPMENT FOR AMATEURS

This appendix is the result of years of experience modifying the Saturn multifluid code to both incorporate plasma-neutral interactions, as well as the subsequent work that was required to improve the performance of the simulation from abysmal to acceptable levels. In this time, I made numerous errors, all of which required a certain degree of backtracking. On a few occasions, that backtracking required repeating several months of worth of simulation runs. Unfortunately, most of these mistakes are the result of simply not having a formal computational background, otherwise I could simply say "go read *The Mythical Man Month* [*Brooks*, 1995]" and be done with it. As a result, I have decided to include this short post-mortem in the form of a series of exhortations to anyone who takes on this project after me, or more generally finds him- or herself working on a large-scale legacy physical model, and comes to this project with varying amounts of computing experience but without a formal computer science background.

Commandment 1. Thou shalt always use version control.

No exceptions! With easy-to-use, widely-adopted and supported offerings like Git and Mercurial available across platforms, there is no excuse at all to not use version control on all critical and non-critical code. The extent to which a research group uses version control may vary, and can be justified by whether a group works on a single code base or not, but the basic practices of constantly committing new changes, creating meaningful log entries, and cloning or branching repositories when experimenting with something new should be something every single group member should be doing. It

avoids mistakes accidentally wiping out months of work, it gives the reader a clear view of how a coder's thought process has developed over time when dealing with a particular task, it enables clearer organization of one's files, and it can act as a valuable tool to maintain tight control of code functionality and output while updating syntax or optimizing. If you are not using version control, you are shooting yourself in the foot.

Commandment 2. Thou shalt always comment your code

As far as is reasonable, document everything. A programmer never knows who might be reading her code and when, nor can she guarantee that her reasoning regarding how she laid things out will be clear to herself if she has to revisit a particular code block at some point in the future. When encountering large code bases for the first time, finding a bevy of subroutines which perform opaque functions helps no one, and can be extremely disheartening for the new student. If you are creating a subroutine or updating a code block, write clear comments that show the reader what you intend to do and where the limitations lie. If the algorithm you are implementing is complex, difficult to understand, unique, or not well known, include references (even if it is just to the pages in your notebook where you created the new concept).

Commandment 3. Thou shalt use meaningful variable and subroutine names

No stupid variable names. If you are angry, feel free to swear in the comments. If you are creating a variable that represents the x-velocity of ion fluid 3, do not call it ovelx. That way lies damnation, especially ion3vx works far better. At the very least it is more systematic, and does not rely on people remembering whether a species is truly represented by a given letter or means something else entirely. Similarly when creating a new subroutine out of an old one, let the reader know what the new subroutine does by

naming it something appropriate. If a program are three smoothing routines, I want to know what differentiates them.

Commandment 3.1. Thou shalt always use IMPLICT NONE

If this is an available feature, then you will do this, or face the wrath of everyone who works on it after you.

Commandment 4. Thou shalt prize readability over performance or economy

Computing power has come a long way in the last few decades, and problems that used to require a cluster or a Cray vector processor can now be done on a single compute node or even a workstation. There is little need to reuse variables in wildly different contexts just to save a little memory. Similarly, do not optimize prematurely. Most modern compilers can automatically apply simple optimizations, so techniques like loop-unrolling are unnecessary to implement by hand.

Commandment 5. Thou shalt always use top-down design techniques

If you make a change or create something new, plan it out ahead of time. No one cares if you use a notebook, an online or virtual notebook, or simply scribble on the walls of a padded cell (as long as the orderlies do not wipe it off later), but break a problem down, come up with solutions to each part, and only then translate it to code. This CS101-level material, and is described in any entry-level coding book.

Commandment 5.1 Thou shalt always run test cases

Using top-down design techniques is great, but you must also learn to understand when a new feature or block of code needs to be tested in isolation. It may seem like extra work, compared to integrating a change into the larger project right away, but the effects of such changes can often take a long time to become evident, especially when the

code already executes slowly, or when your change only affects a particular subdomain or portion of the code. Try to sanity-check things ahead of time.

Commandment 6. Thou shalt always conduct regular code reviews

I would be embarrassed to admit how many times I have created small (or not-so-small) bugs in my code that went unnoticed for months or occasionally years until either my advisor or one of my fellow students caught it. Oftentimes, this was while they were reading it for a reason unrelated to problems with simulation output, which makes me shudder to think just how much time I could have saved if we conduced regular (e.g.: monthly or bimonthly) formal reviews of each other's new code. I have found it very easy to say that we are all working on different projects, and that while the code base is similar or shares the same ancestry it would take too much brain power to continually keep up with how other versions are evolving, but in fact this was intellectual laziness speaking. If this does not grow informally in the group, it should be imposed top-down.

Commandment 7. Thou shalt become familiar the features of your tools

This goes beyond just knowing the syntax of your preferred language. A good programmer understands more granular features, such as how arrays are indexed and how they are stored in memory. One of the biggest wins in this work was figuring out that the original way in which the nested grid configuration was implemented in the array indices was slowing the simulation by a factor of two or three. The fix was relatively simple, but because I did not follow Commandment 1 at the time, took many more months than it should have. Nevertheless, this required my doing some research on my own into arrays were stored in Fortran, and how this differed from other languages like C++. Be prepared to do this work.

Commandment 8. Thou shalt implement project management values in your project

We often think of research as being hard to plan, as it often seems to rely on fortuitous discoveries or bursts of inspiration. However, I have observed that the most successful research projects stick to timetables and schedules. Feel free to build in time to experiment wildly or play around, but strive as hard as possible to hit your key milestones at the right times. When proposing a project, do not simply shoot for the moon. Figure out what is achievable, what is the single most valuable contribution in your proposal, and then structure your time accordingly. If you find that there is not enough time, then figure out how to simplify things. If you are not experienced enough to know how long things should take, talk to someone who is. A good place to start is reading good project management books. One that I highly recommend is "FIRE: How Fast, Inexpensive, Restrained, and Elegant Methods Ignite Innovation" [*Ward*, 2014]. I wound up reading less than nine months before defending this thesis, and recall slapping my forehead every dozen pages, thinking to myself "I could have saved four *weeks* when dealing with that problem if I understood this two years ago".

Commandment 9. Thou shalt learn at least one other computer language

Preferably something popular, and perhaps something object oriented if you are not familiar with one already. A language that satisfies both these criteria is Python, which would definitely help the student thinking of going into the private sector ("Fortran? You don't look 70..."), and is also popular in academia. The simple fact is broadening your skills will always pay off. Not only will it make you more marketable, it will also teach you more about the systems you work with from another perspective. This will both make you a better programmer on your project, but also make you a better

overall problem solver. Moreover, certain tools will not be around much longer. While the Fortran 77 code base appears to be quite robust, the fact is no one is coding anything new with this version of the language. Your time in grad school is finite, while your career moving forward is the rest of your life. Do everything you can to keep your skills and knowledge current.

Commandment 10. Thou shalt read "The Mythical Man Month"

A necessary (if not sufficient) condition to becoming a computational physics guru, you will not regret it.

REFERENCES

Achilleos, N., C. S. Arridge, C. Bertucci, C. M. Jackman, M. K. Dougherty, K. K. Khurana, and C. T. Russell (2008), Large-scale dynamics of Saturn's magnetopause: Observations by Cassini, *J. Geophys. Res.*, *113*(A11), A11209.

Achilleos, N., P. Guio, C. S. Arridge, N. Sergis, R. J. Wilson, M. F. Thomsen, and A. J. Coates (2010), Influence of hot plasma pressure on the global structure of Saturn's magnetodisk, *Geophys. Res. Lett.*, *37*(20), L20201.

André, N., M. K. Dougherty, C. T. Russell, J. S. Leisner, and K. K. Khurana (2005), Dynamics of the Saturnian inner magnetosphere: First inferences from the Cassini magnetometers about small-scale plasma transport in the magnetosphere, *Geophysical Research Letters*, *32*(14), n/a-n/a.

André, N., et al. (2007), Magnetic signatures of plasma-depleted flux tubes in the Saturnian inner magnetosphere, *Geophys. Res. Lett.*, *34*(14), L14108.

Arridge, C. S., K. K. Khurana, C. T. Russell, D. J. Southwood, N. Achilleos, M. K. Dougherty, A. J. Coates, and H. K. Leinweber (2008), Warping of Saturn's magnetospheric and magnetotail current sheets, *J. Geophys. Res.*, *113*(A8), A08217.

Arridge, C. S., et al. (2011a), Periodic motion of Saturn's nightside plasma sheet, *J. Geophys. Res.*, *116*(A11), A11205.

Arridge, C. S., et al. (2011b), Mapping Magnetospheric Equatorial Regions at Saturn from Cassini Prime Mission Observations, *Space Science Reviews*, *164*(1), 1-83.

Bagenal, F., and P. A. Delamere (2011), Flow of mass and energy in the magnetospheres of Jupiter and Saturn, *J. Geophys. Res.*, *116*(A5), A05209.

Baumjohann, W., and R. A. Treumann (1996), *Basic Space Plasma Physics*, 329 pp., Imperial College Press, Singapore.

Brooks, F. (1995), *The Mythical Man Month*, 2nd ed., 336 pp., Addison-Wesley Professional.

Burch, J. L., J. Goldstein, T. W. Hill, D. T. Young, F. J. Crary, A. J. Coates, N. André, W. S. Kurth, and E. C. Sittler, Jr. (2005), Properties of local plasma injections in Saturn's magnetosphere, *Geophys. Res. Lett.*, *32*(14), L14S02.

Burger, M. H., E. C. Sittler, R. E. Johnson, H. T. Smith, O. J. Tucker, and V. I. Shematovich (2007), Understanding the escape of water from Enceladus, *Journal of Geophysical Research: Space Physics*, *112*(A6), n/a-n/a.

Carbary, J. F. (2013), Wavy magnetodisk in Saturn's outer magnetosphere, *Geophysical Research Letters*, n/a-n/a.

Carbary, J. F., D. G. Mitchell, S. M. Krimigis, and N. Krupp (2007a), Electron periodicities in Saturn's outer magnetosphere, *J. Geophys. Res.*, *112*(A3), A03206.

Carbary, J. F., D. G. Mitchell, S. M. Krimigis, and N. Krupp (2009), Dual periodicities in energetic electrons at Saturn, *Geophys. Res. Lett.*, *36*(20), L20103.

Carbary, J. F., M. Kane, B. H. Mauk, and S. M. Krimigis (2014), Using the kappa function to investigate hot plasma in the magnetospheres of the giant planets, *Journal of Geophysical Research: Space Physics*, 2014JA020324.

Carbary, J. F., D. G. Mitchell, S. M. Krimigis, D. C. Hamilton, and N. Krupp (2007b), Charged particle periodicities in Saturn's outer magnetosphere, *J. Geophys. Res.*, *112*(A6), A06246.

Cassidy, T. A., and R. E. Johnson (2010), Collisional spreading of Enceladus' neutral cloud, *Icarus*, *209*(2), 696-703.

Chané, E., J. Saur, and S. Poedts (2013), Modeling Jupiter's magnetosphere: Influence of the internal sources, *Journal of Geophysical Research: Space Physics*, *118*(5), 2157-2172.

Chen, Y., T. W. Hill, A. M. Rymer, and R. J. Wilson (2010), Rate of radial transport of plasma in Saturn's inner magnetosphere, *J. Geophys. Res.*, *115*(A10), A10211.

Clarke, K. E., D. J. Andrews, A. J. Coates, S. W. H. Cowley, and A. Masters (2010a), Magnetospheric period oscillations of Saturn's bow shock, *J. Geophys. Res.*, *115*(A5), A05202.

Clarke, K. E., D. J. Andrews, C. S. Arridge, A. J. Coates, and S. W. H. Cowley (2010b), Magnetopause oscillations near the planetary period at Saturn: Occurrence, phase, and amplitude, *J. Geophys. Res.*, *115*(A8), A08209.

Cowley, S. W. H., and G. Provan (2015), Planetary period oscillations in Saturn's magnetosphere: comments on the relation between post-equinox periods determined from magnetic field and SKR emission data, *Ann. Geophys.*, *33*(7), 901-912.

Cowley, S. W. H., S. V. Badman, E. J. Bunce, J. T. Clarke, J. C. Gérard, D. Grodent, C. M. Jackman, S. E. Milan, and T. K. Yeoman (2005), Reconnection in a rotation-dominated magnetosphere and its relation to Saturn's auroral dynamics, *J. Geophys. Res.*, *110*(A2), A02201.

Dougherty, M. K. (2009), *Saturn from Cassini-Huygens*, Springer Netherlands, Dordrecht :.

Dougherty, M. K., et al. (2004), The Cassini Magnetic Field Investigation, in *The Cassini-Huygens Mission*, edited by C. Russell, pp. 331-383, Springer Netherlands.

Dungey, J. W. (1961), Interplanetary Magnetic Field and the Auroral Zones, *Physical Review Letters*, *6*(2), 47-48.

Espinosa, S. A., D. J. Southwood, and M. K. Dougherty (2003), How can Saturn impose its rotation period in a noncorotating magnetosphere?, *J. Geophys. Res.*, *108*(A2), 1086.

Eviatar, A., and J. D. Richardson (1986), Corotation of the Kronian Magnetosphere, *J. Geophys. Res.*, *91*(A3), 3299-3303.

Fleshman, B. L., P. A. Delamere, and F. Bagenal (2010), A sensitivity study of the Enceladus torus, *J. Geophys. Res.*, *115*(E4), E04007.

Gombosi, T. I., and A. P. Ingersoll (2010), Saturn: Atmosphere, Ionosphere, and Magnetosphere, *Science*, *327*(5972), 1476-1479.

Gurnett, D. A., A. Lecacheux, W. S. Kurth, A. M. Persoon, J. B. Groene, L. Lamy, P. Zarka, and J. F. Carbary (2009), Discovery of a north-south asymmetry in Saturn's radio rotation period, *Geophys. Res. Lett.*, *36*(16), L16102.

Gurnett, D. A., J. B. Groene, A. M. Persoon, J. D. Menietti, S. Y. Ye, W. S. Kurth, R. J. MacDowall, and A. Lecacheux (2010), The reversal of the rotational modulation rates of the north and south components of Saturn kilometric radiation near equinox, *Geophysical Research Letters*, *37*(24), L24101.

Hansen, C. J., L. Esposito, A. I. F. Stewart, J. Colwell, A. Hendrix, W. Pryor, D. Shemansky, and R. West (2006), Enceladus' Water Vapor Plume, *Science*, *311*(5766), 1422-1425.

Hansen, K. C., A. J. Ridley, G. B. Hospodarsky, N. Achilleos, M. K. Dougherty, T. I. Gombosi, and G. Tóth (2005), Global MHD simulations of Saturn's magnetosphere at the time of Cassini approach, *Geophys. Res. Lett.*, *32*(20), L20S06.

Hill, T. W. (1979), Inertial Limit on Corotation, *J. Geophys. Res.*, *84*(A11), 6554-6558.

Hill, T. W., A. M. Rymer, J. L. Burch, F. J. Crary, D. T. Young, M. F. Thomsen, D. Delapp, N. André, A. J. Coates, and G. R. Lewis (2005), Evidence for rotationally driven plasma transport in Saturn's magnetosphere, *Geophys. Res. Lett.*, *32*(14), L14S10.

Hill, T. W., et al. (2008), Plasmoids in Saturn's magnetotail, *J. Geophys. Res.*, *113*(A1), A01214.

Huebner, W. F., J. J. Keady, and S. P. Lyon (1992), Solar photo rates for planetary atmospheres and atmospheric pollutants, *Astrophys Space Sci*, *195*(1), 1-294.

Itikawa, Y., and N. Mason (2005), Cross Sections for Electron Collisions with Water Molecules, *Journal of Physical and Chemical Reference Data*, *34*(1), 1-22.

Jackman, C. M., et al. (2008), A multi-instrument view of tail reconnection at Saturn, *J. Geophys. Res.*, *113*(A11), A11213.

Jackman, C. M., et al. (2014), Saturn's dynamic magnetotail: A comprehensive magnetic field and plasma survey of plasmoids and traveling compression regions and their role in global magnetospheric dynamics, *Journal of Geophysical Research: Space Physics*, *119*(7), 2013JA019388.

Jia, X., and M. G. Kivelson (2012), Driving Saturn's magnetospheric periodicities from the upper atmosphere/ionosphere: Magnetotail response to dual sources, *Journal of Geophysical Research: Space Physics*, *117*(A11), n/a-n/a.

Jia, X., M. G. Kivelson, and T. I. Gombosi (2012a), Driving Saturn's magnetospheric periodicities from the upper atmosphere/ionosphere, *J. Geophys. Res.*, *117*(A4), A04215.

Jia, X., K. C. Hansen, T. I. Gombosi, M. G. Kivelson, G. Tóth, D. L. DeZeeuw, and A. J. Ridley (2012b), Magnetospheric configuration and dynamics of Saturn's magnetosphere: A global MHD simulation, *J. Geophys. Res.*, *117*(A5), A05225.

Johnson, P. V., J. W. McConkey, S. S. Tayal, and I. Kanik (2005), Collisions of electrons with atomic oxygen: current status, *Canadian Journal of Physics*, *83*(6), 589-616.

Johnson, R. E., H. T. Smith, O. J. Tucker, M. Liu, M. H. Burger, E. C. Sittler, and R. L. Tokar (2006), The Enceladus and OH Tori at Saturn, *The Astrophysical Journal Letters*, *644*(2), L137.

Jurac, S., and J. D. Richardson (2005), A self-consistent model of plasma and neutrals at Saturn: Neutral cloud morphology, *J. Geophys. Res.*, *110*(A9), A09220.

Jurac, S., M. A. McGrath, R. E. Johnson, J. D. Richardson, V. M. Vasyliunas, and A. Eviatar (2002), Saturn: Search for a missing water source, *Geophys. Res. Lett.*, *29*(24), 2172.

Kellett, S., C. S. Arridge, E. J. Bunce, A. J. Coates, S. W. H. Cowley, M. K. Dougherty, A. M. Persoon, N. Sergis, and R. J. Wilson (2011), Saturn's ring current: Local time dependence and temporal variability, *J. Geophys. Res.*, *116*(A5), A05220.

Kidder, A., R. M. Winglee, and E. M. Harnett (2009), Regulation of the centrifugal interchange cycle in Saturn's inner magnetosphere, *J. Geophys. Res.*, *114*(A2), A02205.

Kidder, A., C. S. Paty, R. M. Winglee, and E. M. Harnett (2012), External triggering of plasmoid development at Saturn, *J. Geophys. Res.*, *117*(A7), A07206.

Kivelson, M. G., and X. Jia (2014), Control of periodic variations in Saturn's magnetosphere by compressional waves, *Journal of Geophysical Research: Space Physics*, 2014JA020258.

Kriegel, H., S. Simon, U. Motschmann, J. Saur, F. M. Neubauer, A. M. Persoon, M. K. Dougherty, and D. A. Gurnett (2011), Influence of negatively charged plume grains on the structure of Enceladus' Alfvén wings: Hybrid simulations versus Cassini Magnetometer data, *J. Geophys. Res.*, *116*(A10), A10223.

Lamy, L. (2011), Variability of southern and northern periodicities of Saturn Kilometric Radiation, in *Planetary Radio Emissions VII: Proceedings of the 7th International Workshop on Planetary, Solar and Heliospheric Radio Emissions held at Graz, Austria, September 15-17, 2010*, edited by H. Rucker, W. Kurth, P. Louarn and G. Fischer, p. 578, Austrian Academy of Sciences Press.

Leisner, J. S., C. T. Russell, K. K. Khurana, M. K. Dougherty, and N. André (2005), Warm flux tubes in the E-ring plasma torus: Initial Cassini magnetometer observations, *Geophysical Research Letters*, *32*(14), L14S08.

Lishawa, C. R., R. A. Dressler, J. A. Gardner, R. H. Salter, and E. Murad (1990), Cross sections and product kinetic energy analysis of H[sub 2]O[sup +]--H[sub 2]O collisions at suprathermal energies, *The Journal of Chemical Physics*, *93*(5), 3196-3206.

Liu, X., T. W. Hill, R. A. Wolf, S. Sazykin, R. W. Spiro, and H. Wu (2010), Numerical simulation of plasma transport in Saturn's inner magnetosphere using the Rice Convection Model, *J. Geophys. Res.*, *115*(A12), A12254.

Lyons, L. R. (1984), *Quantitative aspects of magnetospheric physics*, D. Reidel Pub. Co. ;, Dordrecht ;.

Masters, A., M. F. Thomsen, S. V. Badman, C. S. Arridge, D. T. Young, A. J. Coates, and M. K. Dougherty (2011), Supercorotating return flow from reconnection in Saturn's magnetotail, *Geophys. Res. Lett.*, *38*(3), L03103.

Masters, A., J. P. Eastwood, M. Swisdak, M. F. Thomsen, C. T. Russell, N. Sergis, F. J. Crary, M. K. Dougherty, A. J. Coates, and S. M. Krimigis (2012), The importance of plasma β conditions for magnetic reconnection at Saturn's magnetopause, *Geophys. Res. Lett.*, *39*(8), L08103.

Mauk, B. H., et al. (2005), Energetic particle injections in Saturn's magnetosphere, *Geophys. Res. Lett.*, *32*(14), L14S05.

Moore, L., I. Mueller-Wodarg, M. Galand, A. Kliore, and M. Mendillo (2010), Latitudinal variations in Saturn's ionosphere: Cassini measurements and model comparisons, *J. Geophys. Res.*, *115*(A11), A11317.

Moriguchi, T., A. Nakamizo, T. Tanaka, T. Obara, and H. Shimazu (2008), Current systems in the Jovian magnetosphere, *Journal of Geophysical Research: Space Physics*, *113*(A5), n/a-n/a.

Morooka, M. W., J. E. Wahlund, A. I. Eriksson, W. M. Farrell, D. A. Gurnett, W. S. Kurth, A. M. Persoon, M. Shafiq, M. André, and M. K. G. Holmberg (2011), Dusty plasma in the vicinity of Enceladus, *Journal of Geophysical Research: Space Physics*, *116*(A12), n/a-n/a.

Nishida, A. (1982), *Magnetospheric Plasma Physics*, Center for Academic Publications Japan, Tokyo.

Paty, C. S. (2006), Ganymede's Magnetosphere: Unraveling the Ganymede-Jupiter Interaction through Combining Multi-fluid Simulations and Observations, 113 pp, University of Washington, Seattle.

Persoon, A. M., et al. (2009), A diffusive equilibrium model for the plasma density in Saturn's magnetosphere, *Journal of Geophysical Research: Space Physics*, *114*(A4), A04211.

Pierrard, V., and M. Lazar (2010), Kappa Distributions: Theory and Applications in Space Plasmas, *Sol Phys*, *267*(1), 153-174.

Pontius, D. H., and T. W. Hill (2006), Enceladus: A significant plasma source for Saturn's magnetosphere, *J. Geophys. Res.*, *111*(A9), A09214.

Pontius, D. H., and T. W. Hill (2009), Plasma mass loading from the extended neutral gas torus of Enceladus as inferred from the observed plasma corotation lag, *Geophys. Res. Lett.*, *36*(23), L23103.

Porco, C. C., et al. (2006), Cassini Observes the Active South Pole of Enceladus, *Science*, *311*(5766), 1393-1401.

Rubin, M., et al. (2015), Self-consistent multifluid MHD simulations of Europa's exospheric interaction with Jupiter's magnetosphere, *Journal of Geophysical Research: Space Physics*, *120*(5), 3503-3524.

Russell, C. T., C. M. Jackman, H. Y. Wei, C. Bertucci, and M. K. Dougherty (2008), Titan’s influence on Saturnian substorm occurrence, *Geophysical Research Letters*, *35*(12), n/a-n/a.

Rymer, A. M., B. H. Mauk, T. W. Hill, C. Paranicas, D. G. Mitchell, A. J. Coates, and D. T. Young (2008), Electron circulation in Saturn's magnetosphere, *J. Geophys. Res.*, *113*(A1), A01201.

Sánchez-Lavega, A., T. del Río-Gaztelurrutia, M. Delcroix, J. J. Legarreta, J. M. Gómez-Forrellad, R. Hueso, E. García-Melendo, S. Pérez-Hoyos, D. Barrado-Navascués, and J.

Lillo (2012), Ground-based observations of the long-term evolution and death of Saturn's 2010 Great White Spot, *Icarus*, *220*(2), 561-576.

Sanz-Requena, J. F., S. Pérez-Hoyos, A. Sánchez-Lavega, T. del Río-Gaztelurrutia, D. Barrado-Navascués, F. Colas, J. Lecacheux, and D. Parker (2012), Cloud structure of Saturn's 2010 storm from ground-based visual imaging, *Icarus*, *219*(1), 142-149.

Schippers, P., et al. (2008), Multi-instrument analysis of electron populations in Saturn's magnetosphere, *J. Geophys. Res.*, *113*(A7), A07208.

Sergis, N., C. S. Arridge, S. M. Krimigis, D. G. Mitchell, A. M. Rymer, D. C. Hamilton, N. Krupp, M. K. Dougherty, and A. J. Coates (2011), Dynamics and seasonal variations in Saturn's magnetospheric plasma sheet, as measured by Cassini, *J. Geophys. Res.*, *116*(A4), A04203.

Sergis, N., et al. (2010), Particle pressure, inertial force, and ring current density profiles in the magnetosphere of Saturn, based on Cassini measurements, *Geophys. Res. Lett.*, *37*(2), L02102.

Shemansky, D. E., P. Matheson, D. T. Hall, H. Y. Hu, and T. M. Tripp (1993), Detection of the hydroxyl radical in the Saturn magnetosphere, *Nature*, *363*(6427), 329-331.

Simon, S., J. Saur, H. Kriegel, F. M. Neubauer, U. Motschmann, and M. K. Dougherty (2011), Influence of negatively charged plume grains and hemisphere coupling currents on the structure of Enceladus' Alfvén wings: Analytical modeling of Cassini magnetometer observations, *J. Geophys. Res.*, *116*(A4), A04221.

Sittler Jr, E. C., et al. (2008), Ion and neutral sources and sinks within Saturn's inner magnetosphere: Cassini results, *Planetary and Space Science*, *56*(1), 3-18.

Smith, C. G. A. (2014), On the nature and location of the proposed twin vortex systems in Saturn's polar upper atmosphere, *Journal of Geophysical Research: Space Physics*, *119*(7), 5964-5977.

Smith, H. T., R. E. Johnson, M. E. Perry, D. G. Mitchell, R. L. McNutt, and D. T. Young (2010), Enceladus plume variability and the neutral gas densities in Saturn's magnetosphere, *J. Geophys. Res.*, *115*(A10), A10252.

Snowden, D., and R. Winglee (2013), Three-dimensional multi-fluid simulations of Titan's interaction with Saturn's magnetosphere: Comparisons with Cassini's T55 flyby, *Journal of Geophysical Research: Space Physics*, *118*(8), 4852-4863.

Spencer, J. R., J. C. Pearl, M. Segura, F. M. Flasar, A. Mamoutkine, P. Romani, B. J. Buratti, A. R. Hendrix, L. J. Spilker, and R. M. C. Lopes (2006), Cassini Encounters Enceladus: Background and the Discovery of a South Polar Hot Spot, *Science*, *311*(5766), 1401-1405.

Tarnovsky, V., H. Deutsch, and K. Becker (1998), Electron impact ionization of the hydroxyl radical, *The Journal of Chemical Physics*, *109*(3), 932-936.

Thomsen, M. F., D. B. Reisenfeld, D. M. Delapp, R. L. Tokar, D. T. Young, F. J. Crary, E. C. Sittler, M. A. McGraw, and J. D. Williams (2010), Survey of ion plasma parameters in Saturn's magnetosphere, *J. Geophys. Res.*, *115*(A10), A10220.

Tilley, M., E. Harnett, and R. Winglee (2015), Modeling the effects of plasma pressure anisotropy on Saturn's global magnetosphere, in *Magnetosphere's of Outer Planets 2015*, edited, Atlanta, GA.

Tokar, R. L., et al. (2006), The Interaction of the Atmosphere of Enceladus with Saturn's Plasma, *Science*, *311*(5766), 1409-1412.

Vasyliunas, V. M. (1983), Plasma distribution and flow, in *Physics of the Jovian Magnetosphere*, edited by A. J. Dessler, pp. 395-453, Cambridge University Press.

Waite, J. H., et al. (2006), Cassini Ion and Neutral Mass Spectrometer: Enceladus Plume Composition and Structure, *Science*, *311*(5766), 1419-1422.

Ward, D. (2014), *FIRE: How Fast, Inexpensive, Restrained, and Elegant Methods Ignite Innovation*, 240 pp., Harper Business.

Wilson, R. J., R. L. Tokar, and M. G. Henderson (2009), Thermal ion flow in Saturn's inner magnetosphere measured by the Cassini plasma spectrometer: A signature of the Enceladus torus?, *Geophys. Res. Lett.*, *36*(23), L23104.

Wilson, R. J., R. L. Tokar, M. G. Henderson, T. W. Hill, M. F. Thomsen, and D. H. Pontius, Jr. (2008), Cassini plasma spectrometer thermal ion measurements in Saturn's inner magnetosphere, *J. Geophys. Res.*, *113*(A12), A12218.

Winglee, R. M. (1998), Multi-fluid simulations of the magnetosphere: The identification of the geopause and its variation with IMF, *Geophysical Research Letters*, *25*(24), 4441-4444.

Winglee, R. M., D. Snowden, and A. Kidder (2009), Modification of Titan's ion tail and the Kronian magnetosphere: Coupled magnetospheric simulations, *J. Geophys. Res.*, *114*(A5), A05215.

Winglee, R. M., A. Kidder, E. Harnett, N. Ifland, C. S. Paty, and D. Snowden (2013), Generation of periodic signatures at Saturn through Titan's interaction with the centrifugal interchange instability, *Journal of Geophysical Research: Space Physics*, n/a-n/a.

Young, D. T., et al. (2004), Cassini Plasma Spectrometer Investigation, in *The Cassini-Huygens Mission*, edited by C. Russell, pp. 1-112, Springer Netherlands.

Zarka, P. (1998), Auroral radio emissions at the outer planets: Observations and theories, *Journal of Geophysical Research: Planets*, *103*(E9), 20159-20194.

Zieger, B., K. C. Hansen, T. I. Gombosi, and D. L. De Zeeuw (2010), Periodic plasma escape from the mass-loaded Kronian magnetosphere, *Journal of Geophysical Research: Space Physics*, *115*(A8), n/a-n/a.

Zong, Q. G., et al. (2004), Cluster observations of earthward flowing plasmoid in the tail, *Geophys. Res. Lett.*, *31*(18), L18803.

VITA

ASHOK RAJENDAR

Ashok Rajendar was born in Mumbai, India in 1984, and moved with his family to Hong Kong in early 1985. He graduated from South Island School in 2002. Ashok earned a B.S. in Mechanical Engineering at Cornell University in May 2006, after which he spent a year working at Lutron Electronics, Inc. in Coopersburg, Pennsylvania. His first brush with the private sector sent him scurrying back to the warm bosom of academia, whereupon he enrolled in the Georgia Institute of Technology's School of Mechanical Engineering. He earned his M.S. in Mechanical Engineering in December 2011 (Thesis: " Internal flow effects on performance of combustion powered actuators"), having already begun doctoral research into Saturn's magnetosphere with Professor Carol Paty in the School of Earth and Atmospheric Sciences in January 2011. When he is not working, he enjoys spending time with his family, riding his bicycle, and reading.